Structures of columnar packings with soft and hard spheres

Jens Winkelmann

School of Physics

Trinity College Dublin

A thesis submitted for the degree of

Doctor of Philosophy

March 8, 2020

Declaration

I declare that this thesis has not been submitted as an exercise for a degree at this or any other university and it is entirely my own work. I agree to deposit this thesis in the University's open access institutional repository or allow the Library to do so on my behalf, subject to Irish Copyright Legislation and Trinity College Library conditions of use and acknowledgement.

Jens Winkelmann .....

Summary

Columnar structures refer to dense cylindrical packings of spheres. They are ubiquitous throughout botany, foams, and have recently also become popular in nanoscience. We investigate such structures by carrying out computer simulations, analytic calculations, as well as simple experiments.

Our simulations concern packings of *soft* spheres of diameter d inside a cylinder of diameter D. We present a phase diagram of all stable structures, including so-called *line-slip* arrangements, up to the diameter ratio $D/d = 2.71486$, where the nature of the densest sphere packing changes. We also report on an experimental observation of such a line slip in a monodisperse foam confined in a cylinder.

Since macroscopic systems of this kind are not confined to the stable states of the phase diagram, we consequently explored structural transitions by carrying out further simulations. Such transitions are in general hysteretic. We summarise details of a reversible transition in form of a stability diagram. All permissible structural transitions of stable packings from the phase diagram are then presented in a directed network.

Lee *et al.* [T. Lee, K. Gizynski, and B. Grzybowski, Adv. Mater. **29**, 1704274 (2017)] recently developed a novel method to assemble columnar structures inside a rotating cylinder. In this method the spheres, which are of lower density than the surrounding fluids, are driven by a centripetal force toward the central axis. Depending on the number of spheres, a variety of structures were observed.

We analysed this experimental method using analytic energy calculations for structures of soft spheres. From these calculations, we obtained a phase diagram displaying interesting features including *peritectoid* points. These results are corroborated by numerical simulations for finite-sample size with soft spheres. However, they also extend our previous results with the appearance of a line-slip structure due to finite-size effects.

The simplest columnar structure that can be assembled by Lee *et al.*'s experimental method consists of a linear chain of spheres. Such a chain, confined by a cylindrical harmonic potential, exhibits a variety of buckled arrangements as it is compressed longitudinally by hard walls at each ends. We developed a theoretical model, based on an iterative stepwise method, as well as an analytic linear approximation to analyse this behaviour. A wide range of predicted structures occurring via bifurcations are explored and presented in an energy bifurcation diagram. The stable structures are also observed in experiments using rapid rotations and simulations based on energy minimisation.

Finally, we conclude all our results and present several directions this work may be extended in the future. This includes the development of a new simulation model of such structures for soft matter such as soap bubbles or emulsion droplets. We present the limits of the soft sphere model used in this thesis by comparing simulation results with those of an exact foam simulation.

Acknowledgements

It has been almost four years now that I came to this beautiful island of Ireland. Despite some stress throughout the years, the PhD at Trinity College Dublin has been a wonderful experience for me. I had the great opportunity to take part at over 10 conference during the last four years. It allowed me to travel to amazing places such as Italy, Cambridge, and Yale where I had the opportunity to meet some old friends, but also to make some new ones.

So I'd like to thank the Irish Research Council (and the irish taxpayer) for funding my research (and all my conference trips!).[1]

I liked to say thank you to my supervisor Stefan Hutzler for all his support during the PhD, but also for all the work during the application of the IRC Scholarship that made the PhD possible in the first place. I would like to thank Denis Weaire for all his great ideas which shaped this PhD tremendously and Matthias Möbius for helpful discussion in our weekly group meetings. Special thanks also goes to Adil Mughal from Aberystwyth University, Wales, for lots of fruitful discussions and collaborative support in studying columnar structures. He also proof-read (and tore apart) the first draft of the introduction.

Big thanks also to my former office mates, Ben and Fritz! It was always great craic with you guys in and outside the office. Don't you agree, Ben? 🍺

[1] Although it should be mentioned that PhD students in Dublin are in dire need for an increase of the annual stipends due to an enormous increase in living costs, especially rents! I hope any future PhD student who reads this, will not have to deal with these problems anymore.

In this regards, I also want to thank you two for proof-reading chapter 3 and 4 for me and Steven Burke and John Ryan-Purcell for proof-reading chapters 5 and 6, respectively.

Of course, I thank my parents and sister for all the support throughout all the years of studies, especially for letting me leave to Ireland.

A *huge* thank you also goes to Bernadette McAweeney for the great hospitality during the four years of my PhD, even though I only intended to stay for a few week, initially. I got treated like her fourth son at her house (not always to my fortune).

Furthermore, I need to thank some old friends back home from the Ruhrgebiet (Germany). `Tobey0r` (Tobias Jung) has been very helpful with questions regards design and graphics and proof-listening to many presentations before conferences. He is also the reason why this thesis has not been written in Comic Sans. I'd like to thank Tracy as well for her many visits and travelling with me all around Ireland. It helped me to stay sane in some stressful times.

Thanks also to my personal enemy no. 2, Marie Schmitz, for being mean and always failing to kill me. I hope you will suffer the same cruel fate as personal enemy no. 1!!!

I also ought to mention the helpful support by Maik Malki and Christian-Roman Gerhorst. Maik Malki gave me some good advice in regards the thesis style and it was helpful to have friends far away, that are in similar situation, to talk to. Last but not least I also acknowledge Ismo Toijala's amazing job: He proof-read my complete thesis a few days before submission within six hours and found 312 (minor) mistakes in the (almost) final version of my thesis.

Chronological list of publications

1. J. Winkelmann et al., *2d foams above the jamming transition: deformation matters*, Colloids Surf. A **534**, 52–57 (2017)

2. J. Winkelmann et al., *Corrected Article: Simulation and observation of line-slip structures in columnar structures of soft spheres [Phys. Rev. E 96, 012610 (2017)]*, Phys. Rev. E **97**, 059902 (2017)

3. A. Mughal et al., *Columnar structures of soft spheres: metastability and hysteresis*, Phys. Rev. E **98**, 043303 (2018)

4. J. Winkelmann et al., *Theory of rotational columnar structures of soft spheres*, Phys. Rev. E **99**, 020602(R) (2019)

5. F. F. Dunne et al., *Implementation of morse–witten theory for a polydisperse wet 2d foam simulation*, Phil. Mag. **99**, 2303–2320 (2019)

6. J. Winkelmann et al., *Equilibrium configurations of hard spheres in a cylindrical harmonic potential*, EPL, accepted for publication. (2019)

Contents

List of Figures

List of Tables

Chapter 1

An introduction to columnar structures

1.1 A Friday-afternoon experiment: Packing golf balls in a tube

It was a typical cold and rainy Friday afternoon in our office at Trinity College Dublin. Because we had no money to go for a pint and nothing better to do, we decided to try out the following experiment using nothing more than golf balls and an acrylic tube: We sequentially dropped roughly 40 golf balls into the transparent tube, whose diameter was a bit more than twice the size of the golf balls. To our surprise they stacked up there to a perfectly ordered cylindrical structure, filling up the tube without any defects [1] .

This simple experiment of packing golf balls into a tube is one illustrative method of creating structures that we call *columnar structures* due to their cylindrical form. The self-assembled structure from this Friday-afternoon experiment is displayed in Fig 1.1(a). Because of the flat office floor and

[1]Link to the video: `https://www.reddit.com/r/ScienceGIFs/comments/b2c604/ordered_columnar_structures_golf_balls_packed/`

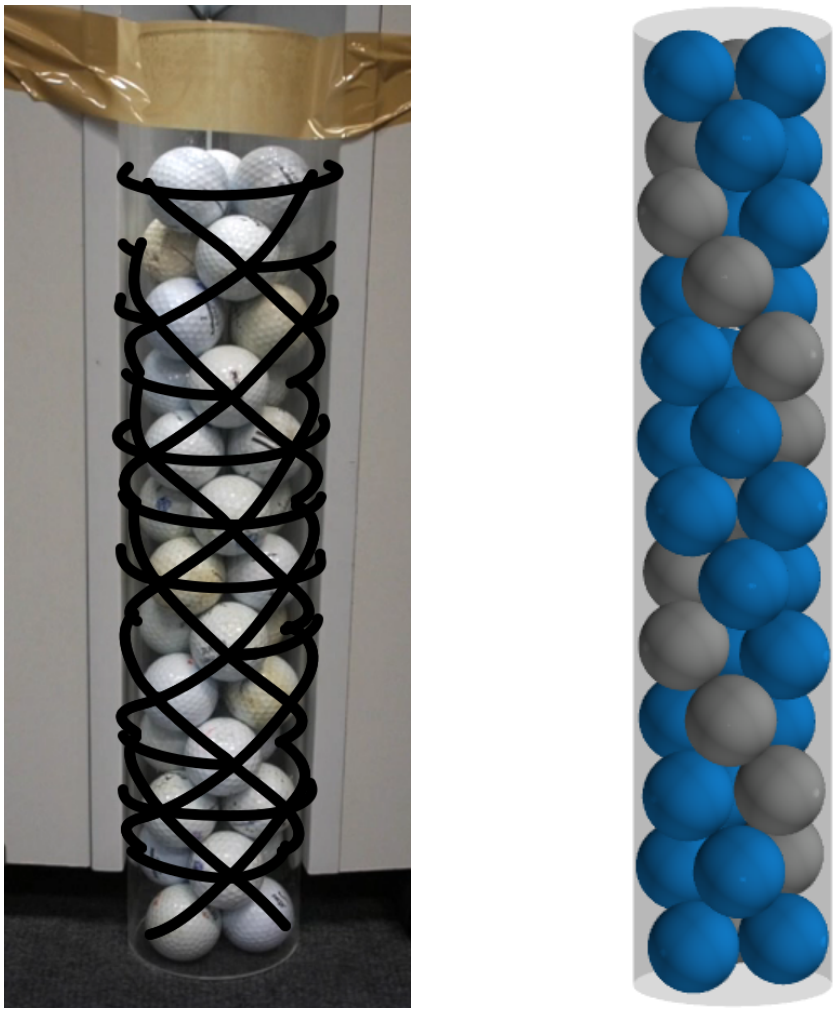

(a) **(b)**

Fig 1.1: An illustrative experimental realisation of a columnar structure with golf balls (a), compared to the corresponding simulated structure (b). Such a structure assembles when golf balls are dropped sequentially inside a tube with a diameter ratio of $D/d \approx 2.22$ between diameter of the golf balls d and tube diameter D. The black lines indicate the contacts between neighbouring golf balls. A short video of the full assembly process can found on `reddit` [7]. By using the same diameter ratio as in the experiment, this structure can also be found with the simulation methods developed in this thesis (see (b)).

the particular ratio of tube to golf ball diameter the first three balls assemble in an equilateral triangles at the bottom. When sequentially being dropped, the next three balls then end up in the valleys created at the contact points

of the bottom balls. Each layer of the following spheres is then rotated by an angle of $\pi/3$ compared to the balls in the preceding layer. This particular packing thus resembles close similarities to the hexagonal close-packed lattice.

With the black lines covering the packing we highlight the contacts between neighbouring spheres, giving us information about the contact network. It actually reveals to us that some spheres in the packing of Fig 1.1(a) are missing contacts with their neighbours. This exceptional type of structure will be a particular focus of this thesis and therefore discussed and explained in a later chapter (see chapter 2.3.2).

The same structure from this simple experiment, can also be calculated from computer simulations (see Fig1.1(b)). Details on such simulation methods are a subject of this thesis. We will discuss and use a range of numerical methods that are employed to simulate such structures.

The packing of golf balls depends on many external factors, such as friction, boundary conditions, assembly process, or history of the structure. If neglecting such such external factors for reasons of simplicity, the packing problem can be reduced to a geometrical problem. The only major control parameter for such a simplified system is then the diameter ratio D/d of the tube diameter D to sphere (or golf ball) diameters d. The rules of golf dictate the golf ball diameter to be approximately $d \approx 4.27\,\mathrm{cm}$ and the tube diameter is measured as $D = 9.50\,\mathrm{cm}$. Thus, we can estimate the diameter ratio for our experiment to be roughly $D/d \approx 2.22$. The corresponding simulated structure from Fig 1.1(b) was found at the same diameter ratio.

Packing spheres (or golf balls) into a cylinder differs from other packing problems in terms of it symmetry. The simple interaction type of spheres makes this problem easy to simulate and investigate theoretically. Changing the packed objects for instance to ellipsoids would increase the complexity of this problem beyond the scope of this thesis. The cylindrical confinement gives this particular packing problem also a rotational symmetry. This is

for instance not the case for packing spheres into an elliptical confinement. It leads to structures that can have an N-fold symmetry, such as the one presented in Fig 1.1 which has a 3-fold symmetry.

1.2 What are columnar structures?

We call any cylindrical structure that constitutes of densely packed objects of spherical-like shape, a columnar structure. This broad definition includes random packings of spheres inside a large cylindrical container, as well as ordered structures that are periodic in vertical direction, similar to the structure in Fig 1.1. In order to obtain an *ordered* columnar structure, it is a vital feature that the spherical objects are of equal size. In the following, we will refer to packings of objects of equal size as *monodisperse* packings (i.e. the words equal size and monodisperse can be used interchangeably).

In this thesis we only discuss columnar structures that are *ordered* (in the sense of periodicity in one direction) and *without internal spheres*. All spheres are therefore in touch with the cylinder wall. In this range of diameter ratios, a random packing is not possible with monodisperse spheres since the sphere packing can be mapped to a disk packing on the surface of the cylinder wall (see chapter 2.4). Packings of monodisperse disks, however, do not form random packings. Columnar structures with point defects are possible, but not subject of this thesis.

Strictly speaking the definition of order excludes any type of mixed structures. For some of our investigations in later chapters, mixtures of two of such ordered structures play an important role as well.

Packing equal-sized spheres densely inside cylinders (like our Friday-afternoon experiment in Fig 1.1) is one of the simplest procedures to build them. There are many more procedures to assemble such arrangements. Further assembly methods include packing of spheres on the surface of a cylinder or

a novel method involving rapid rotations [8]. A more remote but stimulating occurrence are so-called "tubular crystals"; these consist of various columnar structures interwoven in three dimensions [9].

A. Rogava even managed to build such a structure without any confinement. He built a tower of tennis balls (see lower left of Fig 1.2) whose structure resembled very close that of our golf balls [10]. In these experiments friction between the tennis balls is vital. Without the friction there would be no torque balance and the balls would roll away.

Fig 1.2: Building a columnar structure by a stacking tennis balls to a tower [10]. By removing tennis balls from the outside layer in the pyramid on the upper right, various types of tennis ball towers can be created. The one on the lower left resembles a columnar structure very close to that in Fig 1.1. All structures are only held together by friction. The image was taken from Ref [10].

He started his experiments with tennis balls stacked to a pyramid (see upper right image of Fig 1.2). By carefully removing some of the outside balls, he first ended up with a symmetric structure of 16 balls with three

hexagonal and three triangular sides (image top left of Fig 1.2). In a second try, he was also able to build a bizarre, Christmas-tree-like structure made of 14 balls (image middle right of Fig 1.2). By removing the bottom outer balls, he ended up with a small tower of seven tennis balls that already is a small columnar structure (image lower right of Fig 1.2). By adding more tennis balls to the tower, a very similar structure emerged to that of our golf ball packing in Fig 1.1. The top ball here is crucial for keeping the structure steady: it presses down on the three balls in the layer below.

Throughout this thesis we focus on two different assembly methods for columnar structures, mainly with theories and simulations. One of them is the assembly procedure of identical spheres packed inside an infinitely long cylinder. The other (more novel) method involves rapid rotations of spheres inside a liquid-filled tube. This process was first used by Lee *et al.* [8] to experimentally create such structures. From our theories and simulations, we predict which ordered structures are to be expected under what conditions.

1.3 The phyllotactic notation: Categorising columnar structures

One way of classifying ordered columnar structures uses the *phyllotactic* notation, adopted from botany. As the ancient Greek origin of the name "phyllotaxis" suggests (*phyllon* = leaf, *táxis* = arrangement), it describes the arrangement of leaves of a plant. The term was first coined by Charles Bonnet in the 18th century [11]. In his book "On Growth and Form" (1917), the mathematical biologist D'Arcy Thompson analysed such arrangements of plant parts around an axis [12]. This included cylindrical structures like leaves around a stem, pine cones, or pineapples, but also the planar patterns of florets in a sunflower head. While the arrangement in the former are cylindrical, the

spirals in the latter are arranged on a disk.

Phyllotaxis in the context of disk arrangement was recently investigated by Sadoc *et al.* [13]. They looked at dense organisation of small disks inside a large circular domain. By using an algorithm that sets out of the disks on a Fermat spiral, they investigated the very nature of this assembly. Our focus, however, will be on phyllotaxis in the context of cylindrical structures.

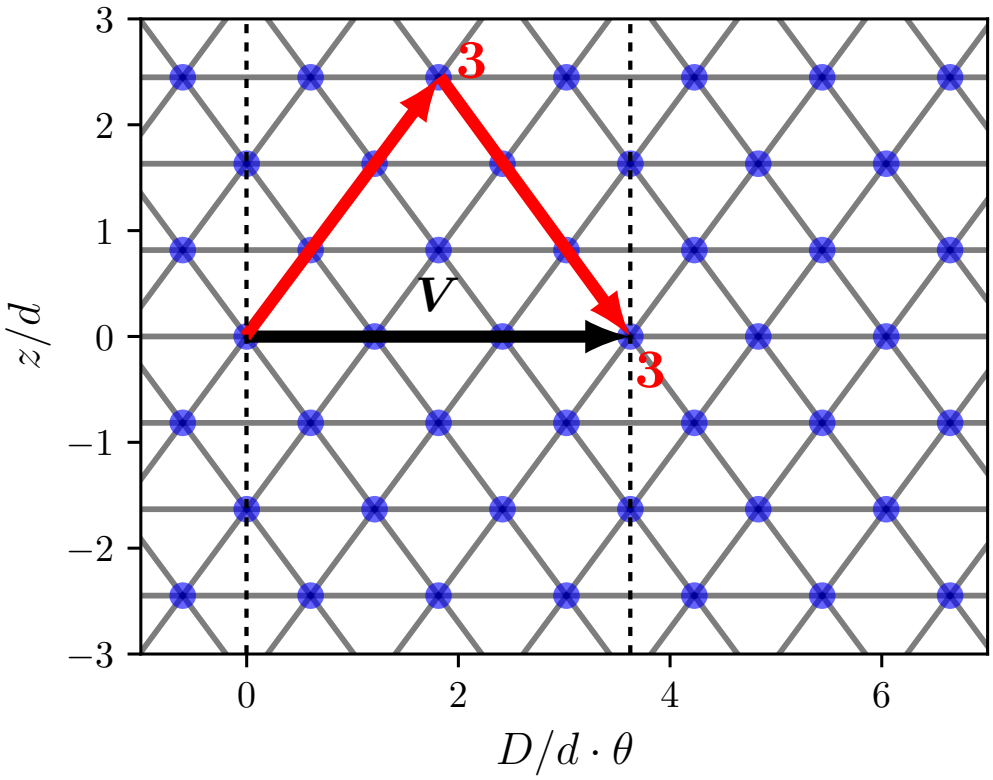

Fig 1.3: The rolled-out contact network of an example columnar structure for explaining the phyllotactic notation. Each blue dot represents a sphere rolled-out into a plane of height z and azimuthal angle θ. The grey lines show the contacts between neighbouring spheres. The length of the periodicity vector $\boldsymbol{V}$ (in black) is equal to the circumference of the cylinder. It takes three spheres to go along this vector from the centre sphere to its first periodic image and none along any of the red arrows; hence one duplet to characterise this structure is $(3, 0)$. The second duplet $(3, 3)$ is found by counting the number of spheres along the two red arrow. Combining these to the phyllotactic notation, the structure is identified as a $(3, 3, 0)$.

In columnar structures, such a phyllotactic pattern can be found in the rolled-out contact network. Each sphere position is displayed as a dot and the contacts between neighbouring spheres are represented by lines. The phyllotactic pattern is achieved by rolling out the positions and contacts into a plane. For the type of columnar structures that we focussed on during this thesis, it forms a triangular lattice, such as the one in Fig 1.3.

Other types of lattices are also possible. For example, the rolled-out pattern for a linear chain of spheres (the simplest columnar structure) consists of vertical lines. Square lattices can be observed for zigzag structures as well as columnar structure with internal spheres [14] that are outside of the scope of this thesis.

Since the phyllotactic patterns are two-dimensional, only two numbers are necessary to describe them. However, a duplet notation would be ambiguous since these numbers might differ depending on the chosen coordinate system. Thus, these structures are best described by a triplet of positive integers $(l = m+n, m, n)$ with $l \geq m \geq n$. Each number l, m, and n describes a family of lines within the 2D rolled-out pattern (or spiral in the 3D packing). They count the number of spirals in each direction until the spiral repeats (at the dashed lines). This notation, however, only applies to triangular lattices and is therefore restricted to the structures without internal spheres (as covered in this thesis).

For instance, Fig 1.3 shows this type of pattern for the $(3, 3, 0)$ structure. This structure is similar to that in Fig 1.1; their differences are marginal. This structure consists of layers of spheres stacked on top of each other with three sphere in each layer. Each sphere is here in contact with all of it six neighbouring spheres.

The phyllotactic pattern is characterised by the periodicity vector $\boldsymbol{V}$. It starts at the blue dot in the origin and wraps around the cylinder where it points to the first periodic image of the dot in the origin. For the example

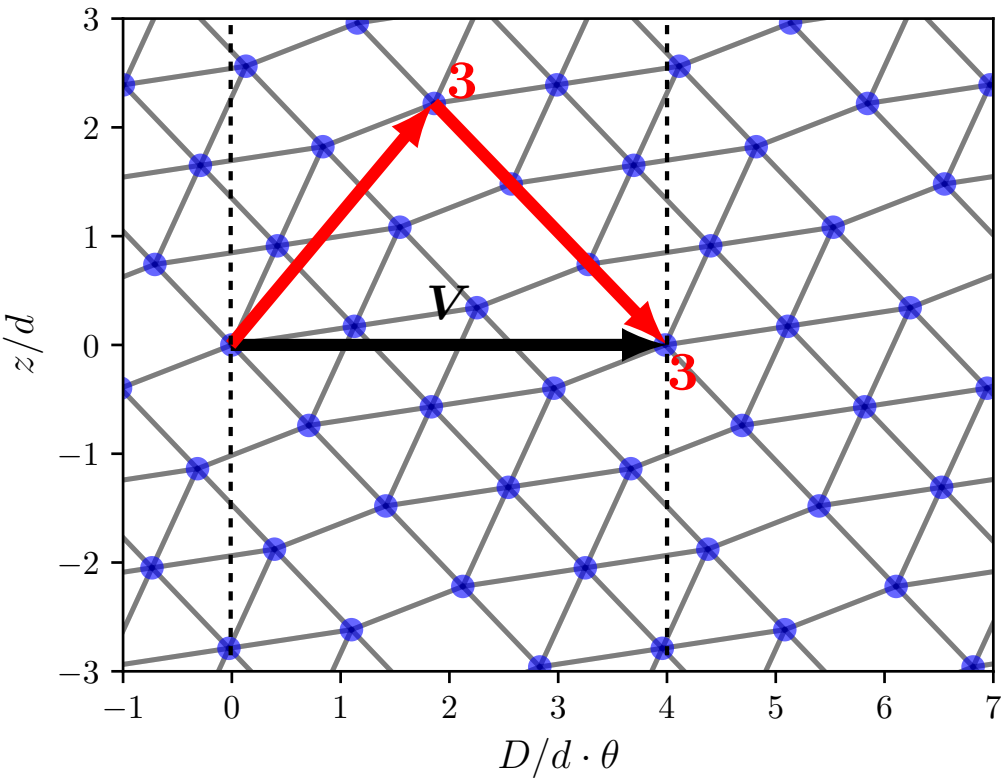

Fig 1.4: The rolled-out contact network of the columnar structure in Fig 1.1. Each blue dot represents a sphere rolled-out into a plane of height z and azimuthal angle θ and the black lines are contacts between neighbouring spheres. This contact network differs from that in Fig 1.4 solely by the missing contacts that are also visible in Fig 1.1. This structure is classified as a $(3, \mathbf{3}, 0)$ line-slip structure in phyllotactic notation. Details of this structure are discussed in 2.3.2.

in Fig 1.3, this vector can be decomposed into two red basis vectors of the triangular lattice.

One duplet of integers to categorise this structure can then be obtained by counting the number of blue dots (or black lines) along these two vectors, which form a coordinate system in this pattern. The corresponding duplet is then $(3, 3)$. A further coordinate system is given by the periodicity vector $\boldsymbol{V}$ and one of the red vectors. Since in our example the periodicity vector $\boldsymbol{V}$ coincides with a basis vector of the triangular lattice, the duplet within

this coordinate system is $(3, 0)$. To avoid ambiguity, these two duplets can be combined to a triplet. Therefore, in the phyllotactic notation a structure that has this type of triangular lattice is described by the integer triplet $(3, 3, 0)$.

The rolled-out contact network of the golf ball packing from Fig 1.1 is shown in Fig 1.4. Here we can spot the missing contacts between neighbouring spheres again that we already saw in the highlighted contact network of Fig 1.1. Fig 1.4 exposes that those gaps appear along a line; hence we will call this type of structure line slips (see chapter 2.3.2 for details). Since this line of missing contacts crosses one of the red arrows, we will mark one of the "3"s in the integer triplet with a bold number. The phyllotactic notation of the example structure in Fig 1.1 (and 1.4) is written as $(3, \mathbf{3}, 0)$.

1.4 From botany and foams to nanoscience: Applications of columnar structures

Ordered columnar structures appear in various research fields on a broad range of length scales from metres down to the nanoscale. Fig 1.5 illustrates examples from four different research topics ordered by their length scale. On the largest scale, such structures can be found in botany where seeds of a plant assemble around the stem. Plants like the *titan arum* can be up to a metre in size [17].

On a slightly smaller scale bubbles of equal size crystallise to columnar foam structures when confined in a glass tube. The bubble and tube diameters for such foam structures are usually of centimetre scale.

In nanoscience such structures can be found in man-made objects which are on length scales from a micron to the nanoscale. Novel materials, such as rods or fibres, are assembled with these structures, where the spheres are on the nanoscale, but the length of the objects is on the microscale [16, 18].

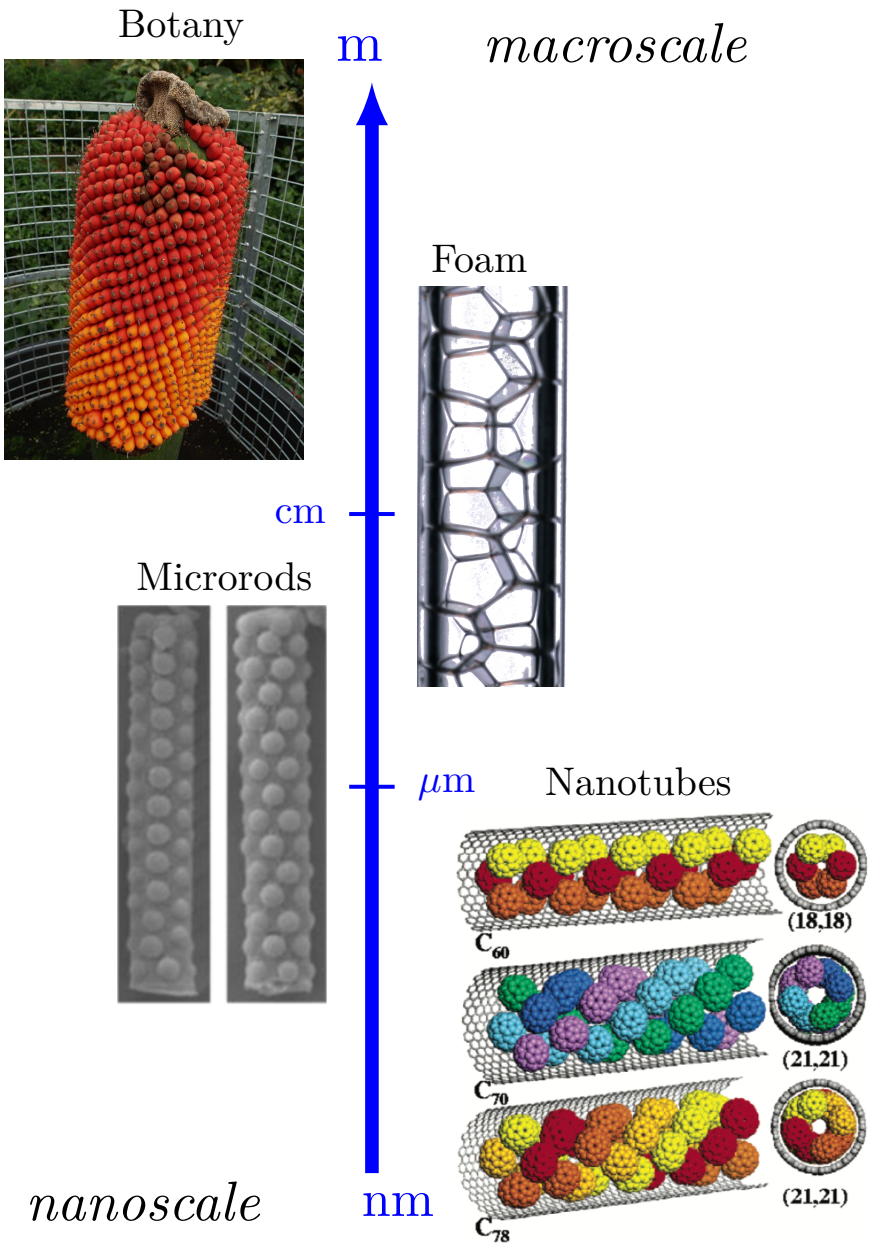

Fig 1.5: Examples of columnar structures from length scales ranging from nanometres (nm) to the metre scale (m). The example on the nanoscale shows particles trapped inside nanotube (taken from [15]). They can also be used to build rods/fibres where the rods/fibres are on the size of a micron (taken from [16]). The research on the macroscale investigates columnar structure in foams and botany. The plant shown here is the *titan arum* (also called corpse flower) (taken from [17]). All examples are discussed in great detail in the text.

Furthermore, these structures also form when molecules such as fullerenes (C60, C70, or C78) are trapped inside a nanotube [15]. Here they are also used to alter chemical and physical properties of such nanotubes.

In this section we will discuss all of these research fields from different length scales in closer detail. We will first give two examples from botany and discuss a selected range of literature on this topic. In the second subsection, we then cover the recent foam research on these structures, up to open questions of current investigations.

At the end of this section, a few interesting applications from nanoscience are introduced. We depict two applications of these applications in closer detail: Wu *et al.* from Penn State University built microrods of Si nanoparticles, which display similar structures as found in our simulations [16]. At Harvard, Tanjeem *et al.* are trying to create a so-called optical metamaterial with a negative refractive index from these packings [19]. They self-assemble such structures by packing nanocolloids on the surface of a cylinder.

1.4.1 Examples from botany

Because of their appearance in plants, columnar structures were first studied in botany [12, 20]. But they are also of interest in other biological areas, including bacteria, viruses, and microtubules [21–24]. Quite recently, such structures were discovered in the notochord of the zebra fish as well [25].

An extensive literature about regular arrangement of lateral organs in plants and flowers has been generated over the last century by biologists and mathematician alike. Their main interest lies in modelling suitable synthesis of realistic images of flowers and fruits that exhibit such spiral phyllotactic patterns. Reviews on this are given by Erickson in Ref [26] and by Lindenmeyer *et al.* in Ref [27]. Most of the mathematical models relate arrangements from botany to packing problems. Lindenmeyer *et al.* [27] describe one model that reduces phyllotaxis to the problem of packing circles on the surface of a

cylinder. In this model, the arrangement of the lateral organs in a plant is described purely by geometry, similar to the models that we use throughout this thesis.

One of the largest flowers where the berries arrange in a regular cylindrical form is the *titan arum*, also called corpse flower due to its rotten smell. An image of it is displayed at the top of Fig 1.5. This flower can be up to 3 m in height and is natively solely found in western Sumatra and western Java.

Less exotic plants with such structures can also be found in Ireland. Two examples from Dublin are presented in Fig 1.6. Fig 1.6(a) displays a plant called "*arum maculatum*" with common names such as "jack in the pulpit" or "cuckoo-pint". Its berries are similar to that of the corpse flower, which is its larger relative. However, the cuckoo-pint is much smaller in height (height ~ 20 cm) and can be found all around Europe.

The berries that form the regular arrangement around the stem of the plant start to occur in autumn. The berry arrangement varies with the stem to berry size, but ordered structures might only occur when all berries have a similar diameter. Otherwise the berries form a structure with defects or simply random clusters around the tip of the stem. [2]

Another plant that can be found in many gardens of residential areas in Ireland is the Australian bottlebrush (see Fig 1.6(b)). It assembles its seed capsules around a branch of the plant. With varying ratio of seed capsule size to branch size, different structures can be observed.

It originates from Australia, where it is mostly found in more temperate regions. But since it favours moist conditions, it thrives as well when planted in gardens in Ireland. When blooming in the summer time the seed capsules turn into brush-like flowers resembling a traditional bottle brush. This

[2] While the berries of the cuckoo-pint start out green, they turn into a bright attractive red with time. However, such berries are extremely poisonous, resulting in swelling of the throat to upsetting the stomach.

(a)

(b)

Fig 1.6: Two examples of columnar structures from botany. The two images show plants found in Dublin, where the berries/seeds assemble around the stem in a columnar fashion. (a) displays the *arum maculatum* spotted in Bushy Park, Rathfarnham, Dublin. In (b) the Australian bottlebrush, which was found in Templeogue, Dublin, is shown.

appearance is what gives the plant its common name.

1.4.2 Dry and wet foam structures

Another occurrence of ordered columnar arrangement on the macroscale are foam structures confined inside a glass tube. They can be realised experimentally with equal-sized soap bubbles inside a glass tube [28–31]. These foam structure play a major role in this thesis, since we performed such experiments in chapter 3.2 in order to compare simulations with experiments. Thus, we discuss the experimental set-up, as well as major results from recent years, in the following paragraphs.

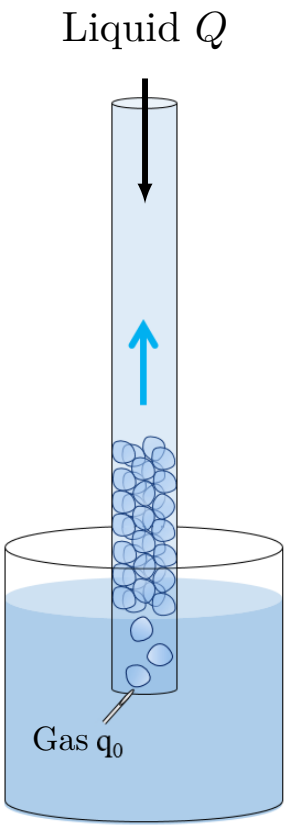

Fig 1.7: Experimental set-up to produce columnar foam structures. Gas is introduced at a constant flow rate q_0 into a surfactant solution to create bubbles of equal size. By a bubbling needle, the bubbles of equal size are filled sequentially into a glass tube from the bottom. There they crystallise to a columnar foam structure. Their liquid fraction is increased by feeding the foam column with a surfactant solution with a liquid flow rate Q from top (forced drainage).

In the experiments, the foam structures are created by filling the tube sequentially with bubbles from the bottom (see Fig 1.7 for an illustration of the experimental set-up). A steady stream of bubbles is produced by blowing air through a needle dipped in a surfactant solution. Bubbles of equal size are created by using a constant gas flow rate q_0. They are then collected in a cylindrical tube, where they crystallise to a columnar foam. The resulting foam column is put under forced drainage by feeding it with surfactant solution from the top with a liquid flow rate Q. With this method, the amount of liquid

(or the liquid fraction) in the foam can be adjusted [32, 33].

Depending on the liquid fraction in the foam, the columnar foam crystal can either be a *dry* or *wet* structure. Dry foam structures have a low liquid fraction and the cell shape consists of polyhedrons (see foam structure in Fig 1.5 or Fig 1.8(a) and (b)). In wet foams the bubble shape is spherical due to a high liquid fraction (see Fig 1.8(c)).

These foam crystals from the dry to the wet limit have been extensively studied over the last 20 years [28–32, 34]. Experimentally discovered foam structures from Refs [30, 31] have a very close structural resemblance with the sphere packings presented in this thesis. Many of these structures have been discovered, classified with the phyllotactic notation, and tabulated throughout the years.

Previous work on columnar foams has not only focussed on experiments, but also computer simulation. Most simulations in the past have been carried out using the Surface Evolver [35] software and have focused mainly on dry structures [29, 30, 36]. Surface Evolver is a computer program for modelling surfaces shaped by surface tension, other energies, and external constraints. It is based on surface energy minimisation, i.e. it evolves a given surface structure towards minimal energy by various types of numerical minimisation routines. Fig 1.8(a) shows the zigzag structure, simulated with Surface Evolver, and (b) displays a photograph from the experiments [30].

This simple zigzag structure was the subject of intensive experimental investigations itself. The observation of a moving interface with increasing liquid fraction was reported by Hutzler *et al.* in 1997 [32]. This included an unexpected 180° twist interface, whose explanation is still lacking.

Further discovered structures include complex structures with internal spheres (or foam cells) [29, 31]. Some dry foam structures with interior cells were found to consist of a chain of pentagonal dodecahedra or Kelvin cells in the centre of the tube [29]. Many more arrangements of this type were also

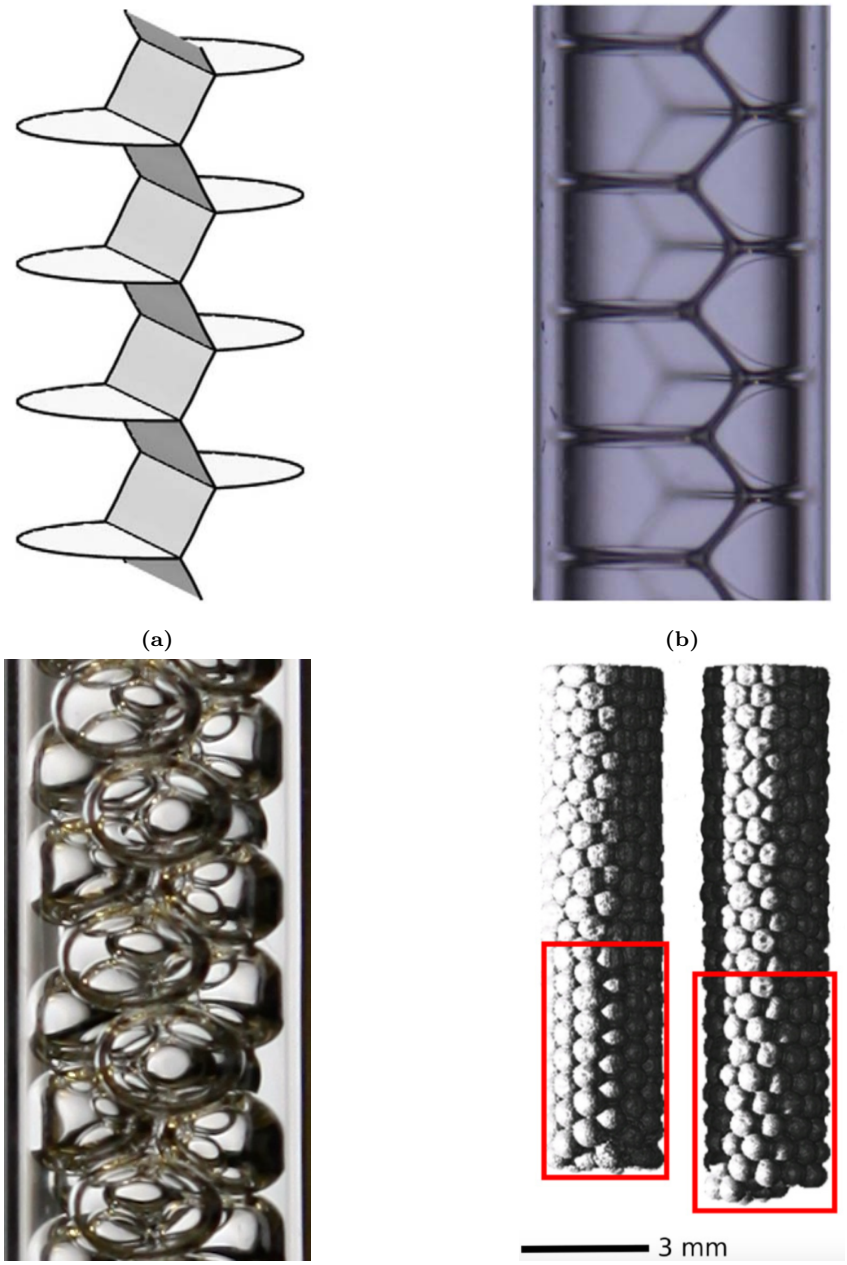

Fig 1.8: Columnar structures of soap bubbles confined inside a glass tube. (a) and (b) show a zigzag structure of a dry foam in Surface Evolver and experiments, respectively. Bot images were taken form Ref [30]. (c) displays a wet foam from a forced-drainage experiment. In (d) more complex foam structures with internal spheres are shown. These structures were imaged using X-ray tomography in Ref [31].

investigated in close detail using X-ray tomography to accurately determine the position of each bubble [31]. It was observed that the outside bubble layer is ordered, with each internal layer resembling a different, simpler columnar structure. Two examples imaged with X-ray tomography are presented in Fig 1.8(d).

Transitions between different foam structures were also explored experimentally with two different techniques: The bubble diameter can be altered by adjusting the gas supply that creates the bubbles, changing the effective diameter ratio between tube diameter to bubble diameter. Structures can also be transformed by dilating or compressing the foam inside the tube. Pittet and Boltenhagen used both techniques to force structures into such crystallographic transitions [28, 37–39]. They examined them through experiments as well as simulations.

In a recent discovery by our collaborating Photographer Kym Cox, we found out that such foam structures can also be made of chain-like arrangement of soap bubbles without the confinement of a tube [40]. The soap bubbles self-assemble to such structures when being pushed out of a vertical tube. There they spontaneously arrange into various types of columnar structures (see example in Fig 1.9).

The left image of Fig 1.9 shows an image of such a bubble chain taken by Kym Cox. We were able to simulate the same structure using Surface Evolver (right image of Fig 1.9). In these simulations the structure is not confined by any cylindrical wall or confinement. Instead the top bubbles are fixed to a ceiling and the cylindrical symmetry is preserved by stretching the structure under gravity.

Similar experiments and simulation have been done for further cylindrical bubble chains. We conjecture that the chain structures are determined by the bubble to tube ratio for short chains. In short chains the gravitational force in vertical direction is approximately constant throughout the structure due

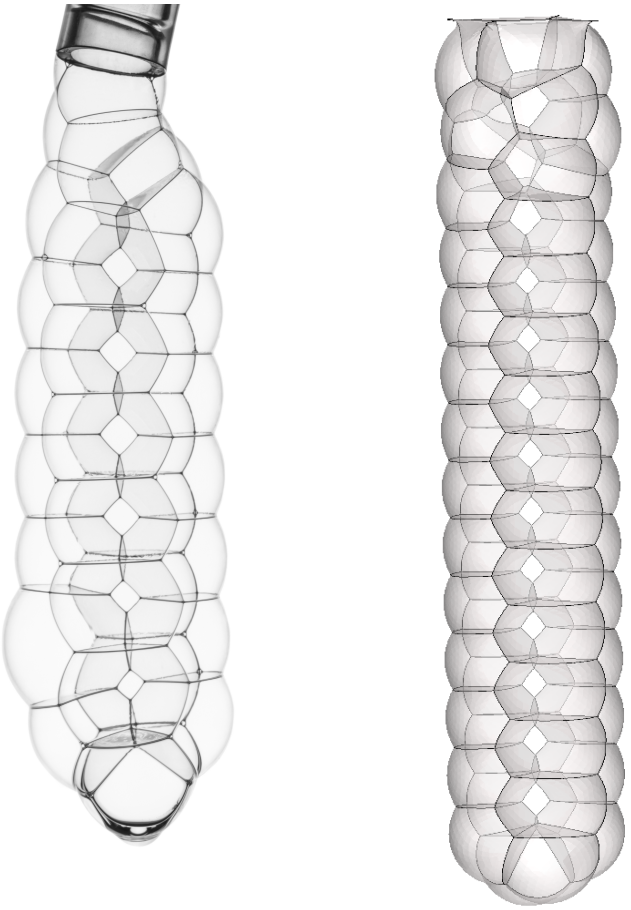

Fig 1.9: Photography/experiment (left) taken by the collaborating Photographer Kym Cox and Surface Evolver simulation (right) of recently discovered chain-like arrangement of soap bubbles which display columnar structures [40]. In the experiments monodisperse bubbles are slowly pushed out of a vertical tube, where they spontaneously self-assemble into columnar structures. In the Surface Evolver simulations, gravity was implemented to preserve the cylindrical symmetry.

to the heavy weight of the drop at the bottom (see left image of Fig 1.9). For longer chains each bubble will also experience a gravitational force due to the weight of all the bubbles below it. Thus, there will be a pressure gradient acting on the structure which might result in structure changes with structure length. However, a rigorous study of these structures and their assembly has not yet been published. We are currently preparing a manuscript on this study [40].

1.4.3 Nanoscience: Microrods and optical metamaterials

Up to now we have discussed the ubiquitous influence of columnar structures on botany and foam research. However, they are also increasingly recognised in physical sciences on smaller scale, particularly in nanoscience [16, 19, 41–44]. There they appear in a huge variety of man-made objects with the goal to create novel materials. For example, they are popular structures in the fabrication of nanowires, microrods, or microfibres [16, 18, 45, 46]. The structures can then determine the stiffness of such wires or fibres, as examined by Wood in his thesis [47].

Many researchers also tried to alter the properties of nanotubes by trapping identical particles inside them [15, 42, 43, 48–51]. These were mostly done by self-assembling fullerenes such as C60, C70, or C78 into carbon nanotubes (see also image at the bottom in Fig 1.5) [15, 48, 49], but also boron nitride nanotubes [43]. Thus, columnar structures were studied intensively in the context of nanotubes.

Fig 1.10 displays four images from different fields of nanoscience [16, 19, 52]. In this subsection we will describe those examples in greater detail and provide background about the research. While the previous examples from botany and foam research has little applications outside of their own research field, the examples from nanoscience may be applied to material science, such as liquid crystals or optical metamaterial.

Structures not too different from columnar structures occurred also in research with pharmaceutical background where particles were coated on the surface of a spherocylinder [52]. The incentive is to coat these drug particles as densely as possible on the spherocylinder to provide the best medical treatment. Thus, such structures in this context may play a vital role in drug deliveries. Lazáro *et al.* examined the morphologies of virus capsid

proteins self-assembled around metal nanorods through simulation as well as experiments [52]. One of their simulated packings on a spherocylinder is displayed in Fig 1.10.

Wu *et al.* built rods as illustrated in Fig 1.10(b) of the size of several microns (scale given in Fig 1.10(b)). These microrods are created by densely packing silica colloidal particles inside cylindrical pores. By solidifying the assembled structures the microrods were imaged and examined using scanning electron microscopy (SEM).

The assembly process consists of three steps. First, charged silica nanoparticles with a diameter of $d \sim 500\,\mathrm{nm}$ are deposited inside PDMS (Polydimethylsiloxane) nanopores of diameter $D = 1.8\,\mu\mathrm{m}$ and length $L = 8\,\mu\mathrm{m}$. Such particles are dispersed inside a photo-cross-linkable monomer of similar refractive index (ETPTA). Due to the Si particles' long-range repulsive interaction, they are called "soft colloids". This also gives them an effective diameter, dependent on the Debye length, which is much larger than their actual diameter.

Inside the PDMS pores they then assemble into ordered cylindrical structures. In order to achieve a variety of arrangements for the same pore and particle diameter, the concentration of particles is increased for different pores (at fixed pore length). In our simulation in chapter 3, this corresponds to a variation of the uniaxial pressure.

By UV-curing the samples in a second step, the ETPTA crosslinks, solidifying the dispersion inside the PDMS pores to a solid cylindrical rod. The assembled Si particles are locked into place within this cylindrical rod and the PDMS mold around those rods can be peeled off.

Since this leaves the columnar structure hidden inside the solidified ETPTA, one last step is needed to make the Si particle arrangement visible again. The outside polymer layer is removed by using oxygen plasma. With direct imaging techniques such as SEM, Wu *et al.* took images of the microrods as those seen

in Fig 1.10(b).

From a closer look at Fig 1.10 (b) one can observe a few distinct structures of their microrods. By increasing the concentration of nanoparticles inside the pores from 15 % to 40 %, they found 8 different dominant sphere packings. The simplest one was the $(2, 1, 1)$ or zigzag structure, but they also report on complex structures with a 1D internal column of particles. Fig 1.10(b) also shows the coexistence of multiple packings within one microrod. We will describe similar structures with this feature in chapter 4.

In order to demonstrate the ability to obtain a desired structure in a controlled way, Wu *et al.* compared their structures to Molecular Dynamics (MD) simulations. For the sphere interaction they used a pairwise-additive, long-range repulsive force, derived from a simple Yukawa potential. Similarly, wall interactions were implemented for the channel wall, as well as top and bottom. By varying the number of colloidal particles in the cylinder until reaching a steady state, they discovered the same structures as in the experiments. The nanoparticle concentration for the simulation was observed to be slightly smaller than that in the experimental structures.

Such microrods, whose physical properties such as stiffness or conductivity highly depend on the assembled columnar structure, can find applications in novel materials, such as liquid crystals, in the future. We will discuss the structure depends of the conductivity for line slips in chapter 2.3.2. In a liquid crystal, the percolation threshold (the lowest concentration at which a liquid crystal is conductive) is directly proportional to the conductivity of its constituents. The structure type of the microrod therefore directly influences this percolation threshold. Further possible applications of microrods with varying conductivity may also include organic solar cells [53] and optoelectronics [16].

Tanjeem *et al.* are currently investigating columnar structures with the long term goal to develop so-called optical metamaterials [54, 55], i.e. materials

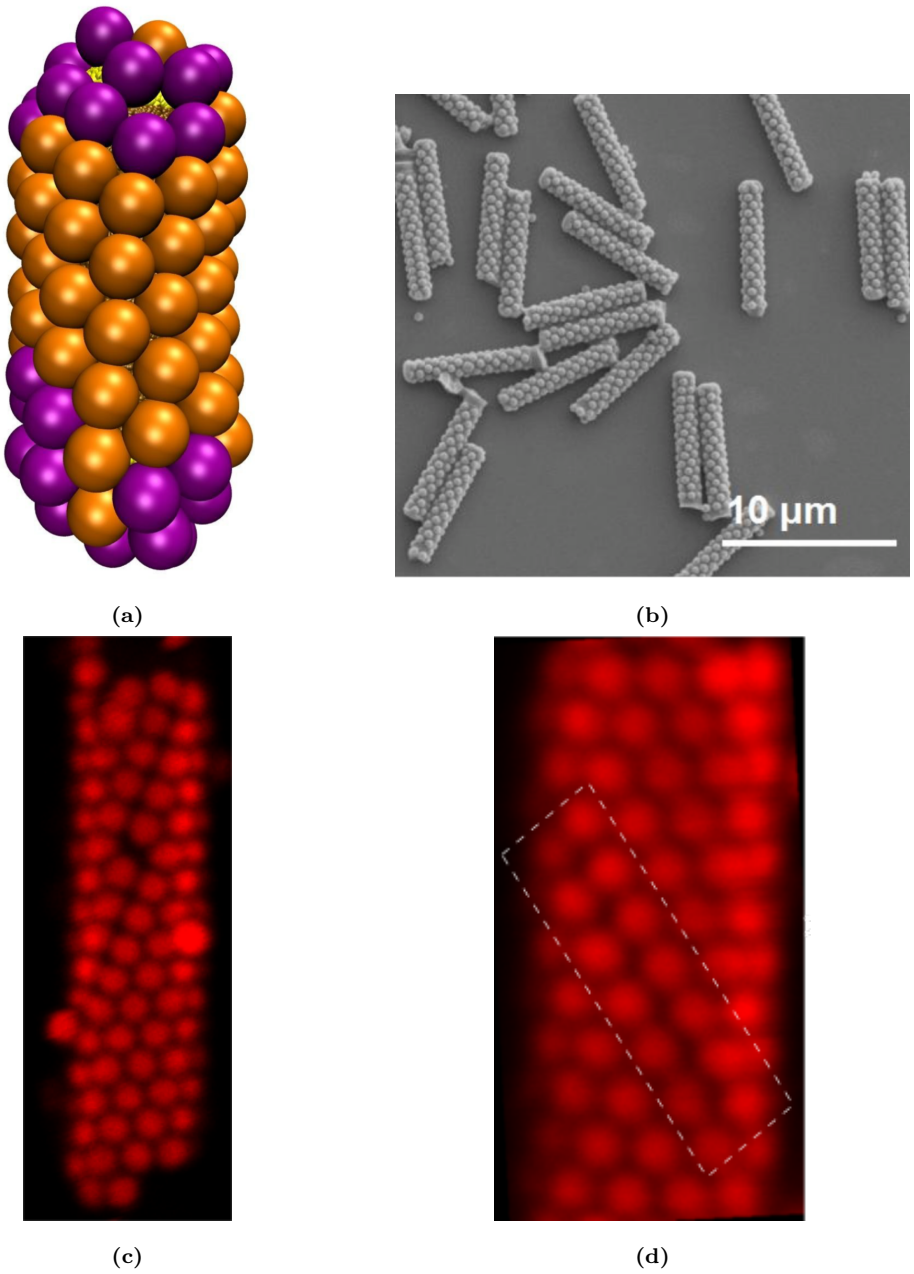

Fig 1.10: Examples of columnar structures in nanoscience. (a) Simulation of particles coated on the surface of a spherocylinder (length $L_{\mathrm{cyl}} \sim 45\,\mathrm{nm}$) where they are used for drug delivery (image taken from [52]). (b) Microrods of length of a few microns can be created by depositing Si nanoparticles inside PDMS pores (image taken from [16]). In (c) and (d) candidates of optical metamaterials are shown (images received in form of private communication from [19]). This is a material with a negative refractive index [19]. The structures are built by self-assembling nanocolloids ($d \sim 500\,\mathrm{nm}$) on the surface of a cylinder. A defect structure consisting of a line slip with a kink in (c) as well as a line-slip structure in (d) were discovered. Line slips will be discussed in detail in chapter 3.2.

with a negative refractive index. No material with such a property exists in nature, but they have been achieved in the past by man-made objects [56, 57].

Refraction of a light beam at the interface to a medium with a negative refractive index leads to a negative angle of refraction. Because of this property optical metamaterials find interesting applications in super lenses or optical cloaking [56, 58]. Super lenses have the ability to go beyond the diffraction limit and can thus be used for super-resolution imaging.

An optical metamaterial is composed of constituents that are smaller than the wavelength of light [55]. For visible light that means the elements must be smaller than 100 nm. Most metamaterials of current research operate for microwaves, which have a wavelength on the microscale and thus feature larger micro-scale structures.

These constituents act like resonators that strongly scatter incoming light of a certain frequency. This light is scattered isotropically which means that the resonance doesn't depend on the orientation of the resonator or the direction of the incoming light [55].

Tanjeem *et al.* are trying to construct such a resonator by self-assembling nanospheres on the surface of the cylinder [19]. The nanospheres ($d \sim 700\,\mathrm{nm}$) are therefore suspended in an SDS (sodium dodecyl sulfate) solution together with a cylinder of diameter D. A depletion force between the nanospheres and the cylinders sticks the spheres to the cylinder. For this effect, the cylinder diameter has to be much larger than the diameter of the nanospheres ($D/d \approx 3 - 5$). The diameter ratio for their structure is therefore above the limit of structures that we investigate in this thesis. However, their structures show nonetheless similarities.

Depending on D/d, Tanjeem *et al.* [19] found different crystalline structures, some of them being metastable. Fig 1.10(c) and (d) present two example structures at the same D/d. One of them is a ground-state line slip (image (d)) with one straight helical line (highlighted in (d)). This type of structure

(for smaller D/d) does also play a vital role in this thesis. Its features will be explained in detail in chapter 2.3.2.

They also discovered another type of line slip with kinks (see image (c)). From comparison with finite-temperature simulations, they found out that the kinks represent low energy excitations from the line-slip structure [19].

Due to the chiral nature of some columnar packings, such structures built out of nano-composites may also play an interesting role in nanoscience related to photonics [59, 60]. Chiral structures are those that have resemblance to a cork screw [such as the structure in Fig 1.10(c)], whereas achiral structures are symmetric around a rotational axis. A mathematical definition together with example structures from simulations are discussed in chapter 2.3.

Chiral structures possess special interesting optical properties that can be used for applications such as optical sensors or photonic crystals [53]. For instance, chirality is a necessary geometrical feature for building a beamsplitter that splits incoming light into s- and p-polarised light [61, 62]. Turner *et al.* [61] built such an optical device from a novel photonic crystal with a chiral asymmetry.

Of further interest in the context of photonic crystals are structures with a 4-fold symmetry. Those structures have a discrete rotational symmetry that the structure looks the same when rotated around the vertical axis by $\pi/2$. This particular rotational symmetry has the special property of destroying circular dichroism [63]. Circular dichroism describes the effect of a material that absorbs left- and right-handed light of a circular polarising light source to different amount. Saba *et al.* discovered that crystals with a 4-fold symmetry destroy this property, making this geometry an attractive design for photonic materials. Columnar structures with the phyllotactic notation of the form $(n4, n4, 0)$ possess such a 4-fold symmetry.

1.5 How this thesis advances the research field

For all these applications columnar structures have been intensively studied. Many experiments and simulations have been carried out to examine their occurrence in a specific scientific subject. This vast amount of previous investigations raises the question: *How can this thesis significantly advance the research field of columnar structures by using simulations as well as experimentally?*

Previous computer simulations such as the MD simulation by Wu *et al.* [16] replicated the full corresponding experimental process of assembling columnar structures. Therefore, the full movement of each sphere during this process is simulated, which makes the simulation computationally intensive as well as complex.

Many previous simulations also use a specific particle interaction that are exclusive for particular experiments. Troche *et al.* [15], for instance, used specific models to simulate the interactions between fullerenes. This allows a close comparison with corresponding experiments, but it also restricts such simulations to a particular experimental context.

We, however, perform throughout this thesis simulation methods that are based on generic models and therefore applicable to a variety of contexts. While they are only a first order approximation for the particle interaction, they still provide a good comparison between simulation and experiment for general columnar structures in equilibrium. Such concepts and generic models will be introduced in chapter 2.2.

Since we strictly search for structures in mechanical equilibrium instead of simulating the full movement of each sphere, our simulations are also computationally efficient as well as simple in the implementation. We therefore quickly achieve important information about the equilibrium structures. Those can then be compared to experimental structures or those simulated with more

complex algorithms.

The simplicity of the generic models also allows us in some parts to develop analytic calculations for columnar structures. Analytic calculations have the advantage that they do not require any computational power to predict information about equilibrium structures. Such calculations are carried out in chapter 4.2 to investigate columnar structures assembled in a process involving rapid rotations.

Both the efficiency of the computer simulations and transparency of the analytic calculations allow us to construct phase as well as stability diagrams for different types of assembly methods. These will play a major role in chapter 3 for computer simulations as well as in chapter 4 for analytic calculations. Phase and stability diagrams comprehensively convey information about the existence and stability of different columnar structures, respectively.

After the introduction of concepts and models in the following chapter, we investigate packings of soft spheres in chapter 3 using simulations as well as experiments of soap bubbles inside glass tubes. In chapter 4 we present a phase diagram derived from analytic calculation for a novel assembly process of columnar structures that involves rapid rotations. Chapter 5 then focusses on equilibrium configurations of spheres inside a cylindrical harmonic potential. These are investigated experimentally, as well as using a numerical scheme based on a generic model. In the last chapter, we conclude and summarise all our results and present an outlook for possible future work related to this thesis.

Chapter 2

Models and concepts for columnar structures

This chapter introduces the models and concepts that are needed to describe the type of columnar structures that we introduced in chapter 1. It will introduce the reader to important terminology used in later chapters and covers the simulation models, such as the hard and soft sphere models.

We start with introducing the concept of packing fraction ϕ. After explaining the concepts of soft and hard spheres, we look at different types of structures, including uniform and line-slip structures, which have previously been observed in columnar packings of hard spheres. We then discuss the previous work [14, 64, 65] on densest hard sphere packings where uniform and line-slip structures and their structural transitions have occurred. Since most simulation methods that we use in this thesis are based on minimisation algorithms, the most common ones for simulating columnar structures are reviewed at the end of this chapter.

2.1 The packing fraction ϕ

An important physical property of a dense packing of spheres in general is its packing fraction ϕ. The packing fraction is defined as the ratio of the total volume of a set of objects to the volume of the space into which they are packed. It is a measure for how efficiently the objects are packed into the given space.

In crystallography, this measure is a well established characteristics for different kinds of lattice packings of spheres such as the fcc (face-centred cubic), bcc (body-centred cubic), or hcp (hexagonal-close packed) lattices. Hales proved that the highest packing fraction achieved by such lattice packing of spheres in 3D is $\phi = \pi/3\sqrt{2} \approx 0.74$, which was already conjectured by Kepler [66]. The sphere packings arranged as fcc and hcp lattices achieve this packing fraction, while the packing fraction of sphere packings arranged as the bcc lattice is approximately $\phi_{\mathrm{bcc}} \approx 0.68$. Further types of lattices created by packings of spheres or ellipsoids together with their packing fractions were investigated and tabulated in Ref [67, 68].

The packing fraction is defined by the ratio of the total sphere volume to the volume of a unit cell, in which the spheres are packed. For ordered columnar structures, the total sphere volume is $N \cdot V_{\mathrm{sphere}} = N 4/3\pi \left(d/2\right)^3$, where N is the number of spheres and d the diameter of a sphere. The volume of the space into which the spheres are packed is defined as a volume of a cylindrical unit cell $V_{\mathrm{cell}} = L\pi \left(D/2\right)^2$ with length L and diameter D. The unit cell is the smallest portion of the periodic structure that shows the pattern of the entire ordered structure. The packing fraction is then calculated as

$$\begin{aligned} \phi &= \frac{N V_{\mathrm{sphere}}}{V_{\mathrm{cell}}} \\ &= \frac{2Nd^3}{3LD^2}\,, \end{aligned} \tag{2.1}$$

where d is the diameter of a sphere [14].

2.2 Hard vs soft spheres

As we have seen in the introduction, the spherical constituents of columnar structures vary from golf balls and tennis balls to berries, seeds, soap bubbles, emulsion droplets and micro- and nanospheres. All of these interact in different ways and require different interaction models if studied in detail. Soap bubbles for instance deform and change their shape when in contact (more details discussed in the outlook of chapter 6). Micro- and nanospheres are often described by the Lennard–Jones type of potentials, which consists of an attractive and a repulsive term [16, 45].

However, generic models are generally sufficient for a qualitative and semi-quantitative understanding of the structures formed. Throughout this thesis, we will use two generic models which are both based on a purely repulsive interaction: the *hard* and *soft sphere models*. By using purely repulsive models, we disregard any possible attractive interaction between the spheres which is the case for spheres with opposite charge. However, the spheres are then not identical anymore. Both, the hard and soft sphere models are introduced in this section.

They are both easy to implement and impress with their simplicity. Yet, packings of various constituents such as soap bubbles or colloidal systems have been simulated quite well to a first order approximation with these models. Especially the hard sphere model has already been used extensively for simulating columnar structures [14, 64, 65, 69–72].

2.2.1 The hard sphere model

The interaction model of hard spheres originates from simulating particles in statistical mechanics of fluids and gases [73, 74]. There, thermodynamic properties of hard sphere systems have been investigated analytically as well as with simulations.

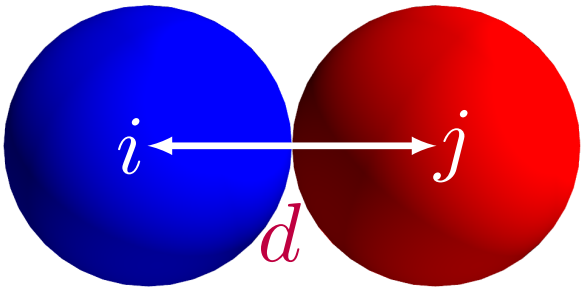

Fig 2.1: Illustration of the hard sphere model: Hard spheres do not overlap. The centre-centre distance between two hard spheres i and j of equal size is always at least the diameter d.

The interaction of two hard spheres is illustrated in Fig 2.1. Two hard spheres i and j cannot be closer together than the sum of their two radii. For spheres of equal size their closest centre–centre distance is equal to the diameter d. Hence hard spheres behave like impenetrable spheres and do not overlap. Their interaction energy is sometimes modelled as being binary. If two hard spheres are further apart than the sum of their radii, the energy is zero, otherwise infinity.

We use this model in chapter 5 to describe equilibrium configurations of spheres inside a cylindrical harmonic potential. The numerical results are then compared against experiments done with polymeric beads, which (as we will see) are impenetrable in our experiments and thus behave like hard spheres.

2.2.2 The soft sphere model

While previous theoretical studies of columnar structures are primarily done with hard spheres, our focus in chapter 3 and 4 lies on structures of deformable spheres. The major application of these investigations are soft matter systems such as foams, emulsions, but also many constituents from other research fields, such as colloids and nanoparticles have a soft repulsive interaction [16, 44, 45].

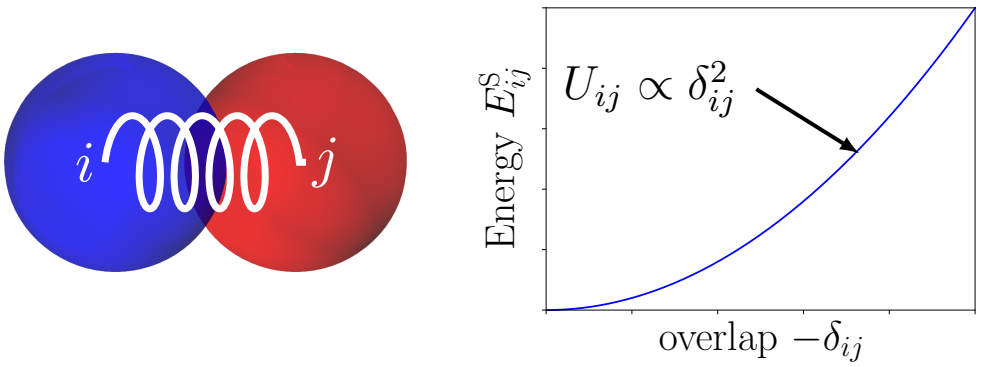

(a) **(b)**

Fig 2.2: Illustration of the soft sphere interaction. (a): Two soft spheres i and j interact like repelling spring, when they have an overlap δ_{ij} (See text for definition of overlap δ_{ij}). (b): Their interaction energy E_{ij}^{S} increases continuously with the overlap squared, $E_{ij}^{\mathrm{S}} \propto \delta_{ij}^2$. This models the deformation energy of each sphere due to the contact.

Opposite to the hard sphere model, two soft spheres can become closer together than the sum of their radii; hence they can overlap. We define the overlap δ_{ij} for two spheres of same diameter d as

$$\delta_{ij} = |\boldsymbol{r}_i - \boldsymbol{r}_j| - d\,, \tag{2.2}$$

where $\boldsymbol{r}_i$ and $\boldsymbol{r}_j$ are the centre positions of spheres i and j.

Two soft (monodisperse) objects, such as two bubbles, deform when they are pushed together closer than their diameter d. An interaction energy term can be ascribed to this deformation. In the soft sphere model this interaction energy E_{ij}^{S} between the ith and the jth spheres is modelled as a function of the square of the overlap δ_{ij}, if the two spheres are overlapping (and otherwise the energy is zero). In detail, the interaction energy between to soft spheres is

$$E_{ij}^{\mathrm{S}} = \begin{cases} 0 & \delta_{ij} > 0 \\ \frac{1}{2} k \delta_{ij}^2 & \delta_{ij} \leq 0 \end{cases} \tag{2.3}$$

where k is a constant.

This is the same energy as in Hook's law for a harmonic repelling spring,

where k is the spring constant. Thus, two overlapping soft spheres repel each other like a harmonic spring (see illustration of Fig 2.2(a)).

Since we are minimising the interaction energy in our simulations, this model can be interpreted as follows: Unlike the hard sphere model, soft spheres can overlap, but their overlap is penalised with an interaction energy in the overlap squared. Its continuous interaction energy is also illustrated in Fig 2.2(b).

The softness of the spheres is determined by the spring constant k. Thus, results from the hard sphere model can be recovered in the limit $k \to \infty$. We can validate our soft sphere simulations by checking the results in the hard sphere limit against previous hard sphere results [14].

The property of being a pairwise potential makes it easy to implement and efficient in run time. Despite, or because of this simplicity, this model has become the most commonly used tool to simulate foams and emulsions since its introduction to the foam research by Durian in 1995 [75]. In fact, due to its good agreement in reproducing the Herschel–Bulkley type rheology, which is associated with emulsions and foams, scientists in foam research became accustomed to believe that it is a good representation of a foam or emulsion.

The soft sphere model is based on the similar assumption as the model of Hertzian contacts which is used to describe contacts of elastic solids. For both models, the strains are within the elastic limit and the area of contact is much smaller than sphere diameter. Any type of friction for the surfaces of the spheres are in general neglected. However, sliding friction between two spheres can be added to the soft sphere model by introducing pairwise friction forces between two contacting spheres. This can only be done in Molecular Dynamic (MD) simulations. We, however, use an (energy) minimisation approach that does not consider friction because we only focus on the (mechanical) equilibrium structure. For systems of soap bubbles or emulsion droplets that are our major application purposes, this is a valid approximation.

However, its limits for simulating such deformable objects are obvious. The soft sphere model lacks volume conservation, since the overlaps reduce the effective volume of the spheres. When a bubble or emulsion droplet is compressed at top and bottom, it bulges out at the side and the volume of soap is conserved in first approximation. The pairwise interaction, as used in the soft sphere model, is also not an accurate description of a bubble in a foam [76, 77]. We discuss the limits of this model in regard to foams and emulsions in the outlook of chapter 6.

The great advantage of the soft sphere model over other foam and emulsion simulations such as the Surface Evolver [35], `plat` [78], or the recently developed Deformable Particle Model (DPM) [79, 80] is its simplicity and computational efficiency. The three other mentioned simulations model bubbles in a foam by films or vertices. Because of the high number of films and vertices, the former models are usually computationally inefficient in time and space complexity. The soft sphere model, on the other hand, simulates a foam by approximating each bubbles as a sphere.

2.3 Different types of columnar structures

In previous simulations many different types of packings have been observed when hard spheres of diameter d are packed inside cylinders with diameter D [14, 64, 65, 71, 72]. Some of these observed structures can be completely metastable such as helical defect packings [81]. However, in this thesis we will only focus on dense and ordered packings that are stable for at least one value of D/d.

Ordered columnar structure can be grouped together in different ways. One form of categorising them is using their chirality. Some of these structures are chiral, while others are achiral. Chiral structures have a screw symmetry (like a cork screw), i.e. the chiral structure forms helices around the vertical

axis. In mathematical terms, a chiral structure cannot be mapped onto their mirror images by either rotation or translation alone, while achiral structures possess this symmetry property. We point out an example of a chiral and achiral structure in Fig 2.5 of section 2.4.

We group these structures in two different categories: *uniform* and *line-slip* arrangements.

2.3.1 What is a *uniform* structure?

One of the dense columnar structures that will play a crucial role in this thesis is the uniform structure. Its features are best explained with the aid of an example as given in Fig 2.3. The presented example here is a so-called $(3, 2, 1)$ uniform structure. The triplet of phyllotactic notation can be derived from the periodicity vector $\boldsymbol{V}$ and the two pink lattice vectors, shown in Fig 2.3(c) (see explanation in Introduction 1.3).

Its sphere packing in Fig 2.3(a) already indicates its symmetric shape. Fig 2.3(b) shows the corresponding contact network of the cylindrical structure. Each blue and red dot on the surface of the cylinder represent a sphere in the packing of Fig 2.3(a) and each black line corresponds to a contact between adjacent spheres. It indicates that each sphere has the same number of contacting neighbours in a uniform packing which gives each sphere an identical neighbourhood. In the example of Fig 2.3 each sphere has six contacts.

Rolling out this contact network into a plane of height z and azimuthal angle θ of each sphere leads to the regular hexagonal (or triangular) lattice of Fig 2.3(c). Each dot in this pattern represents again a sphere of the packing and each line a contact between adjacent spheres.

A regular hexagonal lattice such as in Fig 2.3(c) is therefore the characterising feature of a uniform structure. The reason for the uniform structure forming a hexagonal lattice is due to the fact that it maximises the number of contacts. For different uniform structures (l, m, n) the pattern of Fig 2.3(c)

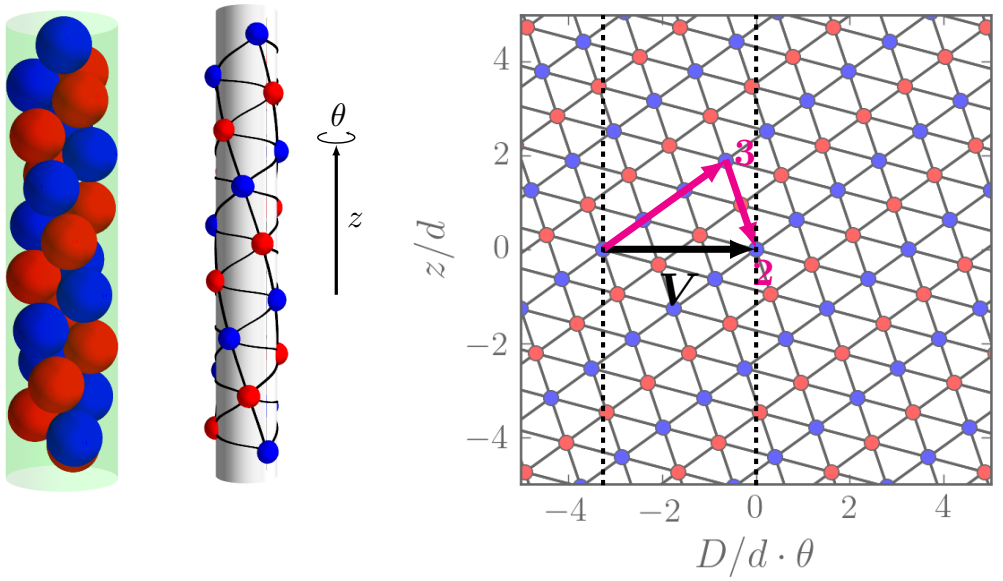

(a) (b) (c)

Fig 2.3: Illustration and explanation of a uniform structure with the aid of an example. Fig (a) shows the sphere packing of a $(3, 2, 1)$ uniform structure, (b) is its corresponding contact network, where each dot represents a sphere and each line a contact between spheres. Fig (c) is the contact network rolled out into a plane of height z and azimuthal angle θ, showing a regular hexagonal lattice. From (b) and (c) one can observe that each sphere has six contacts, giving them an identical neighbourhood. The periodicity vector $\boldsymbol{V}$ and the lattice vectors are drawn in (c) (see Introduction 1.3 for explanations).

only varies by a rotation in the z-θ plane. Each uniform structure is thus distinguished by its periodicity vector $\boldsymbol{V}$, which is given by the phyllotactic triplet (l, m, n) (see chapter 1.3).

In the hard sphere limit, uniform structures can only occur at certain precise values of diameter ratio D/d. These values can be calculated analytically for some of the uniform structures where all spheres are in a horizontal plane [14]. The calculations are performed by reducing the packing problem to one of packing circles inside circles.

2.3.2 What is a *line-slip* structure?

For each uniform structures, there also exists a related but different structure, called a line-slip arrangement. We will explain its features again with the aid of an example in Fig 2.4 and also hint at possible applications from chapter 1.4.3.

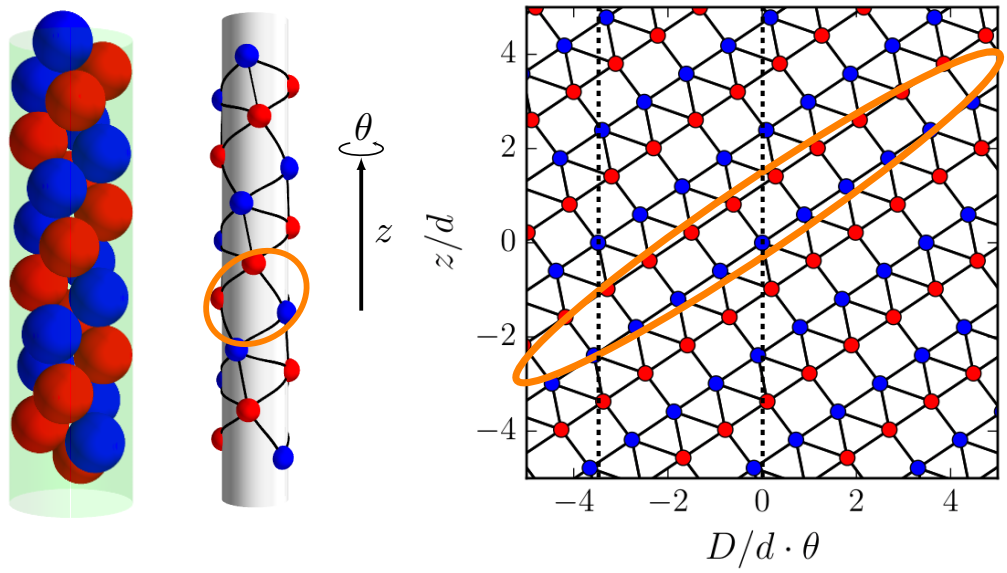

Fig 2.4: Illustration and explanation of line-slip arrangement with the aid of an example. Fig (a) shows the sphere packing of a $(3, \mathbf{2}, 1)$ line slip. (b) is its corresponding contact network, where each dot represents a sphere and each line a contact between spheres. Highlighted here is the gap or loss of contact between certain neighbouring spheres. Fig (c) displays the contact network rolled-out into a plane of height z and azimuthal angle θ. It reveals that the gaps or loss of contacts occur along a line between the red coloured and blue coloured spheres; hence the name line-slip structure.

The differences between uniform and line-slip structures are marginal and difficult to spot from the sphere packings of a $(3, \mathbf{2}, 1)$ line slip [see Fig 2.4(a)] compared to a $(3, 2, 1)$ uniform structure [see Fig 2.3(a)]. However, comparing Fig 2.4(b) with 2.3(b) reveals a difference in the contact network of a line slip towards a uniform structure: certain lines are missing, such as the one

highlighted by the ellipse in Fig 2.4(b). The spheres in Fig 2.4(b) are again represented by red and blue dots, while the connecting lines are contacts. While all spheres in a uniform structure have the same number of contacts, spheres in a line slip can have different numbers of contacts with neighbouring spheres. For the $(3, \mathbf{2}, 1)$ line slip, some spheres have five and others six contacts. Thus a line slip structure is characterised by these gaps or loss of contacts.

Rolling out the contact network again in the z-θ plane leads to the pattern in Fig 2.4(c). The missing lines in this pattern compared with Fig 2.3(c) reveal that these losses of contacts occur along a line; hence the name *line*-slip structure. This feature was first identified by Picket *et al.* [82], but not termed *line slip*.

The bold number in the phyllotactic notation of a line slip, such as $(3, \mathbf{2}, 1)$, gives rise to the direction, in which the losses of contacts occur. Since each number represents one of the lattice vectors in the hexagonal lattice, the index of the bold number indicates the direction of the gaps in Fig 2.4(c). In the given example of a $(3, \mathbf{2}, 1)$ line slip, a row of contact losses is followed by **two** rows (red and blue) of spheres without loss of contacts.

By shearing the row of red dots against a row of blue dots in this example, one can generate again two uniform structures related to one line slip. Thus, each line slip is related to two adjacent uniform structures, one at a higher and one at a lower diameter ratio D/d. Throughout this thesis, we use the convention that each line slip is labelled by the related uniform structure of *lower* D/d [14].

This shearing in the hard sphere limit is equivalent to varying the diameter ratio D/d, explaining why the structures are intermediate between uniform arrangements. Thus, different to uniform structures, line slips can occur in a range of D/d values in the hard sphere limit (see also table A.1 in Appendix A.1). As described in more detail in section 2.4, a line slip always has a lower

packing fraction than its related uniform structures.

Since line slips exist over a range of diameter ratios, the gap between adjacent spheres in a line slip can finely be adjusted by varying D/d or pressure p. This gives line slips special features with huge potential. Physical quantities such as packing fraction, stiffness, or conductivity of the column vary with the extent of the gap (and thus with D/d or p).

Wood investigated the bending stiffness of cylindrical crystals in his thesis [47]. He used Molecular Dynamics (MD) simulations to first assemble spheres on the outside of a cylindrical rod. He then calculates the stiffness of a variety of structures by deforming the rod into an arc of different curvatures.

The conductivity of such structures may be calculated theoretically using Kirchhoff's rules. From the contact network an electrical circuit plan may be abstracted, in which each contact is a resistance and each sphere is knot connecting the resistances. A gap or loss of contact constitutes a capacity in this circuit that depends on the gap size of the line slip. By using Kirchhoff's rules, the conductivity as well total resistance can be calculated.

The special feature of a line slip holds huge potential for novel materials like microrods or polymers as introduced in chapter 1.4.3. Stiffness and conductivity play an important role in those materials, especially for microrods that make up liquid crystals. Thus, creating these materials from line-slip structures might make it possible to finely adjust their stiffness and conductivity. This may help to improve liquid crystals where stiffness and conductivity define properties such as the percolation threshold at which the liquid crystal becomes conductive. Since both properties can be adjusted with gap size, an optimal microrod for such a liquid crystal may be constructed out of a line slip.

2.4 Densest hard sphere packings inside cylinders

Mughal *et al.* studied the densest packing of hard spheres using the simulation method of simulated annealing (see section 2.5.2) [14, 71, 72]. These structures are all screw periodic, i.e. they can be simulated by using a unit cell that is repeated to get an infinitely long column. They described and tabulated all structures in detail up to the diameter ratio of $D/d = 2.873$ for cylinder diameter D to sphere diameter d [14]. This also includes some structures with internal spheres that are not in contact with the cylinder wall. For purposes of coherence, this table is included as table A.1 into the Appendix A.1.

They calculated the packing fraction for all these tabulated structures as a function of D/d (see also Fig 2.5). At the diameter ratios, where the peaks occur in the packing fraction (dashed vertical lines), are the *uniform* structures. Some of them, labelled by their phyllotactic notation, are displayed with arrows indicating the point on the curve where they exist. In-between those the structures of high packing fractions are the line slips, which have a lower packing fraction than the uniform structures. Both structures are explained in greater detail in previous sections 2.3.1 and 2.3.2, respectively.

Note that the packing fractions of all the structures in Fig 2.5, are below $\phi < 0.55$. This is significantly smaller due to the free volume left by the cylindrical confinement than the packing fraction of the unconfined lattice packings such as fcc, bcc, or hcp.

Mughal *et al.* [14] also discovered that structures where all spheres are in contact with the cylinder wall can be related to disk packings on an unrolled surface of a cylinder. The related contact network of the disk packing and the rolled-out contact network of sphere structure are the same. For $D/d > 2$, these 2D disk packings resemble the same structures as the 3D sphere packings. Similarities in the structures can be seen by comparing the

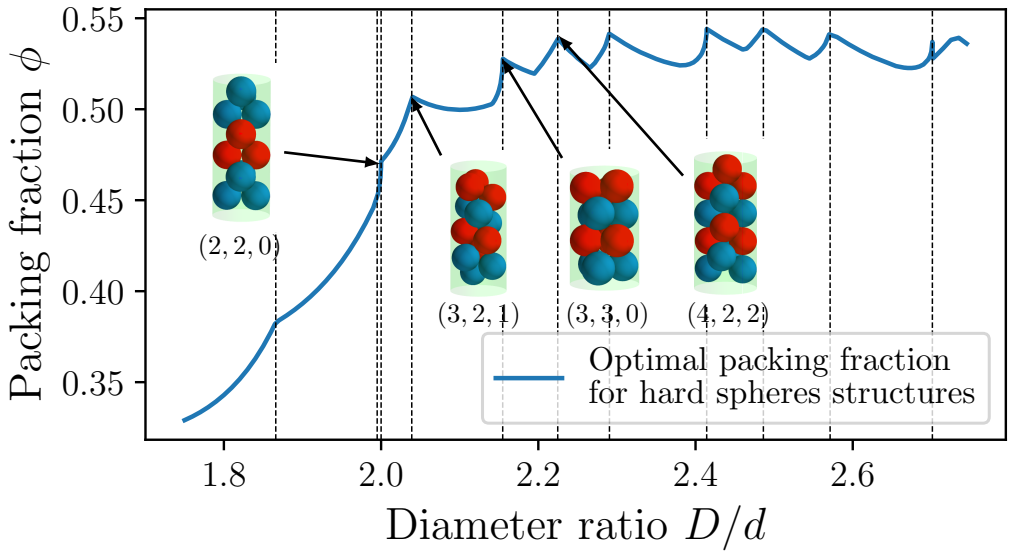

Fig 2.5: Optimal packing fraction ϕ for hard spheres packed inside a cylinder as a function of the diameter ratio D/d (tube diameter D to sphere diameter d) [14]. The structures at the peak positions, indicated by the black arrows, are uniform structures. The optimal packing fraction between those points have intermediate line-slip arrangement. The displayed $(3, 2, 1)$ uniform structure is an example of a chiral structure, whereas the $(3, 3, 0)$ uniform structure is achiral. Line-slip and uniform structures are explained in section 2.3. The image is reconstructed from data take from Ref [14].

contacts of each disk or sphere inside the packing. These similarities are explained by looking at a cut of a cylinder through the centre of a sphere. For small cylinders this cut is an ellipse, but for increasing cylinder diameters the curvature of the cylinder wall decreases and it approaches a disk shape. Thus, a projection of a sphere on a cylinder wall approaches disk shape for large diameter ratio D/d. This reduction of a 3D sphere packing problem to a 2D disk packing problem allowed them to define rules for possible transitions between uniform structures of different phyllotactic indices.

For spheres as well as disk packings, it was found that different uniform structures are connected with each other by line slips. All possible transitions were summarised in a diagram for the 3D case and one for the 2D case [14].

Since we make use of these two diagrams throughout this thesis, they are attached in the Appendix A.1. They show the surface density (in 2D) and the packing fraction (in 3D) for all the uniform structures and their stable and also metastable intervening line slips.

Fu *et al.* [65] vastly extended Mughal *et al.*'s table of densest hard sphere packings in terms of diameter ratio D/d. They identified all dense packings of hard spheres up $D/d = 4.0$ by using a linear programming algorithm (see section 2.5.2). Above the Mughal-*et al.* regime, they discovered 17 new dense structures with internal spheres that are not in contact with the cylinder wall.

Fu *et al.* also extended Mughal *et al.*'s results on how hard sphere packings inside cylinders are related to each other [64]. They investigated structural transitions between different uniform structures using linear programming and summarised their results in a schematic plot Fig 2.6.

Each image of a columnar structure in Fig 2.6 corresponds to a different uniform structure. Each of them is labelled by the phyllotactic notation (l, m, n). The black arrows indicate their sequential appearance in the list of structures of highest packing fraction, sorted by increasing diameter ratio D/d (compare Fig 2.5). The red dashed arrows, however, indicate the favourable sequence of structure, when D/d is increased continuously from starting in a given uniform packing. The sequence of structure at various D/d is found by seeking the highest density configuration.

For instance, the $(3, 2, 1)$ uniform structure favours a transition to the $(4, 2, 2)$ uniform structure over the $(3, \mathbf{2}, 1)$ line slip, when increasing D/d (indicated by the red arrow). However, Fig 2.5 shows that the $(3, 3, 0)$ uniform structure follows the $(3, 2, 1)$ uniform structure in the sequence of a uniform structure with highest packing fraction.

We greatly extend these investigations in chapter 3.3.3 on structural transition by not only investigating sequences upon increasing D/d, but also decreasing D/d. This allowed us to find a cyclic pattern within this network

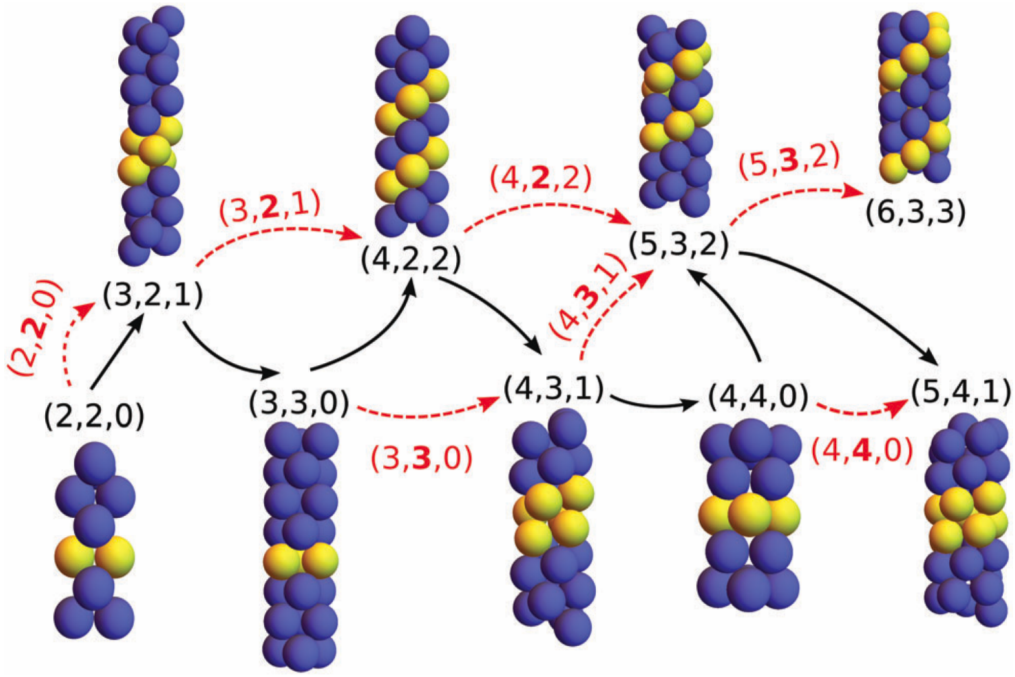

Fig 2.6: Schematic plot of simulated transition sequences between uniform structures, labelled by their phyllotactic notation, and line slip relationship (indicated by the arrows) [64]. Black lines indicate the structures of highest packing fraction with increasing diameter ratio D/d (compare with Fig 2.5). Red dotted arrows show the dynamically favourable sequence, observed from simulation. [image taken from [64].]

of structural transitions.

2.5 Simulation techniques: Minimisation algorithms

Many different types of algorithm have been used in the past to simulate columnar structures. They varied from search tree construction [69], Molecular dynamics (MD) simulation [8, 16], over sequential depositioning [70] to minimisation/optimisation algorithms such as simulated annealing [14] or linear programming [65]. In this section we introduce a few important example algorithms of the latter kind. Such methods simulate columnar structures by either minimising a potential (such as the energy or enthalpy) or seeking for the highest hard sphere packing fraction, starting from a given initial configuration.

Optimisation algorithms can be categorised into two groups: *Local* and *global* optimisation routines. The first is seeking for the nearest optimum from a given initial position/configuration and the latter searches for the optimum in the full given parameter range. Each optimisation problem can always be interpreted as a minimisation problem. Thus, we will briefly explain the following example algorithms in terms of minimising a given multidimensional function $\mathtt{E}(\boldsymbol{X})$, which can be the energy, enthalpy, or unit cell length of the columnar structure simulation. The vector-like parameter $\boldsymbol{X}$ in these simulations usually contains all sphere coordinates.

2.5.1 Local minimisation routines

Gradient descent: The simplest algorithm in finding the (local) minimum of a function $\mathtt{E}(\boldsymbol{X})$ is the gradient descent (or steepest descent) algorithm. It is based on the gradient $\boldsymbol{\nabla}\mathtt{E}(\boldsymbol{X})$ of this function (see Appendix A.2 for definition of the gradient)[1]. The gradient taken at a given parameter vector

[1]When the function to be minimised is a potential, the gradient can be interpreted as a force vector of the system.

$\boldsymbol{X}$ has the property of pointing into the direction of steepest ascent.

Thus, by iteratively taking steps into the negative direction of the gradient, one eventually ends up in a local minimum of the function. At this point the gradient is zero.

The strength of the gradient descent method lies in its simplicity and robustness. It can easily be implemented and not much information about the multidimensional function $\mathtt{E}(\boldsymbol{X})$ is necessary. The only additional information besides $\mathtt{E}(\boldsymbol{X})$ is the gradient which can also be calculated numerically. Thus, it is best used for testing one of the more sophisticated methods on correctness.

However, this iterative algorithm needs many steps to terminate when the function $\mathtt{E}(\boldsymbol{X})$ around the minimum is shallow, i.e. the gradient converges slowly to zero.

BFGS algorithm: A more sophisticated local minimisation routine is the BFGS method, named after Broyden, Fletcher, Goldfarb, Shanno [83]. It belongs to the class of quasi-Newton algorithms, which are an advancement of the conjugate gradient algorithms.

These type of algorithms use the Hessian matrix of the function $\mathtt{E}(\boldsymbol{X})$ as additional information to locate the nearest minimum. The Hessian contains information about the second derivative of the function to be minimised (see Appendix A.2 for the definition of the Hessian). A Newton method that approximates the Hessian numerically is referred to as a quasi-Newton method.

The minimum is found in an iterative procedure, in which a matrix equation involving the Hessian is solved. The BFGS method directly approximates the inverse of the Hessian and terminates the iteration when the gradient is zero.

This method is much more efficient in finding the nearest local minimum than the gradient descent method. Its efficiency comes at a cost of complexity. Additional information such as the gradient and the Hessian of the function

$\mathtt{E}(\boldsymbol{X})$ are used in this method. When these additional information are calculated numerically, it has a great advantage due to higher efficiency over the gradient descent method.

Since we make use of this algorithm throughout the thesis, it is explained in more detail in the Appendix A.2. We describe each step of the algorithm with pseudo-code.

2.5.2 Global minimisation routines

Linear programming: Fu *et al.* obtained their results of columnar hard sphere packings by using an optimisation routine called linear programming [64, 65]. With this method, they managed to significantly extend Mughal *et al.*'s results on the densest structure depending the diameter ratio D/d (see also previous section 2.4).

Linear programming methods are used for optimisation problems that can be formulated as: *Minimise a linear objective function subject to linear equality and inequality constraints.*

In the packing problem of hard spheres within a cylinder the function to be minimised is the volume of the unit cell, which depends on its length L. The constraints are given by the hard spheres. Searching for the optimal hard sphere packing inside cylinders can thus be stated as the following linear programming problem: *Minimise* L subject to the two constraints

- no overlaps between spheres
- no overlaps with the cylinder walls.

Linear programming is a fast and efficient, but also very sophisticated method to locate the correct global minimum of a function with a high accuracy. Due to the constraint of no overlaps, this type of algorithm however is restricted to simulations of hard sphere packings.

Simulated annealing: Mughal *et al.* used simulated annealing to search for the densest hard sphere packings in previous work [14] (see also previous section 2.4). This is a probabilistic minimisation routine that seeks the global minimum of a given function. Its approach is based on the metallurgic process of heating a metal and cooling it slowly down to avoid defects or metastable states [84].

By starting from random sphere positions, it moves the sphere positions randomly. If the movement lowers the function's value, the step is always accepted. Otherwise the step is accepted with a probability criterion dependent on a temperature T, allowing it to leave local minima. The most common acceptance criterion is the Metropolis criterion (see Appendix A.2 for details), which was also used in Mughal *et al.*'s investigations. During the optimisation, the temperature is gradually decreased according to an annealing schedule. In Mughal *et al.*'s simulations this schedule was either linear (i.e. dropping the temperature in fixed intervals) or on a logarithmic scale (e.g. $0.1, 0.09, 0.08 \ldots 0.01, 0.009, 0.008 \ldots$). At $T = 0$ it then settles hopefully in the global minimum of the function.

Using a slow enough annealing schedule this method is able to find the correct global minimum with high accuracy. Similar to the gradient descent algorithm, its greatest advantages are its simplicity and robustness. In fact, at zero temperature when only movements that lower the function's value are accepted, the simulated annealing method performs the gradient descent algorithm. Thus, it has the same disadvantages as gradient descent of being slow and inefficient.

This algorithm was used to minimise the soft sphere energy of a packing [14]. A hard sphere packing is generated when the soft sphere energy is zero and no spheres overlap. For the final structure, the one with the highest packing fraction is then chosen to create Fig 2.5.

Basin-hopping: However, simulated annealing can be improved by combining it with a local minimisation method. This is the basic approach of the Basin-hopping method [85, 86]. It seeks for the global minimum similarly to simulated annealing with a probabilistic approach, but during each iteration it performs a local minimisation.

Each iteration consists of a cycle with three important steps:

1. random perturbation of the parameter vector $\boldsymbol{X}$
2. performance of local minimisation
3. accept or reject the new parameter vector based on the new local minimum.

The acceptance criterion is similar to that of simulated annealing. The new parameter vector is accepted if the new minimum is lower than before. Otherwise a probability criterion such as the Metropolis criterion is used again. The iterations of these steps are performed for a given number of steps, ensuring the termination of the algorithm.

Since we use the BFGS method as local minimisation in the Basin-hopping algorithm, it has similar strength than the BFGS method: the Basin-hopping algorithm finds the correct global minimum fast and efficiently with high accuracy.

We use this minimisation method during this thesis, wherever we are interested in stable structure with a global minimum in energy (or enthalpy). A detailed description of it is given in Appendix A.2.

Chapter 3

Soft sphere packings in cylinders

Related publications:

1. J. Winkelmann *et al.* Phys Rev E **97** 059902 (2017).
2. J. Winkelmann *et al.* Phys Rev E **98** 043303 (2018).

In their most elementary form, columnar structures arise when spheres are packed densely inside (or on the surface of) a cylinder [14, 65, 70–72, 81, 87]. In the previous chapter 2.2.1 we discussed hard sphere structures that were previously investigated and assembled with this method. All of those structures up to $D/d < 2.71486$ (i.e. structures without internal spheres) have been identified and tabulated [14] depending on their diameter ratio D/d (see Table A.1 in Appendix A.1 for Table 1 from Ref [14]). D is here the cylinder diameter and d the diameter of the spheres. Above $D/d = 2.71486$ the nature of the densest sphere packing changes and structures with internal spheres, not in contact with the cylinder wall, occur.

For discrete values of D/d, hard spheres assemble to a uniform structure, labelled with the phyllotactic indices (l, m, n) – see Introduction 1.3 for explanations. Between these values, the structure is best accommodated by the

introduction of a line slip, which shears two adjacent spirals with a loss of contacts. Both structures are explained in detail in the previous chapter 2.3.

We have become accustomed to thinking of line slips as being a property of *hard* spheres, and therefore of limited relevance to real physical systems. That point of view is reconsidered in this chapter: we experimentally demonstrate the existence of line-slip arrangements in wet foams with high liquid fraction. These observations constitute the first conclusive experimental evidence of such structures (discounting the trivial case of packing ball-bearings in tubes [14]). Furthermore, our experiments with foams demonstrate that line-slip structures can be stable in *soft* systems; a hitherto unexpected outcome due to the lack of discovery in the past. Our work is stimulated in part by the observation of line slips (albeit rather indistinctly) in some simulations, which use microscopic particles interacting by (the relatively complex) Lennard–Jones type potentials [9, 45].

We extend the previous hard sphere results to soft repelling spheres by allowing the spheres to overlap. But the overlap is penalised with an increase in interaction energy as a function of the square of the overlap (see section 3.1 for simulation details). Such soft sphere structures then not only depend on the diameter ratio D/d, but are also subject to an applied uniaxial pressure P. We present a phase diagram in terms of these two parameters, displaying stable structures of lowest enthalpy.

However, it is recognised that these might be of limited value for macroscopic experiments. Accordingly we have additionally undertaken an exploration of metastability and hysteresis by carrying out further simulations. That is, we ask the question: *Given a certain structure, locally stable, and some (experimental) protocol for the continuous variation of D/d, what transitions are to be expected?*

We answer this question by first investigating an example of a reversible structural transition in closer detail. The results are presented in form of a

stability diagram. The full picture of all structural transitions are then displayed in form of a directed network, showing all possible transitions between structures provided in the phase diagram.

3.1 The simulation model: Minimisation of enthalpy H

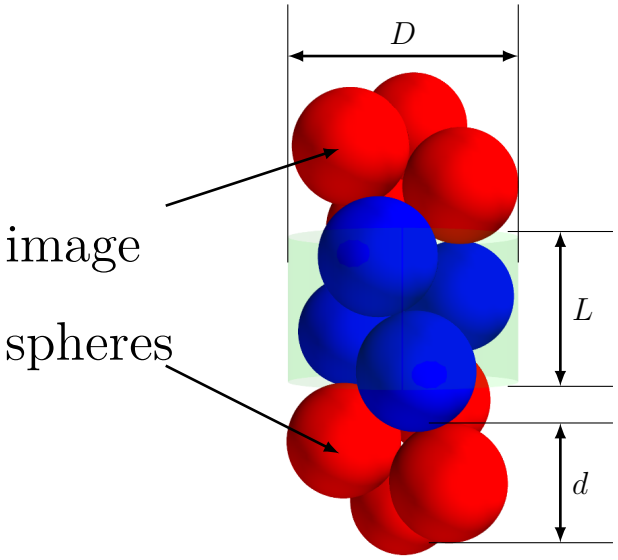

Fig 3.1: Simulation set-up of N soft (overlapping) spheres (blue) with diameter d confined inside a cylinder with a unit cell of diameter D and length L. In order to simulate an infinite column of soft spheres with periodic boundaries, image spheres above and below the unit cell are used. These spheres are not only moved up and down by L and $-L$, respectively, but also rotated by a twist angle α and $-\alpha$, respectively.

To simulate soft spheres packed inside cylinders we use the *soft* sphere model [75] that we explain in detail in chapter 2.2.2. This model consists of spheres with diameter d, whose overlap δ_{ij} leads to an increase in energy E_{ij}^{S} according to

$$E_{ij}^{\mathrm{S}} = \begin{cases} 0 & \delta_{ij} > 0 \\ \frac{1}{2} k \delta_{ij}^2 & \delta_{ij} \leq 0 \end{cases} \tag{3.1}$$

The overlap between two spheres i and j is defined as $\delta_{ij} = |\boldsymbol{r}_i - \boldsymbol{r}_j| - d$, where $\boldsymbol{r}_i$ and $\boldsymbol{r}_j$ are the centres of two contacting spheres.

A harmonic energy term

$$E_i^{\mathrm{B}} = \frac{1}{2}k((D/2 - r_i) - d/2)^2 \tag{3.2}$$

accounts for the overlap between the ith sphere and the cylindrical boundary. The parameter r_i is the radial distance from the central axis of the ith sphere. The sphere-to-wall interaction is therefore similar to the sphere-to-sphere interaction. The spring constant k determines the softness of the spheres.

We conduct simulations using a unit cell of length L (volume $V = \pi(D/2)^2 L$), containing N spheres as illustrated in Fig 3.1. On both ends of the unit cell we impose *twisted* periodic boundary conditions to represent a screw periodic columnar structure of soft spheres. The periodic boundaries are implemented by placing image spheres above and below the unit cell, where each sphere of the unit cell is moved in z-direction by L (and $-L$) and twisted by an angle α (and $-\alpha$, respectively) in the x-y-plane. Only the overlap energies $E_{ij}^{\mathrm{S}'}$ between image spheres i and spheres j inside the simulation cell contribute to the overall internal energy, i.e. image spheres do not interact with each other.

Stable structures are found by minimising the enthalpy $H = E + PV$ for a system of N soft spheres in the unit cell, where E is the internal energy due to overlaps as described before and P is the pressure. The internal energy $E = E^{\mathrm{S}'} + E^{\mathrm{S}} + E^{\mathrm{B}}$ consist of the soft-sphere energy $E^{\mathrm{S}'}$ between spheres in the unit cell and their image sphere, the interaction energy E^S between each sphere within the unit cell, and the sphere-to-wall interaction E^{B}. The enthalpy H is thus calculated as

$$H(\{\boldsymbol{r}_i\}, L) = \underbrace{\frac{1}{2}\sum_{\substack{i,j=0 \\ i\neq j}}^{N} E_{ij}^{\mathrm{S}'} + \frac{1}{2}\sum_{\substack{i,j=0 \\ i\neq j}}^{N} E_{ij}^{\mathrm{S}} + \sum_{i=0}^{N} E_i^{\mathrm{B}}}_{E} + \underbrace{PV}_{\text{pressure term}} . \tag{3.3}$$

During the minimisation, the $3N + 2$ free parameters are the centres $\{\boldsymbol{r}_i\}$ of

the N spheres, the twist angle α, and the length of the unit cell L, while the pressure P is kept constant. Thus, all simulations are performed at a constant pressure and a variable volume.

In an alternative view, one can look at this simulation as a "constraint minimisation problem" where we minimise the internal energy E subject to a constant pressure. The quantity to minimise is hence $E - \lambda P$ where λ is the Lagrange multiplier. This turns out to be the volume V of the system. For easier reference, we borrow vocabulary from thermodynamics, such as enthalpy and pressure, even though the system that we simulate is athermal. We will see throughout the thesis that this analogy continues to the observation of thermodynamic effect, such as discontinuous and continuous phase transitions as well as hysteresis, in our athermal system. This justifies the use of this analogy.

The introduced pressure P in the expression for the enthalpy can be interpreted as a parameter that sets the scale for the volume fluctuations. A larger pressure leads to smaller volume, while structures with a lower pressure have larger volumes. Since the volume can only be changed during the minimisation by the length of the cylinder (thus only in one direction) the pressure is a uniaxial pressure. This implementation of the pressure is therefore equivalent to a pressure caused by two pistons that exert forces on two ends of the unit cell. It is a uniaxial strain condition.

Two different types of minimisation routines are used to minimise the enthalpy $H(\{\boldsymbol{r}_i\}, \alpha, L)$. For the phase diagram, we are interested in the global enthalpy minimum, which is also the densest packing. For the stability analysis of a given structure and investigation of structural transitions we only search for the nearest local minimum to an initial structure.

The BFGS method (named after Broyden, Fletcher, Goldfarb, Shanno [83]) is used to search for the nearest *local* minimum of enthalpy. It is a quasi-Newton algorithm that iteratively finds the nearest minimum from an initial

guess until the absolute value of the gradient falls below a tolerance threshold.

The Basin-hopping algorithm [85] performs a general search for the *global* minimum. It is a stochastic, global minimisation algorithm that iteratively minimises the enthalpy. The iteration consists of a cycle of three steps: random perturbation of the coordinates, local minimisation, and acceptance or rejection of the new coordinates. For the acceptance step the Metropolis criterion was used and for the local minimisation the previously mentioned BFGS method.

These two algorithms, together with a variety of minimisation algorithms, are introduced in chapter 2.5. The BFGS and Basin-hopping algorithms are explained in detail in the Appendix A.2.

Enthalpy and pressure have to be rescaled to obtain non-dimensional quantities. We use the dimensionless enthalpy $h = H/(kd^2)$ and dimensionless pressure $p = P/(k/d)$, where k is the spring constant and d is the sphere diameter.

Since increasing the spring constant is equivalent to lowering pressure, we make contact with the hard sphere limit for $p \to 0$ [14] (see also chapter 2.2.1). By comparing with previous results obtained in this limit, it allows us to verify our simulation results for soft spheres.

Alternative, the simulation model could have also been set up by simply minimising the internal energy of the system at fixed volume (and therefore fixed length L). We then however have three control parameters in the simulation: the diameter ratio D/d, the fixed length L, and the softness k of the spheres. This simulation describes a different experimental scenario that would result in a more complicated three dimensional phase diagram. We therefore chose the approach of minimising enthalpy.

3.2 Simulation and observation of line-slip arrangements in soft sphere packings

With the simulation method above, one can now generate structures for different diameter ratios D/d of tube diameter D to sphere diameter d, and pressures p. By systematically generating structures at given D/d and p, we map out a phase diagram of all stable structures without internal spheres. Diameter ratio and pressure are then the two axes of this phase diagram, displaying under what conditions which structure has the lowest enthalpy. Thus, it is revealing information about the conditions where structures are stable.

The structures in this phase diagram can be classified into two main types, *uniform* and *line-slip* packings. Both types of structures are explained in detail in chapter 2.3.

3.2.1 Phase diagram of all uniform and line-slip structures without internal spheres

Fig 3.2 presents the rich phase diagram for all *uniform* and *line-slip* arrangements in the range $1.5 \leq D/d \lesssim 2.7$. The lower limit is set arbitrarily. Below this limit only the trivial bamboo structure of spheres stacked in a line on top of each other occurs at $D/d = 1$. The upper limit marks the point at which the character of the optimal structures changes radically; beyond this point the structures contain internal spheres which are not in contact with the cylindrical wall [14].

The pressure range is limited to $p \leq 0.02$, beyond which line-slip structures are absent. At large pressures the model of soft spheres may be regarded as unrealistic since the contact area is no longer much smaller than the sphere diameter. For a system of bubbles, which was the initial context for this work,

one encounters the "dry limit", as p increases. At this point all liquid in a foam has been removed, as explained in detail in chapter 1.4.2.

The phase diagram is obtained by minimising the enthalpy for a given diameter ratio D/d and pressure p for several numbers of spheres N in the unit cell. The structure with the lowest enthalpy is chosen. For low pressures the minimisation was performed with the Basin-hopping algorithm. We found that the results from these simulations could be used as initial guesses for the BFGS method to map out the higher pressure regions of the phase diagram. The initial guess is the starting point for the minimisation routine, from where to minimise the enthalpy. Starting with an initial structure (with $N = 3, 4, 5$) we steadily increased the pressure p and diameter ratio D/d independently. As a further check we also ran the procedure in the orthogonal direction - i.e. we start with a seed structure of a high value of D/d, keep the pressure constant while reducing D/d in discrete steps and minimise the enthalpy at each step. In either case the structure with the lowest enthalpy for a given value of D/d and p is given in the phase diagram.

Above the diameter ratio of 2.0, we find 24 distinct phases. These correspond to 10 uniform packings and the remaining 14 structures are their corresponding line slips. Below $D/d = 2.0$ we observe the bamboo structure, the zigzag, the $(2, 1, 1)$ uniform, and the twisted zigzag structure [i.e. the $(2, \mathbf{1}, 1)$ line slip] (for more information, see [14]).

3.2.2 Transitions in the phase diagram

The transitions between different structures in the phase diagram can be classified as follows: In *continuous* phase transitions (marked with dashed lines in Fig 3.2) a structure transforms smoothly into another by gaining or losing a contact. This can be observed in the supplemental video S0 of Ref [3], which shows an overview over all structures at a low pressure, together with the corresponding rolled-out contact network and the structure's position in the

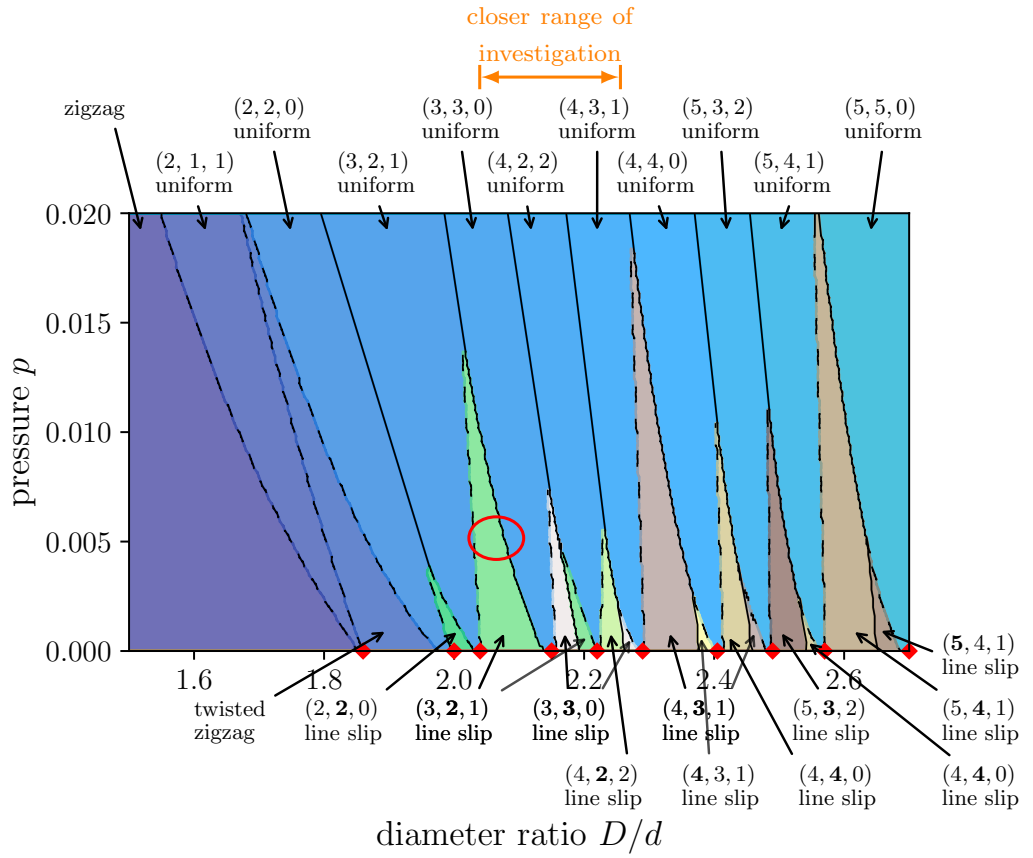

Fig 3.2: Phase diagram for soft sphere packings in cylinders in the range $1.5 \leq D/d \lesssim 2.7$ and dimensionless pressures $p \leq 0.02$. The resolution in the ratio of tube to sphere diameter is $\Delta D/d = 0.0025$ and in the pressure is $\Delta p = 0.0004$. Besides the zigzag, the $(2, 1, 1)$ uniform, and the twisted zigzag structure, there are 10 uniform (blue shaded) and 14 related line-slip structures (green and brown). Small regions that contain the $(\mathbf{2}, 1, 1)$ and the $(\mathbf{3}, 2, 1)$ line slips, which were found for hard spheres, are not visible in this phase diagram due to the finite resolution. Discontinuous transitions are indicated by solid black lines, while continuous transitions are indicated by black dashed lines. The diamond symbols at $p = 0$ correspond to the hard sphere uniform close-packed structures [14]. The orange arrow above the diagram indicates the closer investigation range for different transitions types (see next section 3.2.2). A rough estimate of an experimentally observed line-slip structure (see section 3.2.3) is indicated by the ellipse on this phase diagram, accounting for the possible metastability.

phase diagram. This type of transition is found between a uniform structure and a line slip, e.g. $(3, 2, 1)$ uniform $\Rightarrow$ $(3, \mathbf{2}, 1)$ line slip. The zigzag to $(2, 1, 1)$ transition is also continuous. *Discontinuous* transitions (solid lines in Fig 3.2) are transitions where a structure of particular phyllotactic notation (l, m, n) changes into a structure of a completely different notation (i, j, k), e.g. $(3, \mathbf{2}, 1)$ line slip $\Rightarrow$ $(3, 3, 0)$ uniform. The transition may also be described as abrupt (see also the video S0 of Ref [3]).

A typical example of a discontinuous transition is given by the solid line separating the $(3, \mathbf{3}, 0)$ and $(3, \mathbf{2}, 1)$ line-slip regions. We find in the case of soft spheres that, with increasing pressure, the $(3, \mathbf{2}, 1)$ line slip is the first to disappear at a triple point followed by the $(3, \mathbf{3}, 0)$ line slip at a slightly higher pressure. At still higher pressures only the $(3, 3, 0)$ and $(4, 2, 2)$ uniform structures remain stable, separated by a discontinuous phase transition.

On first glance on our phase diagram, the case $(3, 2, 1) \rightarrow (3, 3, 0)$ seems to be exceptional, in that only a single line slip, the $(3, \mathbf{2}, 1)$ line slip, is visible. From Table A.1 of Appendix A.1 (taken from Ref [14]) we would also have expected to see two line slips separating the uniform structures (as in the other cases). However, the line-slip structure of the $(\mathbf{3}, 2, 1)$ exists only in the narrow range $2.1413 \leq D/d \leq 2.1545$ for the hard spheres and is not resolved in Fig 3.2.

The distinction between continuous and discontinuous transitions can be illustrated directly via the enthalpy h. To do this, we will focus on a more narrow range in D/d. This range is marked by the orange arrow above the phase diagram of Fig 3.2.

Fig 3.3(a) gives an example of h in terms of D/d at constant pressure $p = 0.01$. Continuous transitions, such as $(3, 2, 1)$ uniform (indicated in green) to $(3, \mathbf{2}, 1)$ line slip (indicated in light green), are not apparent in the variation of h. However, discontinuous transitions such as the $(3, \mathbf{2}, 1)$ line slip to $(3, 3, 0)$ uniform (yellow) show a change in the slope of h at the transition.

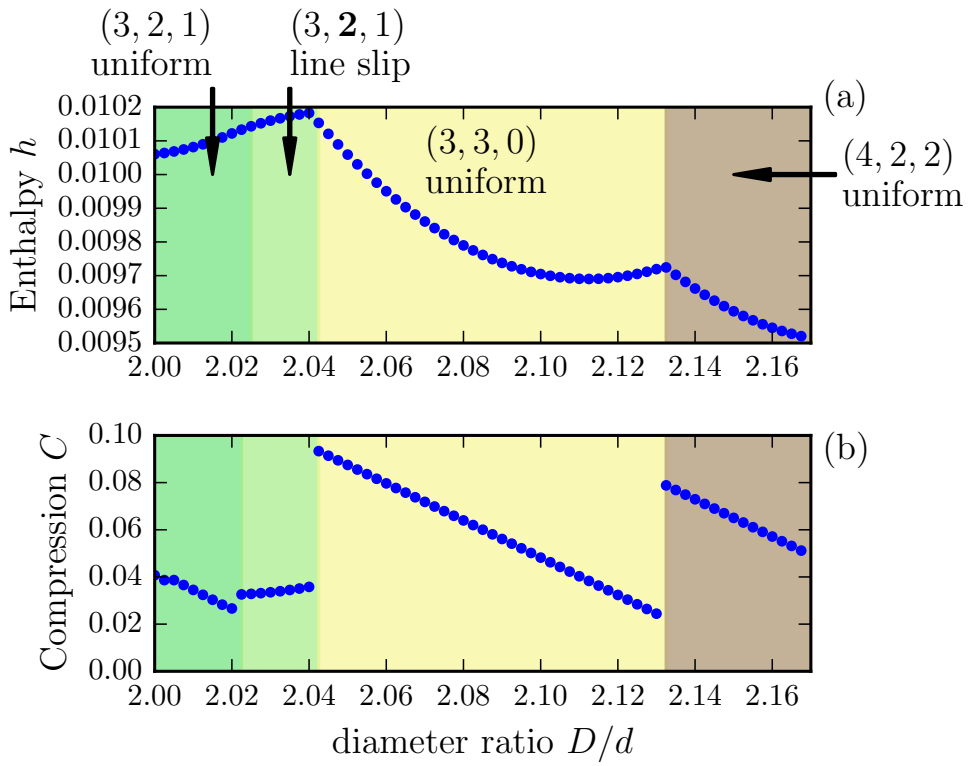

Fig 3.3: Top (a): An example of the dimensionless enthalpy h as D/d is varied at a constant pressure $p = 0.01$. The plot corresponds to a horizontal cut through the phase diagram in the range indicated by the orange arrows above of Fig 3.2. Bottom (b): Compression C of the soft packings as a function of the diameter ratio D/d. Only the transition from $(3, 2, 1)$ to $(3, \mathbf{2}, 1)$ is continuous and does not involve a change in the slope of h at the phase boundary.

Also shown for comparison in Fig 3.3(b) is the compression of the packing subject to the applied pressure. We define the compression as $C = (V_0 - V(p, D/d))/V_0$, where $V(p, D/d)$ is the volume of the unit cell of the soft sphere packing (for the chosen p and D/d) and V_0 is the volume of the unit cell for the corresponding hard sphere structure. In the case of uniform structures the volume of the unit cell in the hard sphere case has a unique value [72]. However, for the line-slip structures this is not the case (since the length of the unit cell depends on D/d) and instead we compare against the smallest volume

of the unit cell for a given hard sphere arrangement of this type [72]. It is similar to the thermodynamic definition of compressibility as $C_{\text{themo}} = -\frac{1}{V}\frac{\partial V}{\partial p}$ in the sense that both are calculated by the variation of volume.

It is illustrative to also consider the orthogonal trajectory, i.e. variation in the enthalpy h in terms of p at constant diameter ratio. As an example of this we show in Fig 3.4 a vertical cut through Fig 3.2, where we hold the diameter ratio at a constant $D/d = 2.1$ and vary the pressure. In Fig 3.4(a) the enthalpy h is given at $D/d = 2.1$ for varying pressure and the corresponding compression ratio is shown in (c). The trajectory passes through a transition from $(3, \mathbf{2}, 1)$ to $(3, 3, 0)$ and then from $(3, 3, 0)$ to $(4, 2, 2)$ - both of these are discontinuous transitions; while the change in the slope cannot be determined by inspection from Fig 3.4(a), it nevertheless can be clearly observed by taking the derivative of h with respect to p along the trajectory (see Fig 3.4(b)). Note the similarities between the derivative in enthalpy (b) and the compression (c): One seems to be the negative of the other, which allows us to classify the transition as continuous vs discontinuous in analogy to the thermodynamic concept of first and second order transitions.

3.2.3 Experimental observation of a line slip

In the previous section we showed that line-slip structures do not only assemble for hard spheres, but also soft spheres. Especially, Fig 3.2 indicates the existence of these kind of structures up to a certain pressure (or overlap). But so far line-slip structures in soft systems were only found in computer simulations.

These simulations lead to the prediction of such structures in experimental realisations of systems with soft (deformable) spheres. Here we verify that such a structure can also be realised in experiments with soap bubbles inside a glass tube. We present an experimental observation of a column of bubbles, clearly exhibiting such a line-slip arrangement (see Fig 3.5). By comparing the

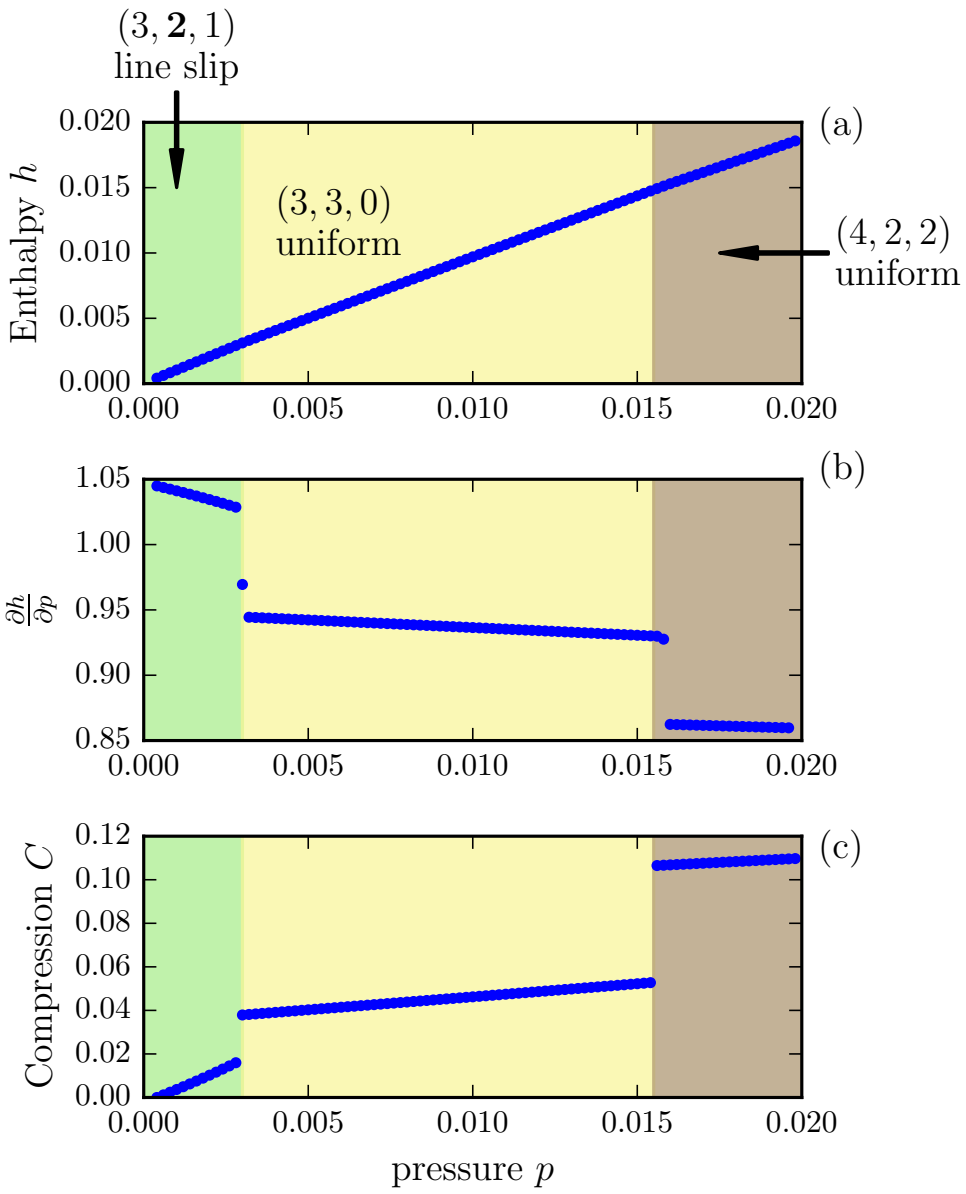

Fig 3.4: An example of the dimensionless enthalpy h as p is varied at a constant $D/d = 2.1$ (a) and its numerically computed derivative with respect to p in (b). Both plots show a vertical cut through the phase diagram of Fig 3.2. The transitions shown are all discontinuous. However, for the enthalpy the change in the slope at the phase boundaries can only be detected in the derivative $\partial h/\partial p$ of plot (b). Plot (c) displays the compression C of the soft packings as a function of the applied pressure.

capillary pressure of a bubble with its hydrostatic pressure, it can be shown that bubbles packed inside a tube, can be perceived as such soft spheres. Thus, these experiments verify the existence of line slips in systems of soft particles.

First, we describe our experimental procedure and results. All experiments, described here, have been performed by Dr. Benjamin Haffner, a former Post-doc in the Foams and Complex Systems Group. While he created the foam structures, I identified and analysed them, since I have the expertise in categorising and labelling the columnar structures.

We choose to observe structures of columns of bubbles under *forced drainage*; that is, a steady input of liquid from above [33, 88, 89] (as explained in detail in chapter 1.4.2). In the past, this has been extensively studied for columns of bulk foam where D/d much larger than the range we study here. It was found that this results in convective instabilities for flow rates that gave rise to higher liquid fractions, confining experiments on static foam structures to relatively dry foam [34].

The present work leads us to consider columns of wet foams, that is, with the drainage rate high enough to produce near-spherical bubbles. We find no such instability in the case of the confined columnar structures of large bubbles considered here; hence the wet limit can be reached at a certain flow rate. Below that point, the liquid fraction can be controlled by the flow rate, producing ordered columnar structures closely analogous to those described by our simulations.

We use the same experimental set-up as explained in the Introduction 1.4.2: monodisperse bubbles are produced by blowing air through a needle into a solution of commercial surfactant, Fairy Liquid [32, 88]. The surfactant solution contains 50 % by weight of glycerol in order to increase the viscosity, smooth the transition between structures and to allow us to observe more easily unstable bubble arrangements. Tuning the gas flow rate ($q_0 \sim 1\,\mathrm{mL/min}$) allows us to produce monodisperse bubbles of controlled size.

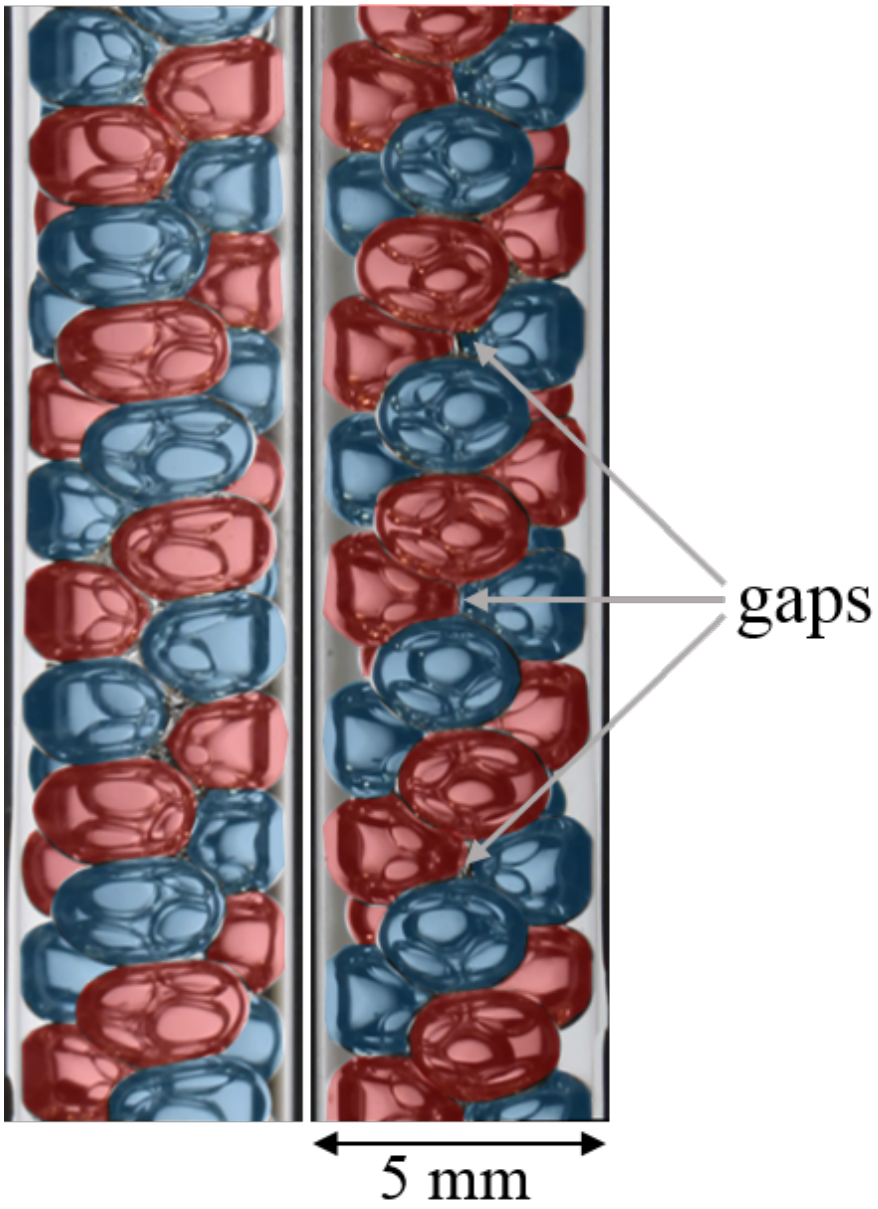

Fig 3.5: Photograph of columnar structures of bubbles under forced drainage, showing about forty bubbles. **Left:** $(3, 2, 1)$ uniform structure occurring at a relatively low flow rate. **Right:** Bubbles adopt the $(3, \mathbf{2}, 1)$ line-slip structure at a relatively high flow rate. It is similar to the line-slip structure of Fig 2.4(b). The post-processed colouring highlights the two interlocked spirals of the $(3, 2, 1)$ and $(3, \mathbf{2}, 1)$ structures. The estimated position of the line slip on the phase diagram of Fig 3.2 is marked by the red ellipse in Fig 3.2.

The bubbles are approximately of size $d \sim (2.50 \pm 0.04)\,\mathrm{mm}$. The diameter d can be determined by squeezing a small amount of foam between two horizontal, parallel plates, separated by a negligibly small gap to obtain a monolayer of bubbles. The bubble area A of the bubbles in the monolayer can be determined from analysing images from above. The diameter is then calculated as $d = \sqrt{2A/\pi}$.

When released into a vertical cylinder, the bubbles are observed to self-organise into ordered columnar structures (we used a glass tube of inner diameter 5 mm and length 1.5 m). The resulting foam column is put under forced drainage by feeding it with surfactant solution from the top (liquid flow rate Q up to $\sim 10\,\mathrm{mL/min}$). For a bubble in our experiments the capillary pressure is $p_\mathrm{c} = \gamma/r$, where $\gamma = 0.03\,\mathrm{N/m}$ is the surface tension and $r = d/2$ is the radius of the bubble. Thus, we estimate the capillary pressure for the bubbles to be of the order of approximately $p_\mathrm{c} \sim 10\,\mathrm{Pa}$. The hydrostatic pressure, $p_\mathrm{h} = \rho g x$, for a given bubble depends on its height x of the bubble in the column, as measured from the liquid/air interface at the top, as well as the density of water ρ and gravity g. With a column height of approximately 1 m, the hydrostatic pressure is three orders of magnitude larger ($p_h \sim 1 \times 10^4\,\mathrm{Pa}$) than the capillary pressure and dominates in the experiments. Thus, the bubbles are in the regime where they can easily be deformed and the foam can safely be regarded as a packing of relatively *soft* objects.

Fig 3.5 shows an example of the observation of the $(3, \mathbf{2}, 1)$ line-slip structure in accord with expectations based on the soft sphere model, described in previous section. Note that the bubbles are distorted into smooth ellipsoids by the flow. The extent of the loss of contact in the observed line-slip structure is roughly equal to that of the simulated structure at the position marked with a red ellipse in the phase diagram of Fig 3.2. This is also consistent with an estimation of equivalent pressure p and D/d, where the pressure is determined from the local packing fraction.

In the depicted region of Fig 3.5 the difference in pressure from top to bottom is negligible small, so that the pressure gradient is not important for this experiment. By extending the height of the investigated structures to the full length of the tube, the experiment can easily be altered to include a pressure gradient. The assembled structures will then include structure transitions with the height. We discuss possible experiments of this type in the conclusions at the end.

However, while the boundaries plotted in Fig 3.2 demarcate the borders between the lowest enthalpy structures, these structures can be metastable in experiments. The experimentally observed line slip can therefore exist in a larger range than marked by the ellipse in Fig 3.2. Thus, a closer investigation of metastability and hysteresis of our simulated packings is needed.

3.3 Hysteresis and metastability in structural transitions

For microscopic systems, our results from the phase diagram (Fig 3.2) are strictly only relevant to structures in equilibrium. For some systems, such as those currently under investigation [16, 44, 64, 90–92], many observed structures are metastable (i.e. not structures of lowest enthalpy). Pittet *et al.* also discovered that a structural transition between columnar structures of soap bubbles does not necessarily return to the original structures, when the control parameter is reverted [28, 38]. Thus, columnar structure can be metastable and their structural transitions are in general hysteretic.

We therefore engaged in exploring the wider context of metastable structures and structural transitions between them by performing further simulations. This establishes a full comparison with possible future experiments. It includes possible transformations between structures as well as their regions of

(meta)stability, which are both vital information for experimental realisation of such structures.

Where previously the computation of a phase diagram entailed a search for the *global* minimum, involving the Basin-hopping algorithm that allowed radical changes of structure to be explored, here we pursue a more limited objective. *Given a stable structure, possibly metastable, how does it change when diameter ratio D/d (and/or the pressure p) are continuously varied, if it is to remain in the local minimum of enthalpy?* Since we are interested here in the local minimum of enthalpy, we employ the BFGS method. To ensure that the nature of hysteresis investigated in this section is independent of the minimisation method, we corroborated a subset of results with the gradient descent routine (for both methods see also chapter 2.5.1).

Due to the local minimisation, structures of high symmetry, such as the $(4, 2, 2)$, can get stuck on a saddle point, where the enthalpy is not minimal, but its gradient is zero. This can be avoided by applying a *small* random perturbation to the structure, which displaces it from the saddle point, followed by a local minimisation. This random perturbation in the sphere positions does not exceed 10 % of the sphere diameter.

All simulations were carried out for a unit cell with $N = 12$ spheres. This choice is commensurable with structures that require a minimum of $N = 1, 2, 3$ or 4 spheres in the unit cell. All known structures from the previously identified hard-sphere packings within the considered range of D/d can be simulated with these required numbers of spheres (see Table A.1 in the Appendix A.1 for structures and the number of spheres in the unit cell). An exception to this are packings which contain $N = 5$ spheres; however, in the hard sphere case, these occur only for high values of D/d and as such are out of the range of the present simulations.

Initially, in this section, we compute trajectories in the $(p, D/d)$ plane by locally minimising the enthalpy and record the boundaries where the structure

changes to one of a different character. With a sufficient number of trajectories, a *stability diagram* is built up, i.e. a map of the location of structural transitions.

We investigate the structural transitions between the $(3, 2, 1)$ and $(4, 2, 2)$ uniform structures and the associated $(3, \mathbf{2}, 1)$ line slip as an example of a reversible transition in closer detail. Reversible transitions revert back into the initial structure (e.g. the $(3, 2, 1)$ in our example) when the control parameter is reversed. They are nonetheless accompanied by hysteresis as we will see.

We begin by plotting the changes in enthalpy that occur for a structure when p is held fixed and D/d is steadily varied. We show that, at low pressure, it is possible to start with any one of these structures and continuously transform one structure into another: that is, a change in D/d can transform a uniform structure into a line-slip arrangement by the loss of a contact and a line slip into a uniform structure by the formation of a contact. This is accompanied by a smooth variation in the enthalpy, or at most a change in the slope of the derivative of the enthalpy when a new contact is formed. However, at higher pressure, some of these transitions are no longer reversible and show evidence of hysteresis. Such discontinuous transformations are accompanied by a discontinuity in the enthalpy. From such results we eventually obtain a stability diagram, from which we can extract a schematic stability diagram.

In the later part of this section, we use this simulation procedure to construct a directed network between all uniform structures from the phase diagram of Fig 3.2. It displays *all* permissible structural transitions between uniform structures without internal spheres and summarises all possible types of structural transitions. These are not necessarily of reversible nature (as the example of the $(3, 2, 1) \Leftrightarrow (4, 2, 2)$ transition). From this network graph we identified counterclockwise cyclic patterns of which we investigate one cycle with enthalpy curves in closer detail.

3.3.1 Enthalpy curves at constant pressures for a reversible transition

An example of a computed enthalpy curve is shown in Fig 3.6. It shows the change in enthalpy as D/d is increased and pressure is held constant at $p = 0.007$. At such a low pressure a change in D/d allows the $(3, 2, 1)$ uniform structure to transition continuously into the $(3, \mathbf{2}, 1)$ line-slip arrangement (by the loss of contacts), and then continuously into the $(4, 2, 2)$ uniform structure (by the formation of new contacts), both reversibly. The values of D/d where the changes in the structure occur are indicated by dashed vertical lines in Fig 3.6. The smooth change in the enthalpy over the course of these transitions demonstrates that the process is continuous and reversible. The smooth change in structure, together with its rolled-out contact network and its position in the stability diagram, Fig 3.9(b), can also be observed in the supplemental video S1 of Ref [3].

Note that these transitions cannot be obtained from the information of the phase diagram (Fig 3.2), which is based on the global minimum of enthalpy. It would predict the occurrence of the $(3, 3, 0)$ uniform structure which, however, does not occur in Fig 3.6.

At the higher pressure of $p = 0.02$ the nature of the transitions between these structures is different, as illustrated in Fig 3.7. As before, and shown by the blue crosses, starting with the $(3, 2, 1)$ uniform structure, a steady increase in D/d leads to a smooth change in the enthalpy leading to the $(3, \mathbf{2}, 1)$ line slip at a value of D/d, as indicated by the vertical blue dashed line. However increasing D/d further leads eventually to a discontinuous transition whereby the structure transforms suddenly into the $(4, 2, 2)$ uniform arrangement, as indicated by the continuous vertical blue line. At this point in D/d the enthalpy shows a sudden drop. The supplemental video S2 of Ref [3] illustrates this sudden transformation into the $(4, 2, 2)$ uniform arrangement.

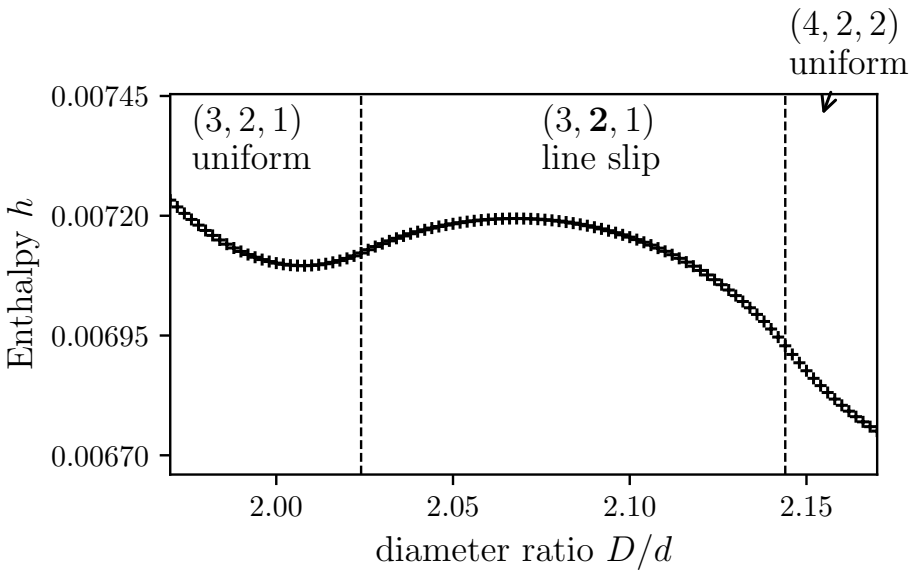

Fig 3.6: Variation in enthalpy h as a function of D/d for pressure $p = 0.007$. The change in D/d allows the packing to continuously (and reversibly) transform between the $(3, 2, 1)$ structure, the $(3, \mathbf{2}, 1)$ line-slip, and the $(4, 2, 2)$ uniform structure. The values of D/d at which the structure changes are indicated by the dashed vertical lines.

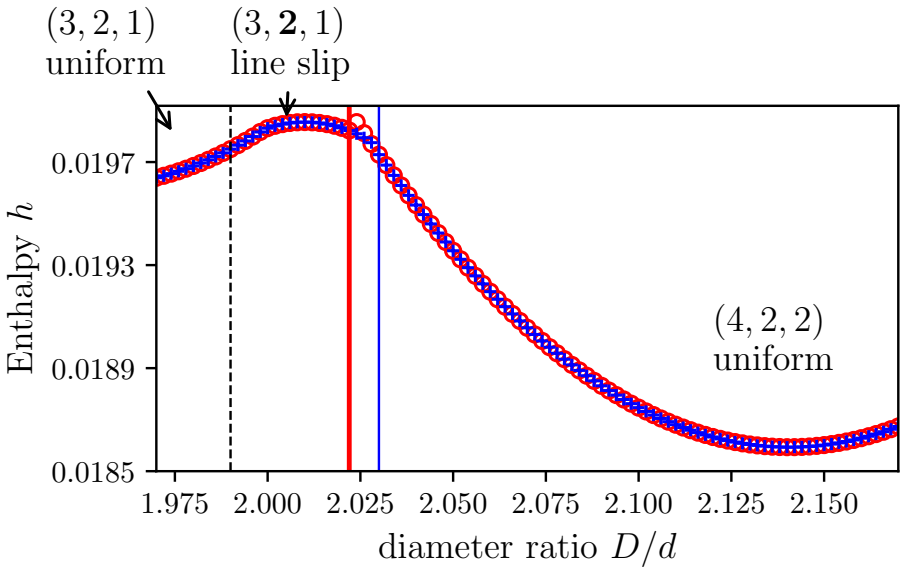

Fig 3.7: Variation in enthalpy h as a function of D/d for pressure $p = 0.020$. Changing D/d leads to a reversible and continuous transformation between the $(3, 2, 1)$ uniform structure and the $(3, \mathbf{2}, 1)$ line slip for both the forward (increasing D/d, blue crosses) and reverse (red circles) trajectories, indicated by the vertical dashed line. In contrast, the transition from the $(3, \mathbf{2}, 1)$ line-slip structure to $(4, 2, 2)$ uniform arrangement (thin blue line) is discontinuous and occurs at a lower value of D/d on the reverse trajectory (thick red line).

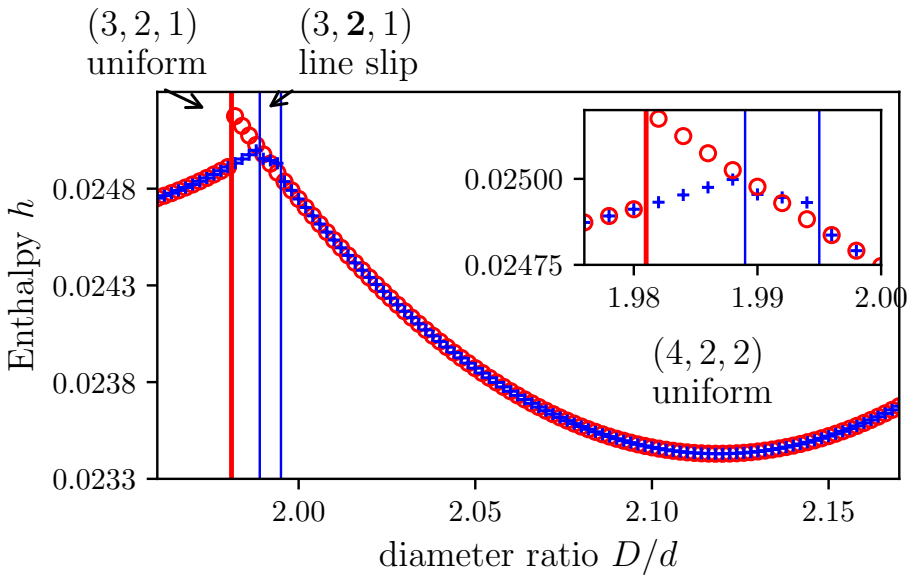

Fig 3.8: Variation in enthalpy h as a function of D/d while holding pressure at a constant value of $p = 0.026$. The forward trajectory is as before: an increase in D/d leads to a discontinuous transformation from the $(3, 2, 1)$ uniform structure to the $(3, \mathbf{2}, 1)$ line slip (thin blue line), a further increase in D/d results in a discontinuous transition to the $(4, 2, 2)$ uniform structure (thin blue line). The reverse trajectory is remarkable in that the intervening line slip is eliminated. Instead the transition from the $(4, 2, 2)$ uniform to the $(3, 2, 1)$ uniform structure is via a discontinuous transition (thick red line). The inset shows a zoom on the discontinuous transitions.

When the diameter ratio is decreased again (red circles), the transition from the $(4, 2, 2)$ uniform structure to the $(3, \mathbf{2}, 1)$ line slip is again discontinuous (thick red vertical line). However, the transition to the $(3, \mathbf{2}, 1)$ line-slip structure occurs at a *lower* value of D/d on the reverse trajectory as compared to the forward trajectory and thus exemplifies the structural hysteresis present in these packings above a critical pressure.

At even greater pressures the line-slip structure disappears completely from the reverse trajectory, as shown in Fig 3.8 for $p = 0.026$. Now, in the forward trajectory a discontinuous transition (vertical thin blue line) transforms the $(3, 2, 1)$ uniform packing into the $(3, \mathbf{2}, 1)$ line slip and then

to the $(4, 2, 2)$ uniform structure by a further discontinuous transition. On the reverse trajectory the $(4, 2, 2)$ uniform structure jumps straight to the $(3, 2, 1)$ uniform structure by a discontinuous transition (vertical thick red line) - without the presence of the intervening line slip. Increasing the pressure yet higher ($p \lesssim 0.028$) eliminates the line slip also on the forward trajectory so that transformations between the $(3, 2, 1)$ uniform structure and the $(4, 2, 2)$ uniform structure are accompanied only by discontinuous transitions, and the line slips are completely eliminated. Further supplemental videos S3–S4 of Ref [3], display the structures and rolled-out contact networks along these trajectories.

3.3.2 Stability diagram for a reversible transition

The stability diagram represents the boundaries at which transitions take place between a particular set of structures (starting with one of the structures listed in it). Other metastable structures must exist in the same region, but are not represented. As mentioned earlier, the stability diagram is not to be confused with the phase diagram in Fig 3.2.

Fig 3.9(a) is the stability diagram representing transitions between the $(3, 2, 1)$ and $(4, 2, 2)$ uniform structures and the associated line slip $(3, \mathbf{2}, 1)$. It was obtained from the calculations of enthalpy curves of the kind described in the previous subsection 3.3.1. Fig 3.9(b) is a schematic guide to the interpretation of this stability diagram, which is correct in representing the topological features of the stability diagram but does not preserve the geometrical features. Here U_1 is to be identified with the $(3, 2, 1)$ uniform packing, U_2 is to be identified with the $(4, 2, 2)$ uniform packing and LS with the $(3, \mathbf{2}, 1)$ line slip.

Continuous transitions (reversible) between structures are marked by dashed lines while discontinuous transitions (irreversible) are represented by solid lines. Blue arrows indicate the directions for which such boundaries entail

a transition. We also mark the nature of the boundary and the structures encountered on either side of the boundary.

The reversible boundaries are to be identified with parts of the phase boundaries of the equilibrium phase diagram, Fig 3.2.

As displayed in Fig 3.9, there are four qualitatively different pressure regimes, corresponding to the examples described above. These are $p < p_3$ (see Fig 3.6), $p_3 < p < p_2$ (see Fig 3.7), $p_2 < p < p_1$ (see Fig 3.8) and $p_1 < p$. For the last regime, i.e. above p_1, the metastable phase of the $(3, \mathbf{2}, 1)$ line slip has completely vanished. Here the enthalpy curves show discontinuities at the blue crosses for increasing D/d and at the red circles for decreasing D/d. Videos S1–S4 of the supplemental videos from Ref [3] illustrate the change in structure for all four different pressure regimes when varying D/d at constant pressure. At the discontinuous transitions the corresponding videos reveal the sudden change in structure.

To illustrate the useful application of the schematic diagram Fig 3.9(b) we describe the case $p_3 < p < p_2$ in detail by choosing $p = 0.020$, which corresponds to the enthalpy curves shown in Fig 3.7. The other cases can be interpreted similarly by comparing Fig 3.9(a) with Fig 3.9(b).

Starting from the $(3, 2, 1)$ uniform packing at $p = 0.020$ increasing D/d leads to a boundary [shown by the blue crosses in Fig 3.9(a)] which marks the continuous transition to the $(3, \mathbf{2}, 1)$ line slip. In Fig 3.9(b) this is marked by the dashed line indicating the continuous transition $U_1 \leftrightarrow$ LS.

Increasing D/d further a second boundary (blue crosses) is encountered, making a discontinuous transition to the $(4, 2, 2)$ uniform structure. This boundary is shown in the schematic diagram by the solid line and is labeled LS $\rightarrow U_2$. The arrow indicates that this is encountered only upon increasing D/d, transforming the line slip LS into the uniform structure U_2 by a discontinuous transition.

Upon decreasing D/d the $(4, 2, 2)$ uniform structure undergoes a discon-

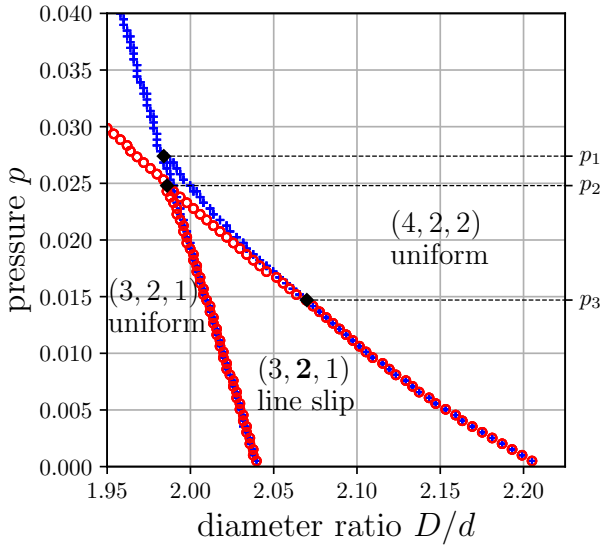

(a)

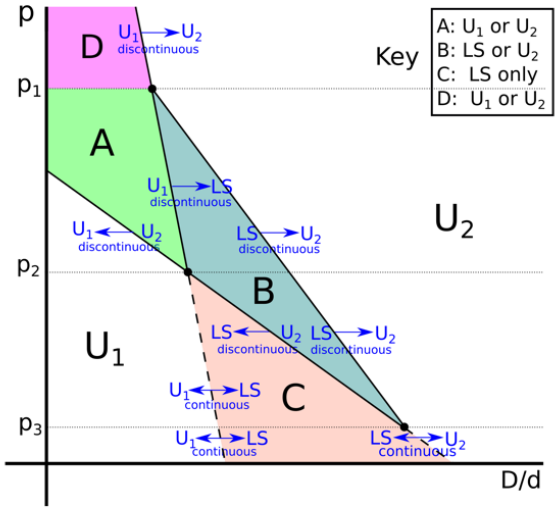

(b)

Fig 3.9: (a) The stability diagram for transitions between $(3,2,1)$, $(4,2,2)$ and the associated line slip $(3,\mathbf{2},1)$. The computed transition points are indicated by blue crosses (increasing D/d) and red circles (decreasing D/d) according to the direction taken. This is indicated by arrows in the accompanying schematic diagram, (b). Here the two uniform arrangements are labeled U_1 and U_2 and the intermediate line-slip arrangement is labeled LS. The key at the top right indicate the structures occupied by the different regions A, B, C, and D. This diagram represents the topology of (a), but does not preserve geometrical features. Continuous transitions are marked by dashed lines, and discontinuous transitions are represented by solid lines.

tinuous transition at the boundary indicated by red dots in Fig 3.9(a) into the $(3, \mathbf{2}, 1)$ line slip. This boundary is marked by the solid line in the schematic diagram accompanied by the label LS $\leftarrow U_2$.

A further decrease of D/d results in a continuous transition into the uniform $(3, 2, 1)$ structure, at the boundary marked by red dots in Fig 3.9(a) and dashed line in Fig 3.9(b). We have thus returned to the starting point of this particular excursion through the stability diagram.

3.3.3 Directed network of structural transitions

The previous stability diagram (Fig 3.2) gives us detailed information about the stability regions of reversible transitions, i.e. transitions where U_1 transformed into U_2 upon increasing D/d ($U_1 \rightarrow U_2$) and U_2 transitioned back into U_1 upon decreasing D/d ($U_1 \leftarrow U_2$). However, there are many more transitions of different types. The directed network of Fig 3.10 summarises all structural transitions between the uniform structures given in the phase diagram of Fig 3.2.

We obtained the main information for this network by investigating the following question with the previously described soft sphere simulations in the limit of hard spheres: *Starting with a given uniform structure, which of these transitions is favoured under continuous variation of the diameter ratio D/d?* For any given uniform structure, there are potentially multiple intermediate line-slip arrangements, each leading to a different uniform structure. In our simulations we do not observe all of these transitions, only a subset, which we call *favourable* transitions. With additional information from the previous hard sphere results about the remaining unfavourable transitions (see Fig A.1 and A.2 in Appendix A.1), we can complete the directed network.

We introduced a conceptual origin $(0, 0, 0)$: The closer a structure is to this origin, the smaller is its D/d. The dashed lines represent contours of constant D/d about the origin (i.e. $D/d = 0$); thus a transition from one

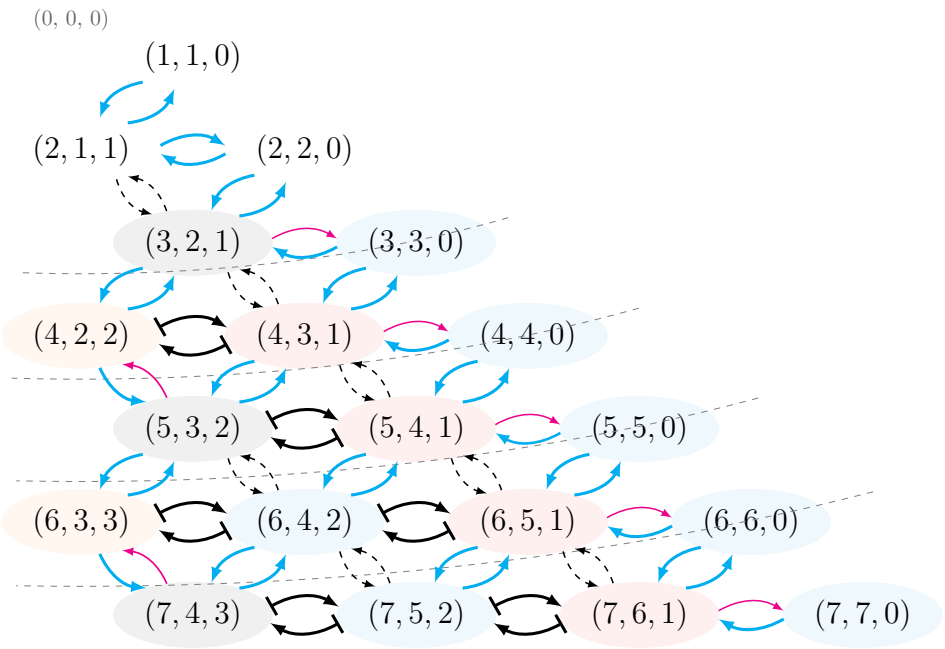

Fig 3.10: Directed network displaying possible structural transitions between all uniform structures from the phase diagram of 3.2. The point $(0, 0, 0)$ represents a conceptual origin for the diagram corresponding to $D/d = 0$, dashed lines are contours of constant D/d. A transition from one structure to another which involves moving along the diagram in a direction perpendicular to the contours implies a change in D/d. We indicate favourable transitions with bold blue arrows, unfavourable transitions with red arrows and all re-entrance cases are indicated by bold black lines (see text for explanation of favourable transition). In all other metastable cases transitions follow the double dashed black arrows. Uniform structures of same adjacent transition types are coloured in same colours. Starting from the $(3, 2, 1)$ structure we found that the favourable paths follow a counterclockwise cyclic pattern going along the diagonals from the top right to bottom left.

uniform structure to another which requires moving along the diagram in the direction perpendicular to the contours implies a change in D/d.

All favourable transitions are displayed by bold blue arrows in Fig 3.10. Cyclical blue arrow pairs thus indicate reversible transitions such as the previously described transition from $(3, 2, 1) \Leftrightarrow (4, 2, 2)$. Red arrows indicate transitions that are not reversible. For instance, the $(3, 3, 0)$ uniform struc-

ture favours the transition into the $(3, 2, 1)$ structure (when decreasing D/d). However, the reverse transition is not preferred, instead the $(3, 2, 1)$ favours the transition into the $(4, 2, 2)$. The dashed and bold black arrows are transitions identified from previous hard sphere results, as added to this thesis in the Appendix A.1 in Fig A.1 and Fig A.2 [14]. Such transitions cannot be observed in our soft sphere simulations (unless starting from from the metastable intermediate line slip). The bold black lines highlight the special case of the re-entrance case, which will be described in more detail below.

For the purpose of greater clarity, all intermediate line-slip structures were left out of this graph. Each arrow represents the transition from a uniform structure, over a line slip to another uniform structure of different phyllotactic notation. Similar investigations can also be done with softer spheres (or higher pressure p). Since the effect of increasing pressure is the disappearance of line slips, we would expect these intermediate structure to vanish. But the connection between uniform structures as given by Fig 3.10 would remain.

Following the favourable transition in the graph, we can identify cyclic patterns that can only be followed counterclockwise. These are going along the diagonals from the top right to the bottom left with the first cycle starting with the $(3, 2, 1)$ structure: $(3, 2, 1) \Leftrightarrow (4, 2, 2) \Rightarrow (5, 3, 2) \Leftrightarrow (4, 3, 1) \Leftrightarrow (3, 3, 0) \Rightarrow (3, 2, 1)$. The two red arrows at the at the $(3, 2, 1)$ and the $(5, 3, 2)$ prevents this cycle from going clockwise.

Fig 3.11 shows the enthalpy curve h for the first cycle at very low pressure (in the limit of hard spheres). The enthalpy of uniform structures are given in this plot by the minima of the two curves. In-between are the enthalpies of intermediate line slips. Increasing D/d from the $(3, 2, 1)$ uniform structure, the line slip leading to the $(4, 2, 2)$ structure is favoured (blue dots). By further increasing D/d, we finally reach the $(5, 3, 2)$, the return point of the cycle. Decreasing D/d at this point leads us on a different enthalpy curve (yellow triangles) back to the $(3, 2, 1)$ uniform structure.

For experimental purposes, these counterclockwise cycles imply that a $(3, 2, 1)$ to $(3, 3, 0)$ transition can only be achieved by first increasing D/d until a $(5, 3, 2)$ structure is found, followed by decreasing D/d again. A direct transformation from $(3, 2, 1)$ to $(3, 3, 0)$ is not possible, even though they are adjacent structures in the phase diagram of Fig 3.2.

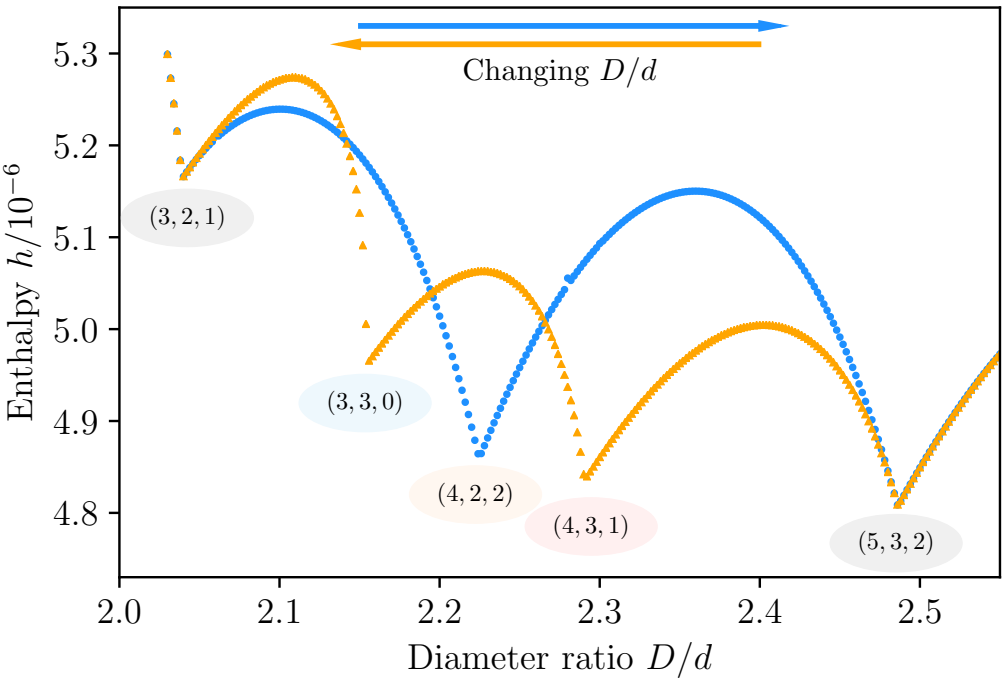

Fig 3.11: Enthalpy h for the first counterclockwise cycle of Fig 3.10 by varying the diameter ratio D/d at constant pressure $p = 5 \times 10^{-6}$. We start the cycle in the local minimum labelled as the $(3, 2, 1)$ structure on the left-hand side. The blue dots indicate the enthalpy of the favoured intermediate line slip upon increasing D/d. This trajectory leads the initial $(3, 2, 1)$ structure over the $(4, 2, 2)$ into the $(5, 3, 2)$ uniform structure. Decreasing D/d from there, a different intermediate line slip is preferred (yellow triangles), leading to a different uniform structure at the minima of the yellow enthalpy curve. However, by decreasing D/d further the $(3, 2, 1)$ is reached again, closing the cycle.

In the directed network of Fig 3.10 we can now distinguish between four different types of transitions: reversible transitions, irreversible transitions, re-entrance cases and metastable cases.

We already discussed the reversible transition in greater detail previously. They occur between structures with two blue arrows, like the example of $(3,2,1)\Leftrightarrow(4,2,2)$, which we investigated previously. When increasing D/d starting from the $(3,2,1)$, the preferred transition (blue arrow) is into $(4,2,2)$; similarly upon decreasing D/d the favoured transition returns the system back to the $(3,2,1)$ structure. Thus, this transition is overall reversible.

However, for some transitions the reversed transformation is unfavored. An example of an irreversible transition is the transition $(4,2,2) \Rightarrow (5,3,2)$. The $(4,2,2)$ follows an intermediate line slip into the $(5,3,2)$, when the diameter ratio is increased. But the $(5,3,2)$ structure *cannot* be transformed back into the $(4,2,2)$ by a decrease in D/d, instead it transforms into the $(4,3,1)$ – which is then a reversible transition again.

The re-entrance cases are indicated by bold black arrows, as in the case of $(4,2,2) \Leftrightarrow (4,3,1)$. Here the line-slip arrangement intermediate between these two uniform structures is metastable. Thus, it is not possible to enter this line slip from one of the adjacent uniform packings.

In the hard sphere limit, this line-slip structure has the special property that it exists at two distinct values of packing fraction at the same diameter ratio D/d (cf. Fig A.2 in Appendix A.1). For instance to the line that connects the $(4,2,2)$ and $(4,3,1)$ in Fig A.2, two distinct values of packing fractions ϕ at a given D/d can be assigned.

This leaves the double thin black arrows as the last possible transition between two uniform structures. This intermediate line slip is also metastable and cannot be reached from any uniform packing with our soft sphere simulations. It distinguishes itself from the other line slips by having the lowest packing fraction (and the highest enthalpy).

A similar, but more sparse directed network graph for hard sphere simulations is shown in Fig 8 of [64] (see also Fig 2.6), where the assembly sequence upon only increasing D/d of such structures was investigated. While our

results are consistent with their findings, Fig 3.10 is vastly extended in information. It gives predictions for all possible transition, including decreasing D/d. Our network graph also depicts very clearly the emerging cyclic pattern, which is not visible in Fig 2.6.

Another related study is that of Pittet *et al.* [37] who observed structural transitions in cylindrical *dry* foam. They observed two distinct sequences of transitions upon increasing D/d and starting from the simple $(1, 1, 0)$ structure of a linear chain of bubbles (also called bamboo structure). Their findings were represented in a similar grid of structural transition [see Fig 3 of Ref [37]] to that of Fig 3.10. It indicated the two sequences of transitions observed in experiments and simulations, respectively. However, their dry foam structures are well outside of the range of our investigation and their transitions therefore are not in accordance with Fig 3.10.

3.4 Conclusions

In conclusion, questioning the relevance of hard-sphere properties to physical systems, consisting of *soft* spheres, has led us into a new territory, not previously explored. We have shown that line-slip arrangements are a feature of soft systems, thus extending their usefulness to encompass a range of commonly encountered substances including foams, emulsions, and colloids. It is of direct relevance to some physical systems (foams and emulsions) and offers qualitative interpretation in others. It extends into another dimension (that of pressure) the elaborate table of hard-sphere structures previously found (cf table A.1 in Appendix A.1).

Our results, especially the phase diagram Fig 3.2, may be fruitfully compared with previous studies employing the Lennard–Jones potential, where both uniform structures and line-slip arrangements are observed [16, 45]. On the other hand, in the case of very soft potentials, such as the Yukawa

interaction, line-slips have neither been predicted to exist [93] nor observed in experiments [16]. Determining the robustness of the phase diagram presented in Fig 3.2 as a function of the hardness/softness of the interaction potential remains an open question.

We did not observe any new structures that are particular for soft sphere systems, i.e. that can be found at higher pressure. All structures from Fig 3.2 are the same as found in previously investigated hard sphere systems. This might be due to our minimisation procedure where we are not running an exhaustive search for the global enthalpy minimum at higher pressures. There might be an enthalpy minimum that is lower than the one we found, but far away from all structures depicted in the phase diagram. It is also possible that they appear at much higher pressure than we investigated. However, at those pressure the soft sphere model becomes unrealistic for comparison with systems of bubbles. At these pressures other models, such as the Z-cone model [94] or the Morse–Witten model [5] (that will be discussed in more detail in the outlook of chapter 6) might be more appropriate.

Using our computer simulations, we also investigated metastability and hysteresis for structural transitions of columnar structures. We have not attempted an exhaustive description of metastability and hysteresis in this system. Instead, a representative example of a reversible transition was examined in detail, resulting in a stability diagram of Fig 3.9. All possible structural transitions between structures of the phase diagram are summarised by the directed network in Fig 3.10. All reversible transitions, displayed in this network, are qualitative similar to Fig 3.9. Thus, Fig. 3.9(b), given the coordinates of about six points, where the lines meet can serve as a guide to any such case. Other types of structural transitions (such as irreversible transitions) are different; all of these are subject to future investigations.

It is perhaps surprising that all structures in the stability diagram resulted only in the appearance of structures that are to be found in the equilibrium

phase diagram, albeit over different ranges of p and D/d. This may be rationalised at or close to the hard sphere limit, but might not have been anticipated at higher pressures. It would appear that the procedure adopted here allowed the appearance of radically new structures, for instance structures with defects and kinks (such as the one displayed in Fig 1.10(c) in chapter 1.4.3). These radically new structures would be metastable structures that do not occur in the phase diagram of Fig 3.2. But none of such structures were found.

It may be interesting to extend this analysis on hysteresis and metastability to higher values of D/d, for which Fu *et al.* [65] have computed a list of equilibrium structures that are of a different character, as we noted in chapter 2.4. This is likely to be quite demanding, and should perhaps be guided by preliminary experimental investigations of that regime.

Our results should also provide insight for new experiments in which it is more convenient to vary p for fixed D/d, rather than the reverse. For example, in experimental system as examined in section 3.2.3 ordered columnar bubble structures already have natural variation of p within the column in this experiment, due to gravity. Such a system may be used to identify structures and transitions between them, for comparison with what is presented here. Diagrams such as Fig 3.9(b) may then serve as a guide to the practical fabrication of structures of soft spheres in tubes, for which the equilibrium phase diagram of Fig 3.2 by itself, may be misleading. These possible future experiments are discussed in more detail in chapter 6.

Chapter 4

Rotational columnar structures of soft spheres

Related publication:

1. J. Winkelmann *et al.* Phys Rev E **99** 020602(R) (2019).

Recently, the subject of columnar structures has been given a new twist by the development of a novel experimental method by Lee *et al.* [8]. In their experiments, the rapid spinning of a liquid-filled column containing spheres of lower density than the surrounding fluid drives the spheres toward the central axis. Confined by a centripetal force, they assemble as columnar structures around this axis.

Lee *et al.* performed lathe experiments on this assembly method by using polymeric beads, which are impenetrable and essentially behave like hard spheres. Depending on the number of spheres and the rotational speed, they observed various types of structures. Their experimental results are corroborated in parts with Molecular Dynamics (MD) simulations.

We adopt here a different approach using analytical methods to calculate the energy of such structures for *soft* spheres. From these we obtain a comprehensive phase diagram, of which the two axes correspond to a variation of the linear number density (number of spheres per unit length), which

can be varied in an experiment, and the rotational frequency. Finally, we compare our analytic results with soft sphere simulations of finite-system size to corroborate our calculation. However, the finite-system size also introduces surprising modifications to the analytical phase diagram.

Lee *et al.*'s simulations are computationally intensive because they describe the full motion of spheres inside a rotational flow, including inertia. Our finite-size simulations, however, have the advantage of being computationally inexpensive. They are based on energy minimisation and thus only describe the equilibrated columnar structure.

4.1 Lee *et al.*'s lathe experiments

A new experimental method of realising columnar structures has recently been introduced by Lee *et al.* [8]. We will summarise their work and results in this section. They suspended monodisperse spheres inside a denser rotating fluid. Rapid rotation of the system drives the spheres towards the axis of rotation where they assembled to different ordered structures. Due to the rotation, the centripetal force confined the spheres inside a harmonic potential, which strength can be tuned by the rotational speed.

Lee *et al.*'s experimental set-up is sketched in Fig 4.1. Polymeric beads of same diameter $d = 1.588\,\mathrm{mm}$ and same density ρ were placed in an aqueous solution of agarose and caesium bromide. The density was varied for different experiments between $\rho = 0.9-1.13\,\mathrm{g/cm}$. By adding the caesium bromide, the density of the fluid was increased above the density of the beads, resulting in buoyancy of the spheres. When rotated by a commercial lathe up to rotational speeds of $10\,000\,\mathrm{rpm}$, a centripetal force pushes the beads toward the central axis and the liquid to the wall of the tube. Because of a high Young's modulus of $E = 1325\,\mathrm{MPa}$ [95], these beads are impenetrable and behave like hard spheres.

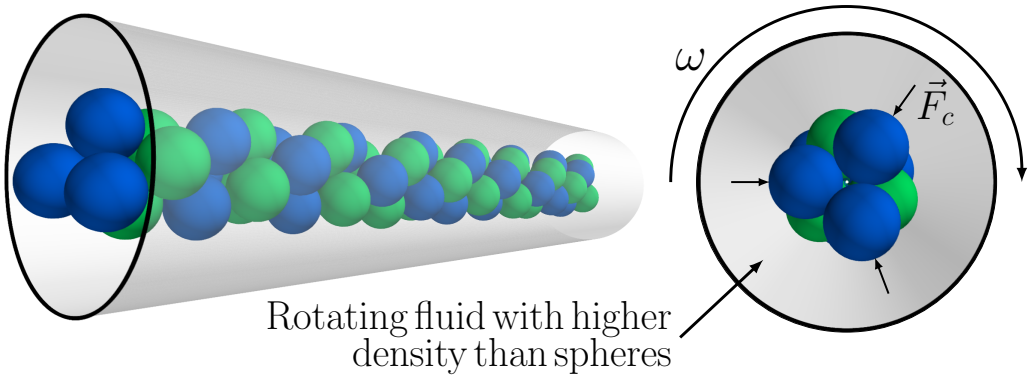

Fig 4.1: Experimental set-up for assembling columnar structures of spheres inside a rotating liquid-filled tube. The liquid has a higher density than the spheres, making the spheres buoyant. When the system is rotated with a rotational speed ω, the spheres experience a centripetal force $\boldsymbol{F}_c$ pushing them towards the axis of rotation. They assemble around this axis into different columnar structures. [I reproduced the image after Lee *et al.*'s experimental description [8].]

Different structures were interconverted upon increasing or decreasing the rotation of the tube. Additionally, the structure was determined by the number of polymeric beads inside the cylindrical tube at fixed length, i.e. the number density of the system. With the agarose, the assembled structures were solidified by gelation and turned into permanent structures after the assembly process. The assembly process was recorded with a high speed camera to investigate the structure before the solidification.

In order to gain further insides into the assembly process, Lee *et al.* complemented their experiments with Molecular Dynamics (MD) simulations of (essentially) hard spheres. These simulations describe the full motion of the spheres within a rotational flow. Thus, they included inertial forces, drag forces in a viscous fluid, buoyant forces, and sphere–sphere interaction forces in their simulation, but no hydrodynamic interactions.

Depending on the rotational speed ω and the number of spheres, two different types of columnar structures were observed in experiment and simulation. The structures were either homogeneous, i.e. a single phase structure filling

out the entire length of the cylindrical tube, or a binary mixture, a mixture of two structures with an interface. Two examples for each type of structure are shown in Fig 4.2. In Fig 4.2(b) the interface of the binary structure is highlighted.

The existence of binary mixtures seems to be surprising on first sight because the Mermin–Wagner theorem [96] states that spontaneous symmetries cannot be broken for structures in one- and two-dimensions at finite temperature. We showed in chapter 2 that the types of columnar structure that we consider in this thesis can be reduced to two dimensions. Due to the cylindrical confinement, the degrees of freedom of each sphere are only the height z and azimuthal angle θ. This may lead to the conclusions that the Mermin–Wagner theorem prohibits binary mixtures in Lee *et al.*'s experiments. However, the structures in this chapter have three degrees of freedom: each sphere can potentially move in radial direction as well. This allows the existence of binary mixtures where the spheres of each structure have different radial positions.

For both, experiment and simulations, phase diagrams in terms of rotational speed vs number density were extracted (see Fig 4.3) [8]. The horizontal axes of the phase diagram consisted of the normalised particle number n/n_0. The number n corresponds to the number of polymeric beads in the tube and n_0 is the number of beads needed to form a linear chain inside the tube. Thus, at $n/n_0 = 1$ the linear chain is observed.

Both phase diagrams resulted in the familiar sequence of columnar hard sphere packings: The legend on the side of Fig 4.3(a) and (b) shows the same sequence of homogeneous structures as the uniform structures in Fig 2.5. However, no intervening "line slips" were discovered (explanation for line slip in chapter 2.3.2). Instead they report on mixed structures of two columnar hard sphere packings of different diameter ratios D/d.

Lee *et al.* also reproduced all their experimentally observed structures with simulations. However, comparing the experimental phase diagram (Fig 4.3(a))

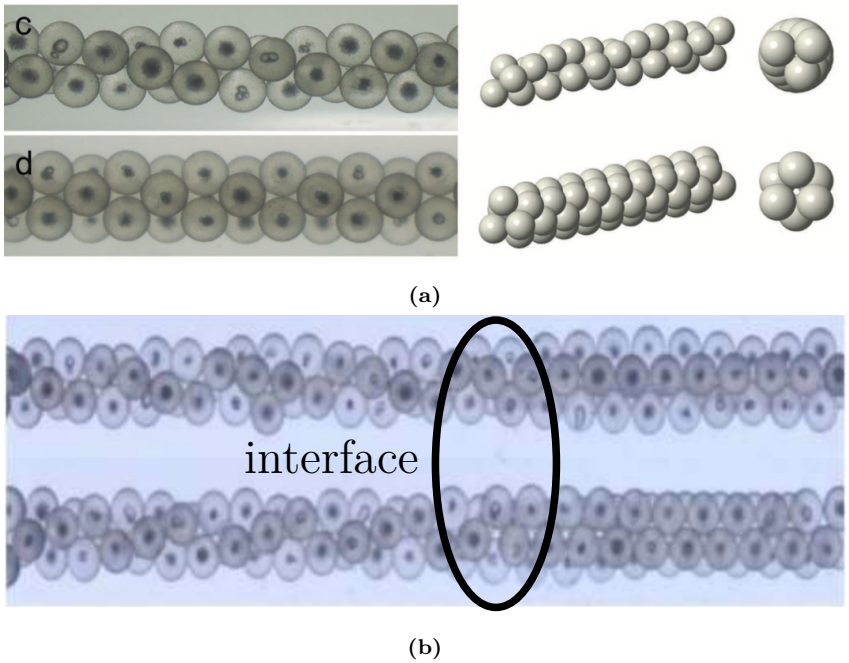

Fig 4.2: Examples of observed columnar structures by Lee *et al.* [8] in lathe experiments involving rapid rotations. Depending on the number of spheres and the rotational speed ω, the polymeric beads assembled around the rotating axis either as homogeneous structures (a) or binary mixtures (b) of two homogeneous structures. Homogeneous structures are single phase structures, filling out the whole tube. A binary mixture consist of two structures with a visible interface, highlighted by the black ellipse in (b). [Both images were extracted from Ref [8].]

with the one from the simulations (b), a shift towards lower number density can be observed for the experiments. While this is not discussed in Ref [8], we think that possibly vibrations due to the spinning of the lathe might be the cause for this. We experienced a similar shift in our analytic calculations to Lee *et al.*'s experiments, which is discussed in section 4.2.2.

Lee *et al.* also discovered that the chirality (see chapter 2.3) for helical assembles can be controlled by the orientation of the axis of rotation of the tube with respect to gravity. While experiments with horizontal tubes had no preferences for the chirality, in an inclined tube, the beads first localised at the top end. During the rotation they then formed helices of the preferred

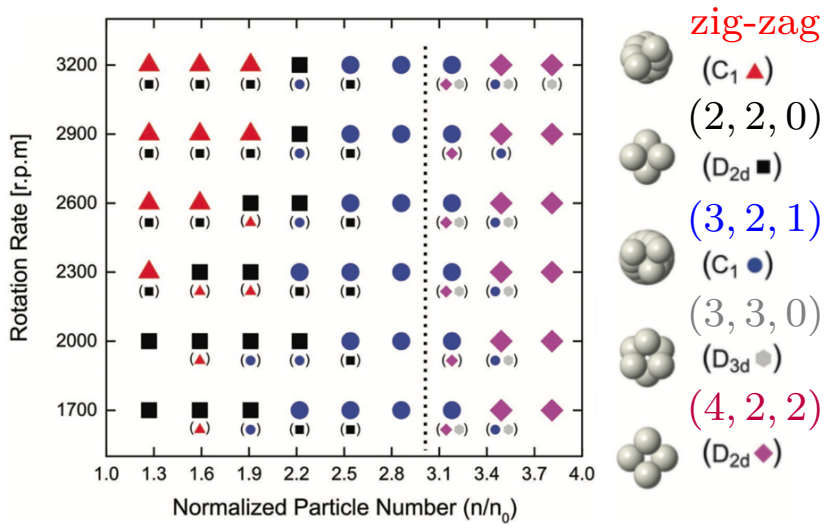

(a)

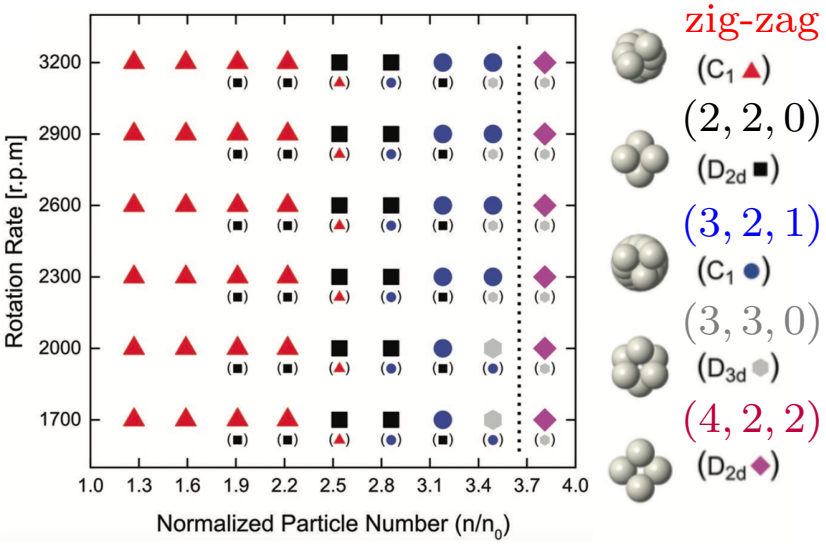

(b)

Fig 4.3: Lee *et al.*'s phase diagram constructed from experiments (a) and simulations (b) in terms of rotational speed (or rate) vs the normalised particle number n/n_0, which is a similar quantity to the number density. n is the number of spheres in the system and n_0 relates to the number of spheres that are needed to form a linear chain inside the tube. Homogeneous structures are marked with a single symbol (see legend on the side) and for mixtures the less dominant structures are indicated by the symbols in parentheses below. [Both images are taken from Ref [8].]

handedness. This effect was also reproduced in their simulations.

In further experiments columnar structures with bidisperse polymeric beads (of same density) were studied as well [8]. The larger polymeric beads assembled in a chain along the axis of rotation, while the smaller beads arranged around them. The authors also presented preliminary results for beads assembled at the interface of two immiscible fluids. These resembled structures of spheres assembled on the surface of a cylinder. Finally, experiments of exploratory kind were also done with bubbles. The reported findings only concerned simple linear chain structures, where the bubbles aligned along a straight line.

4.2 Theory of columnar structures formed by rapid rotations

Our approach here analyses Lee *et al.*'s assembly method using the soft sphere model. We will first focus on the rotational energies of hard sphere structures in section 4.2.1, which can be derived from previous findings. The soft sphere model then allows us to analytically calculate the total energies for soft spheres in such a system (section 4.2.2). From these we deduct a phase diagram for columnar structures without internal spheres, which is rich in interesting features.

4.2.1 Energies of hard sphere structures

As described in chapter 2.4, Mughal *et al.* [14, 71, 72, 87] have computed the densest columnar structures of hard spheres inside a cylinder. While there is no mathematical proof of these results, they have been corroborated by others [64, 65] and are in little doubt. The packing fraction ϕ of the densest structures was computed as a function of the ratio D/d of cylinder to sphere

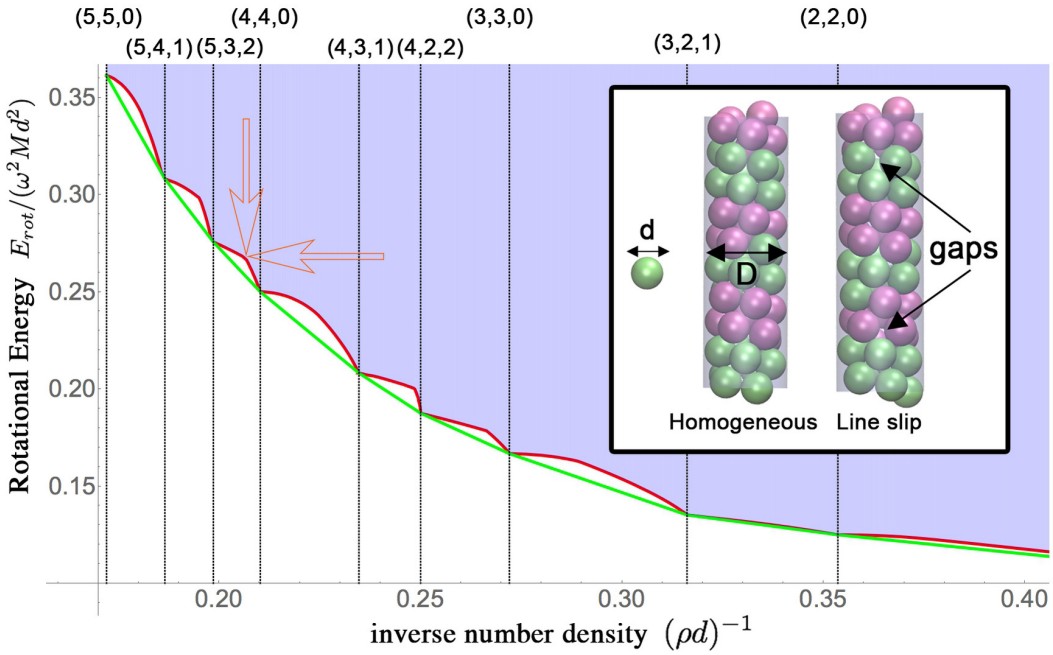

Fig 4.4: Minimal rotational energy $E_{\rm rot}$ as a function of dimensionless inverse number density $(\rho d)^{-1}$ for *hard sphere* packings. The energy of the line-slip packings is given by the solid red line. Vertical black lines indicate the location of homogeneous (in chapter 3 called uniform) structures, identified by indices (l, m, n). The *straight* solid lines (green line) between adjacent homogeneous structures indicates that binary mixtures have a lower energy compared to line-slip packings. The shaded area is the region of all possible hard sphere packings which have a single value of distance R from the central axis, by definition this precludes binary mixtures. The inset shows examples of a homogeneous and a line-slip structure. See text for an interpretation of the two red arrows in the main figure.

diameters (Fig. 2.5 in chapter 2.4). Up to $D/d \approx 2.7$ these structures include only spheres in contact with the confining cylinder, so that all spheres are at the same distance R from the central axis. All of the homogeneous structures considered here are of this type.

The densest hard sphere packings can be classified as either *homogeneous* (in chapter 2 and 3 called uniform structure [14]) packings or *line-slip* arrangements; examples of both are shown in the inset of Fig. 4.4. For a homogeneous arrangement, each sphere is in the same relation to six neighbouring spheres.

Such structures can be classified using the *phyllotactic* notation, i.e. a triplet of positive integers $(l = m + n, m, n)$ with $m \geq n$. This notation is explained in detail in the introduction of chapter 1.3.

Intervening between these homogeneous packings, which are found at particular values of D/d, are line-slip structures in which contacts are lost along a line separating two spiral chains of the homogeneous structure as explained in detail in chapter 2.3.2.

We can transform known hard sphere packing results to give us the lowest (rotational) energy per sphere (that is, the minimal R) as a function of the dimensionless inverse number density $(\rho d)^{-1}$ (see Fig 4.4), as follows. If the rotational velocity is ω, then by the parallel axis theorem, the rotational energy per sphere is

$$E_{\mathrm{rot}} = \frac{1}{2}\omega^2(I_0 + MR^2)\,, \tag{4.1}$$

where $I_0 = Md^2/10$ is the moment of inertia of a sphere with mass M and sphere diameter d. Since the moment of inertia of a sphere is independent of the distance from the axis R, we will omit this term in the calculations below. For hard sphere packings the sphere centres are located at a distance $R = (D - d)/2$ from the cylindrical axis, thus the rotational energy for hard sphere packings is given by

$$E^{\mathrm{H}}_{\mathrm{rot}} = \frac{1}{8}\omega^2 M(D - d)^2\,. \tag{4.2}$$

The dimensionless inverse number density $(\rho d)^{-1}$ can be computed from the diameter ratio and the packing fraction ϕ.

For a finite system of length L and number of spheres N, ϕ is given by

$$\phi = \frac{4NV_{\mathrm{Sphere}}}{\pi D^2 L} = \frac{2}{3}\frac{Nd}{L}\frac{d^2}{D^2}\,, \tag{4.3}$$

where V_{Sphere} is the volume of a sphere. In the limit of an infinite system ($N \to \infty$ and $L \to \infty$), the number density ρ is introduced $Nd/L \to \rho$.

Rearranging eq 4.3 for the inverse number density, we then get

$$(\rho d)^{-1} = \frac{2}{3}\left(\frac{d}{D}\right)^2 \phi^{-1}\,. \tag{4.4}$$

Fig 4.4 implies that the homogeneous structures, which occur for special values of $(\rho d)^{-1}$, minimise the rotational energy per sphere and we expect to observe this type of structure at these values of $(\rho d)^{-1}$. In the intervening ranges, however, binary mixtures (consisting of two-phase structures) of the adjacent homogeneous structures are expected. The energies of the binary mixtures, dictated by the usual Maxwell (common tangent) construction, lies below the line-slip energies in Fig 4.4.

For the homogeneous structures as well as line-slip arrangements, the packing inside the cylindrical channel is filled with a single structure. Thus, these structures do not need to accommodate an interface. The binary mixture, however, consists of two structures that differ in their D/d and therefore has an interface. While the Maxwell construction predicts the energy for an infinite system and neglects this interface energy, for finite-system sizes this interface energy plays an important role (see section 4.3).

Note that the hard sphere limit may be approached in two ways as indicated by the red arrows in Fig 4.4: Following the horizontal arrow, we approach the hard sphere limit by a volumetric change, as done in the packing simulation of chapter 3. This approach is essentially described by reducing the pressure in the phase diagram of Fig 3.2. The vertical approach to the hard sphere limit is achieved by changing the rotational speed, as in this chapter. We will discuss the phase diagram related to the vertical red arrow in section 4.2.2.

The resultant structure sequence is in accord with the findings of Lee *et al.* [8]. In the following we address its modification in the case of soft spheres and finite column length.

4.2.2 Analytic soft sphere energy calculations

The effect of moving away from the hard sphere limit is to widen the range in which the homogeneous (l, m, n) structures are found. This can be quantified and understood in terms of a transparent analytical description, illustrated by Fig 4.5 and described below.

For a rotating column of soft spheres the energy per sphere is given by

$$E^{\mathrm{S}}_{\mathrm{rot}} = E_{\mathrm{rot}} + E_o \,, \tag{4.5}$$

where the second term is due to the sphere–sphere interaction. We use the same soft sphere interaction between sphere i and j as described in chapter 2.2.2, namely

$$E_{ij} = \begin{cases} 0 & \delta_{ij} > 0 \\ \frac{1}{2} k \delta_{ij}^2 & \delta_{ij} \leq 0 \end{cases} \tag{4.6}$$

where k is the spring constant. The overlap $\delta_{ij} = |\boldsymbol{r}_i - \boldsymbol{r}_j| - d$ depends on the sphere positions $\boldsymbol{r}_i$ and $\boldsymbol{r}_j$.

The total overlap energy per sphere E_o can be written as

$$\begin{aligned} E_o &= \frac{1}{2} \frac{k}{N} \sum_{\substack{i,j=0 \\ i \neq j}}^{N} \delta_{ij}^2 \\ &= \frac{1}{2} k \left\langle \delta_{ij}^2 \right\rangle \,, \end{aligned} \tag{4.7}$$

i.e. it is obtained by summing over all pairwise interactions and dividing by the total number of spheres in the structure. Thus the energy per sphere is given by,

$$\frac{E^{\mathrm{S}}_{\mathrm{rot}}}{M\omega^2 d^2} = \frac{1}{2} \frac{R^2}{d^2} + \frac{1}{2} \frac{k}{M\omega^2} \left\langle \left(\frac{\delta_{ij}}{d} \right)^2 \right\rangle \,. \tag{4.8}$$

Homogeneous structures are comprised of packings for which each sphere is in an identical relationship to every other sphere in the packing. Each sphere is at a distance R from the central axis and is in contact with six neighbouring spheres. From these constraints, it follows that for a given number density

ρ, the energy of a homogeneous structure can be varied *only* by a uniform radial compression/expansion or twist, if it is to remain homogeneous (as we assume here). Thus the energy per sphere for all homogeneous structures is an analytic expression to be minimised with respect to only two variables: R and a twist angle α [14]. In the case of achiral structures this twist angle is zero due to symmetry, and only one free variable remains.

The detailed calculation for the analytic energy expression of all homogeneous and achiral $(l, l, 0)$ structures (i.e. $(2, 2, 0)$, $(3, 3, 0)$, $(4, 4, 0)$, etc.) is given in Appendix A.3. The minimal energy can either be found by a root search of the gradient or using a numerical minimisation routine for scalar functions.

The minimised energies of all homogeneous structures as a function of the inverse number density $(\rho d)^{-1}$ are shown for two different values of $\omega^2 M/k$ in Fig 4.5. These calculations are based on the full harmonic interactions between neighbours (see below for justification). The common tangents between adjacent curves are shown by the black lines and the points of contact between the tangent and the curve by black dots. Where the common tangents are below the energy curves of the homogeneous structures, the binary mixtures are more stable. For the other values of $(\rho d)^{-1}$, highlighted by the shaded strips, a homogeneous phase is predicted. Low values of $\omega^2 M/k$ correspond to the hard sphere limit (see Fig 4.5(b)); with increasing $\omega^2 M/k$ the overlap between spheres increases, resulting in a broadening of the range over which homogeneous structures are observed.

There is no loss of contacts in the range in which homogeneous structures are predicted. This justifies the simplification that resulted from not taking loss of contacts into account, i.e. using the full harmonic approximation of interactions.

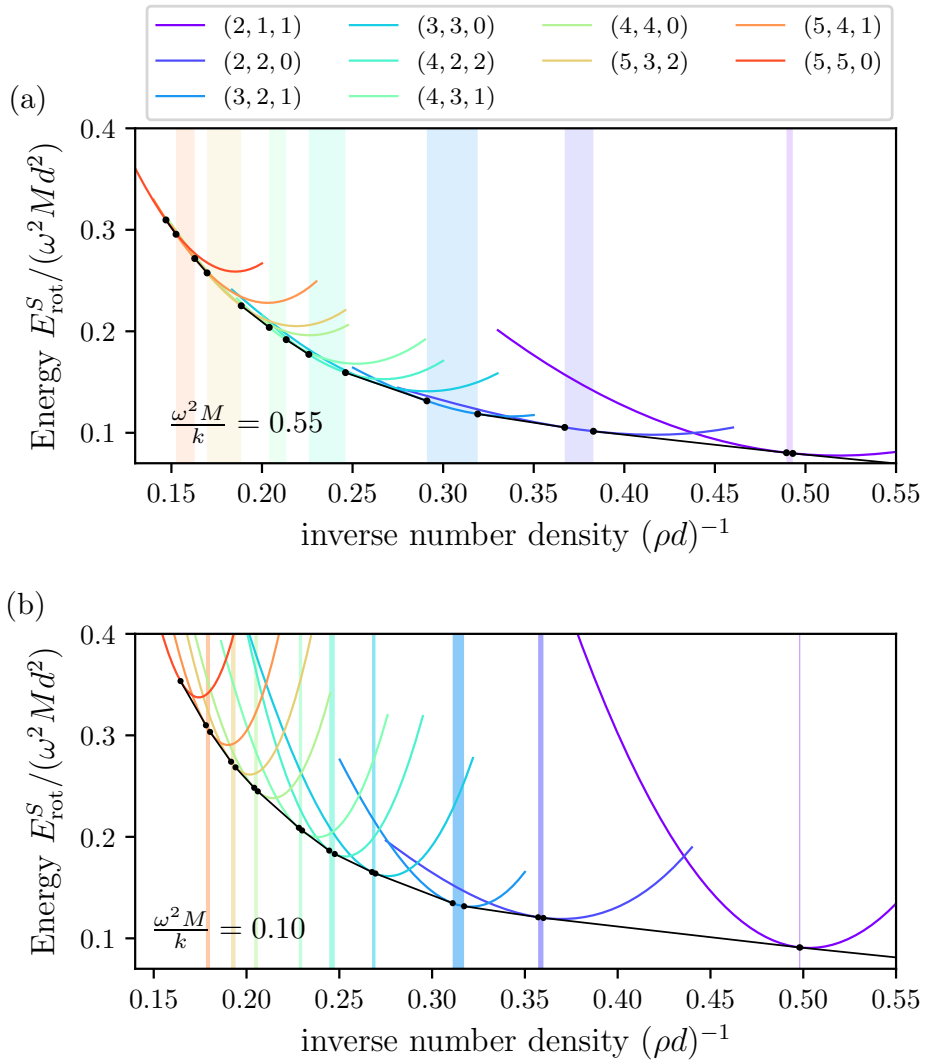

Fig 4.5: Minimal energy per sphere for all homogeneous structures as a function of dimensionless inverse number density $(\rho d)^{-1}$ for the case of *soft spheres*, with harmonic interactions (see text). (a) shows the result for $\omega^2 M/k = 0.55$ and (b) for $\omega^2 M/k = 0.10$, which is close to the hard sphere limit. Common tangents between adjacent homogeneous structures are shown by the black lines and the black dots are the tangent points. The ranges over which homogeneous structures are expected, are highlighted by shaded strips (coloured according to the appropriate homogeneous structure - see key). Outside these ranges the common tangents have a lower energy and binary mixtures are expected.

The corresponding analytically calculated phase diagram [1] is shown in Fig 4.6. In the hard sphere limit ($\omega^2 M/k \to 0$), the values of $(\rho d)^{-1}$ for the homogeneous structures are consistent with those from the simulations of Lee *et al.* [Fig 4.3(b)] which we have indicated by points with dashed horizontal error bars. Lee *et al.*'s experimental data are shifted toward higher values of $(\rho d)^{-1}$. This is possibly due to vibrations, keeping the hard spheres slightly apart, which gives them an effective diameter larger than their actual size. We report on a similar effect in experiments of the next chapter 5.5.

With increasing $\omega^2 M/k$ the ranges of homogeneous structures expand, as expected. The upper part of the phase diagram is, however, much richer in detail than anticipated. Of special interest is the vanishing of the homogeneous achiral structures $(3, 3, 0)$ and $(4, 4, 0)$ at a rotational velocity of $\omega^2 M/k \approx 0.5$. For high $\omega^2 M/k$ the achiral structures cannot compete with chiral structures: The latter can deform by twisting, while the former cannot.

At the values of $\omega^2 M/k$ where these achiral structures disappear, there are *peritectoid* points (see inset of Fig 4.6) [97]. The homogeneous structures vanish in a point and also their two adjacent binary mixtures disappear. Above these three structure a new binary mixture of the second nearest homogeneous structures emerges. The phase boundaries of the adjacent homogeneous structures show a change in slope where the new binary mixture appears. This is due to the change of the common tangent, now to be taken between the second-nearest homogeneous structures.

Note that a peritectoid transformation actually describes a type of isothermal reversible reaction from metallurgy, in which two solid phases react with

[1] The phase diagram was created by calculating the analytic energy for each homogeneous structure first and then finding each common tangent by a matching slope algorithm at a certain ω^2/Mk value. The points where the tangents meet the energy curves of the homogeneous structures are the borders of the coloured regions in the phase diagram. The resolution in ω^2/Mk is 0.01.

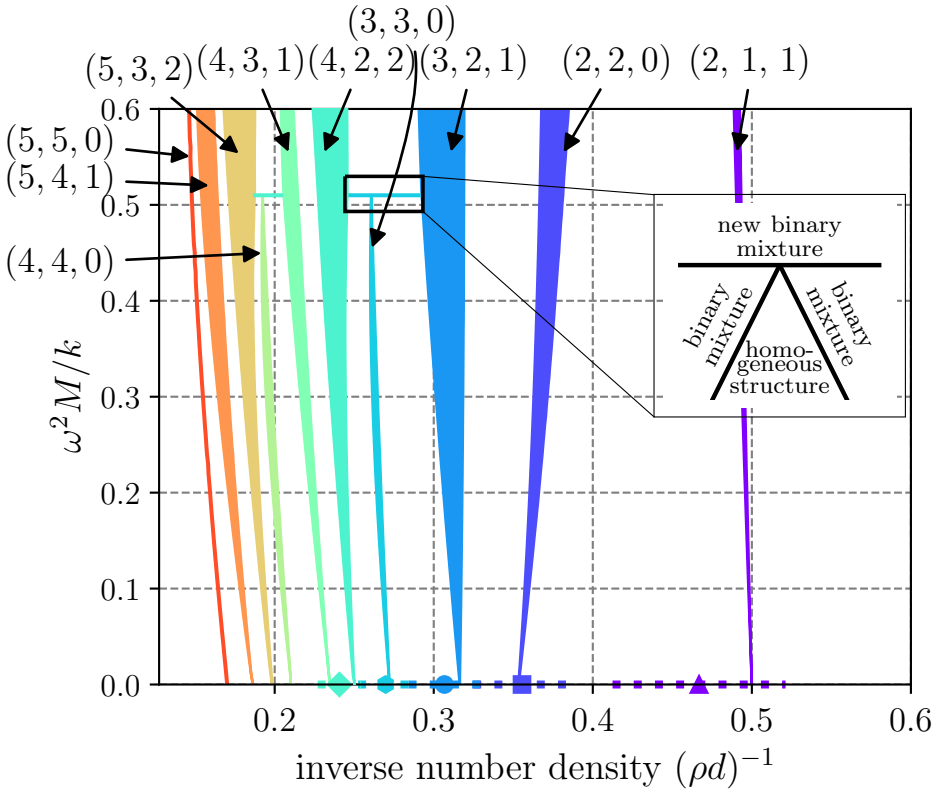

Fig 4.6: Calculated phase diagram of homogeneous structures (coloured, labelled regions) and their binary mixtures of adjacent homogeneous structures (intervening white space). Most homogeneous regions expand with increasing $\omega^2 M/k$ (i.e. rotation frequency) but the achiral $(3,3,0)$ and $(4,4,0)$ structures vanish in *peritectoid* points (see the inset) [97]. In the case of the $(5,5,0)$ phase only the right hand boundary can be shown, since it is the last structure without inner spheres. The $(\rho d)^{-1}$ values for the homogeneous structures are in good agreement with Lee *et al.*'s simulation results [8], indicated by points with dashed horizontal error bars in the hard sphere limit.

each to create an alloy that is a completely different solid phase. Our structure do not undergo any thermal reaction (since we do not have a thermal system). We still apply this term from metallurgy to our phase transitions because both share the same topological features in the phase diagram.

4.3 Finite-system size simulations of columnar structures by rapid rotations

The analytic results, however, are only valid for systems of infinite sample size. In order to corroborate our analytical results, but also extend them to investigations of finite-system sizes, we carried out finite-size simulations based on energy minimisation. This simulation model is explained in detail in the next section 4.3.1. These lead to the unexpected discovery of a line-slip arrangement in such a finite-size system. We present these results in form of a modified phase diagram (compared to Fig 4.6) in section 4.3.2.

4.3.1 The simulation model: Energy minimisation

We slightly modified the soft sphere simulation model described in 3.1 in order to simulate columnar structures of finite size assembled by rapid rotations. It can be used as more general numerical simulations for a finite system of N spheres which can occupy any position in a unit cell of length L (see Fig 4.7).

In doing so, we minimise the total energy per sphere

$$\frac{E(\{\boldsymbol{r}_i\},\alpha)}{M\omega^2 d^2} = \frac{1}{2N}\sum_{i}^{N}\left(\frac{R_i}{d}\right)^2 + \frac{1}{2}\frac{k}{NM\omega^2}\sum_{i=1}^{N}\sum_{j=i}^{N}\frac{|\boldsymbol{r}_i-\boldsymbol{r}_j|^2}{d^2} \tag{4.9}$$

with respect to all sphere positions $\boldsymbol{r}_i$ and twist angle α at fixed unit cell length L. For the rotational energy term we sum over all radial distances R_i^2 of sphere i and the interaction energy is again that of soft spheres. We have also applied twisted boundary conditions using image spheres above and below the unit cell as illustrated in Fig 4.7 [14] (see also chapter 3.1).

We use the Basin-hopping method [85] to search for the global minimal energy for particular values of number density $\rho = N/L$ and $\omega^2 M/k$. It is introduced in chapter 2.5.2 and described in detail in Appendix A.2.

We explore structures with low number densities between $2 < \rho d < 3$ ($0.3 < (\rho d)^{-1} < 0.5$ for the inverse number density). The number density ρd

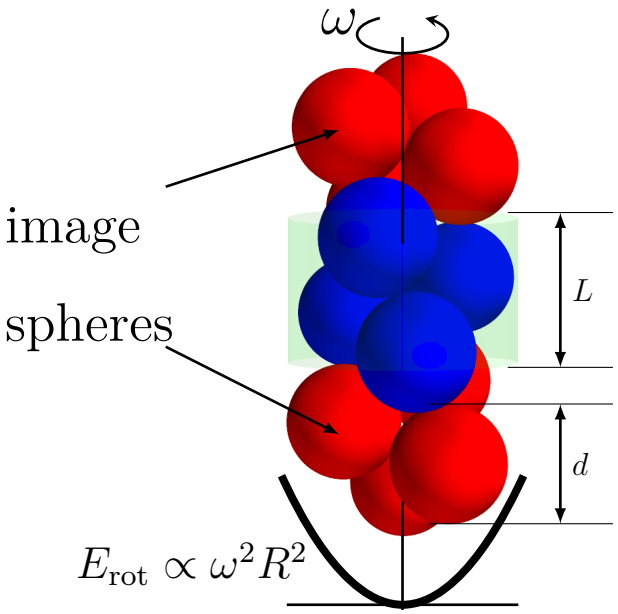

Fig 4.7: Simulation of N soft (overlapping) spheres (blue) with diameter d confined by a rotational energy E_{rot} in a unit cell of fixed length L. The spheres can now occupy any position within this unit cell. The energy E_{rot} is proportional to the rotational speed ω^2 and the radial distance from the central axis R^2. Periodic boundaries are again employed by image spheres (red) above and below the unit cell that are rotated by a twist angle α.

can be varied by fixing the sphere number N and adjusting the unit cell size L. From the hard sphere results we know that the only possible structures in this regime are the homogeneous phases $(2,1,1)$, $(2,2,0)$ and $(3,2,1)$ and their corresponding line slips. Finite values of N which are multiples of 12 are compatible with these structures. Thus, in the finite-size simulations presented here we have used $N = 24$.

4.3.2 Appearance of a line slip due to finite-size effects

We first compared our analytically calculated energies with energies from the finite-size simulations. An example of our numerical results for a low rotational velocity (i.e. $\omega^2 M/k = 0.2$) is shown in Fig 4.8. Here we explore the region between the $(2,2,0)$ and $(3,2,1)$ homogeneous soft sphere structures.

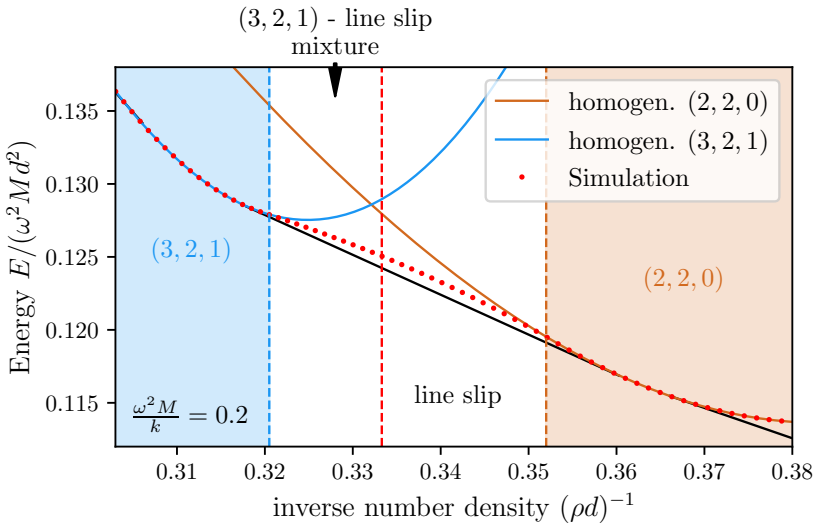

Fig 4.8: The red dots show the energy from finite-size simulations, for $\omega^2 M/k = 0.2$ and $N = 24$. Brown and blue solid lines are the previously analytically calculated energies for the labelled homogeneous structures, and the common tangents (black solid lines) represent their binary mixture. Within the vertical dashed red and brown line, a line-slip structure is observed. At the vertical dashed blue line the $(3, 2, 1)$ transforms into a binary mixture of a homogeneous and line-slip structure, whose energy is higher than that of the common tangent (due to finite-size effects).

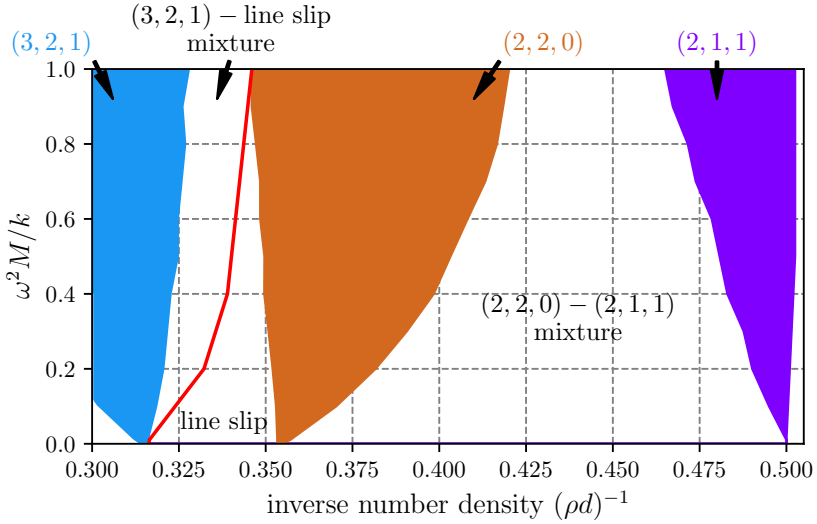

Fig 4.9: Numerically computed phase diagram from the finite-size simulation with $N = 24$ spheres. In addition to the expected homogeneous structures and binary mixture of $(2, 2, 0)$ and $(2, 1, 1)$, a line-slip arrangement, as well as its binary mixture with $(3, 2, 1)$ are found.

The blue and brown solid curves are their analytically computed energies; the solid black line is the common tangent between them. The numerically computed energy from the finite-size simulations, shown by the red dotted line, closely matches the analytic theory within the ranges of the homogeneous phases.

However, a notable difference arises for $0.3205 \leq (\rho d)^{-1} \leq 0.3520$. Here, the computed energy is slightly higher than that of the common tangent (binary mixture) due to finite-size effects. Between the dashed vertical blue $[(\rho d)^{-1} = 0.3205]$ and red lines $[(\rho d)^{-1} = 0.3333]$ we find a mixture of the $(3, 2, 1)$ uniform structure and a $(2, \mathbf{2}, 0)$ line slip. Between the dashed vertical red $[(\rho d)^{-1} = 0.3333]$ and the brown lines $[(\rho d)^{-1} = 0.3520]$ we observe only the line-slip structure.

In part these results corroborate those of the analytic treatment – in particular in regards to the homogeneous phases – but the intervention of the line slip was an unexpected effect of finite size. In these finite systems the interface energy of the binary mixtures has a finite contribution to the total energy, which decreases with increasing number of spheres. Results for the range in number density presented here, using $N = 48$ and 96, indicate that the binary mixture of two homogeneous phases is recovered for infinite system size. The energy per sphere for these system sizes approaches that of the common tangent.

From our finite-size simulations we finally compute a limited phase diagram, shown in Fig 4.9, to be compared with Fig 4.6. In the case of the $(2, 1, 1)$ and $(2, 2, 0)$ structures the intervening region is occupied as expected by the $(2, 2, 0) - (2, 1, 1)$ mixed phase structure. However, in the case of the $(2, 2, 0)$ and $(3, 2, 1)$ structures, the intervening region is split into two parts, featuring the line slip mentioned above for low values of $\omega^2 M/k$.

4.4 Conclusions

The phase diagram presented in Fig 4.6 provides an analytic guide to the expected occurrence of equilibrium structures in long rotating columns on the basis of a generic soft sphere model. It is packed with great features, such as the two peritectoid points, at which two achiral structures are predicted to vanish.

We have adduced results from more general simulations, as well. In part these results corroborate those of the analytic treatment – in particular as regards the homogeneous phases – but the intervention of the line slip was an unexpected effect of finite size. It is to be expected that line slips will play a role in all the other parts of the phase diagram, in simulations of finite-system size.

The wide range of other unexpected structures remains to be explored for future work, as well as a rigorous analysis of the asymptotic trend as N goes to infinity. Results for the line slip investigated here indicate that the binary mixture of two homogeneous phases is recovered in that limit. There also remains the case of hard wall boundary conditions at both ends of the tube in a finite sample, which is more directly relevant to the present experiments. The general simulations from this chapter can easily be modified in this direction by replacing the periodic boundaries with a wall potential at both ends.

The interesting feature of peritectoid points in the phase diagram has also not yet been explored in simulations and experiments. Since these points were discovered in the analytic calculations, they may only be features of infinite systems. Their relevance for finite system can be studied with the simulations introduced in this chapter. The experiments will have to be performed with spherical objects that are deformable because peritectoid points are features of soft systems. We will discuss possible future experiments of this kind using

hydrogel spheres in the outlook of chapter 6.

The finite-size effect of line slips should also be investigated in future experiments. Since we expect this finite-size effect also in the hard sphere limit, these experiments can conveniently be done with polymeric beads, as already used in experiments by Lee *et al.* In any such experiments, one should also be aware of the existence of metastability and hysteresis in macroscopic systems, which we explored in chapter 3.3 in a related context. All possible future investigations to this topic using simulations, as well as experiments will be discussed in detail in the outlook of chapter 6.

Chapter 5

Hard sphere chains in a cylindrical harmonic potential

Related publication:

1. J. Winkelmann *et al.* EPL **status:** accepted (2019).

Particles confined in the vicinity of a straight line by a radial potential have been found to exhibit a rich variety of structures, particular distorted linear chains [98]. In detail they depend on the interactions between the particles, the confining potential and any boundary conditions at the end of a finite sample.

We discovered that such a structure can be also be assembled and investigated with the elementary experiment introduced by Lee *et al.* [8] at very low number densities ρ (see previous chapter 4.1). When the number of spheres is commensurate with the length of the rotating tube, the spheres assemble in a linear chain. By reducing the tube length, the system is compressed and localised buckling of the chain is observed.

In the introduction of this chapter (section 5.1) we sketch the complex scenario of such a sphere chain and give examples of previous experimental system. Landa *et al.* [99] observed for such a system that appearing zigzag structures are induced by bifurcations in experiments with ion traps.

We find similar observations in our experiments using rapid rotations (see section 5.5), which are of much simpler nature. Our experiments are complemented with transparent theoretical models that are amenable to very simple methods. We first introduce our numerical methods in section 5.2 with which we investigate a wide range of predicted structures (section 5.3), before we also present an analytic linear approximation (section 5.4).

5.1 Introduction to sphere chains in a cylindrical harmonic potential

5.1.1 Localised buckling in compressed sphere chains

The system of interest in this chapter consists of N identical spheres in a rotating liquid-filled tube of length L. The system is confined by flat walls at both ends of the tube. Since the spheres are buoyant, the centripetal force drives them towards the central axis where they are confined inside a cylindrical harmonic potential.

If the number of polymeric beads is commensurate with the length of the tube ($L = Nd$), they arrange in a straight chain as depicted in Fig 5.1(a). The chain experiences localised buckling, when the tube length is reduced to length $L < Nd$ (Fig 5.1(b)). We will refer to such a structure as a *modulated zigzag* structure. We use this set-up to investigate this buckling behaviour of a chain of spheres confined by a harmonic potential experimentally as well as theoretically.

We focus on the question: *In what force equilibrium configurations does a chain of hard spheres in a cylindrical harmonic potential arrange, when compressed between two plates?* The lathe experiments by Lee *et al.* provide a very clear and elementary experimental system for such investigations.

Previous experiments of such system have been carried out with ion traps

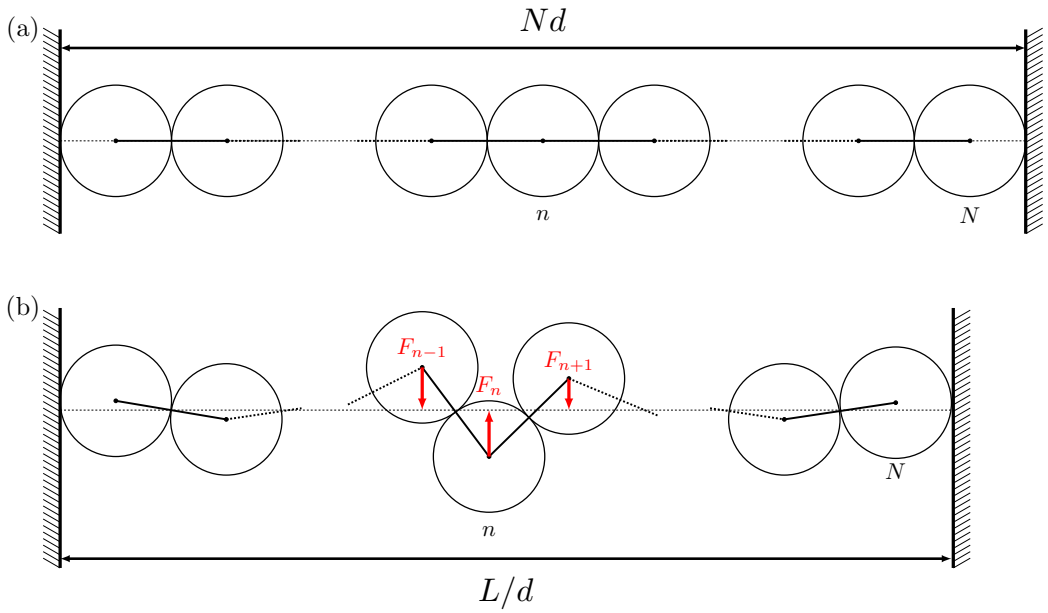

Fig 5.1: Chain of N spheres of diameter d inside a cylindrical harmonic potential in radial direction confined between two planar wall boundaries. (a) shows the linear, uncompressed chain, where the distance of the planar boundaries is commensurate with the number of spheres. At closer distance L, the system is compressed and experiences local buckling (b). Due to the harmonic potential, a force F_n pushes the spheres toward the axis of rotation (dashed line).

[100–105] and granular media as well as colloids [106, 107], but also finite dust clusters [108], overdamped colloids systems [109] and microfluidic crystals comprising of droplets [110]. The complex scenario of appearing zigzag structures, induced by bifurcations, has been sketched by Landa *et al.* [99]. In these experiments N ions are trapped within a quadripolar confining potential and their ion–ion interaction is described by Coulomb's law. The traps are experimentally realised with oscillating electric fields with trapping frequency ω.

Fig 5.2 presents schematically the bifurcation diagram for appearing zigzag structures. The parameter $\gamma_y = \omega_y^2/\omega_x^2$ is related to the trapping frequencies of the laser light of the ion traps holding the ions in place for the axial (ω_x) and radial direction (ω_y). Thus, it determines the confinement strength in

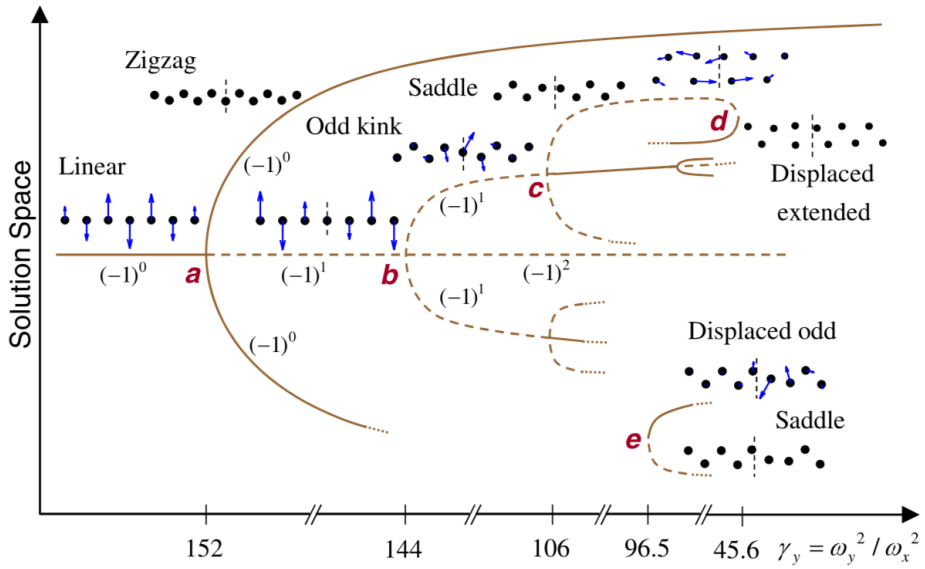

Fig 5.2: Schematic bifurcation diagram introducing different zigzag structures, observed in experiments with ion traps [99]. The frequencies ω_y and ω_x are the trapping frequencies of the optical traps in radial and axial direction. The parameter $\gamma_y = \omega_y^2/\omega_x^2$ determines the confinement in radial direction. Note that it decreases from left to right. Solid lines indicate stable configurations and dashed lines are unstable solutions with at least one negative eigenvalue of the Hessian matrix. The spatial configurations are depicted by showing a few ions at the crystal centre, together with the line of axial symmetry of the structure.

radial direction: the higher γ_y, the higher the radial confinement.

At high confinement strength only the linear chain occurs. Upon lowering the γ_y, zigzag structures are introduced by bifurcations. At this point the previous linear chain becomes unstable and two new stable zigzag structures emerge. Those two structures are radial mirror images of each other and thus degenerate in their energy.

For theoretical approaches, the stability of such structures can be tested with the aid of the Hessian matrix. One or more negative eigenvalues of the Hessian indicate that a structure is unstable. In Fig 5.2 the number of negative eigenvalues n is displayed in the form $(-1)^n$. At each bifurcation point the sum of local indices of all solutions is conserved before and after the bifurcation.

Bifurcation theory in general studies the changes in the topological structure of the solutions of a family of differential equations. These equation are most commonly applied to dynamical systems. A bifurcation occurs in such systems when a small change made to the bifurcation parameter causes a sudden topological change in its behaviour. The systems considered in this chapter are neither dynamical nor described by a family of differential equations. However, sudden topological changes in the modulated zigzag structures are also observed, after a small change to a parameter value. This bifurcation parameter is in the case of the ion traps γ_y and in our system involving rapid rotations the compression Δ which we will explain in the next section. Bifurcation theory suggests that such structures may be described by a family of differential equations (at least in the continuous limit).

5.1.2 The compression Δ

In the previous chapter 4 we used the number density ρ as the structure-defining parameter in the hard sphere limit for infinitely long structures. But due to the buckling behaviour of these structures when confined between two flat walls, the number density can vary locally and is thus not a suitable parameter.

As a structure-defining parameter we therefore introduce the dimensionless compression Δ, defined as

$$\Delta = \frac{Nd - L}{d} = N - L/d\,, \tag{5.1}$$

where d is the sphere diameter and L is the tube length.

It measures how much the tube length L is reduced compared to the length of a linear chain which is given by Nd. In Fig 5.1 it is the horizontal distance between the right-hand-side wall in (a) and the right-hand-side wall in (b).

The relevant structures in this chapter have a compression below $\Delta = 1.3$, where the modulated zigzag structure are observed. This corresponds

to (average) number densities close to $\rho d = 1$ (not displayed in the phase diagram Fig 4.6). In this range, the structures are all *planar*.

5.2 Numerical methods and simulations

The rich scenario of structural transitions within this regime under increasing compression is predicted in detail by the analysis provided in this section. It uses two numerical methods: an iterative stepwise solution for calculated positions from force equilibrium and a simulation based on energy minimisation. While the iterative stepwise method is based on the planar geometry of the chain structure and force equilibrium, the simulation is more general by not restricting the minimisation in any way.

Both theoretical models introduced are very transparent, and amenable to very simple methods. They both neglect the full movement of the spheres during the assembly process. Instead, only equilibrated structures are simulated.

Even though the experimental system, is a highly driven system due to the rapid rotations of the lathe, there is no need to consider non-equilibrium effects. The structures that assemble are in a stationary state that allows us to describe them as if they are in force equilibrium. While the whole system is rotating at high speed, the (centripetal) forces acting on each sphere are constant over time, leading to force equilibrium.

5.2.1 Iterative stepwise method

In the experimental system, detailed below, each sphere of mass m experiences a centripetal force $f_c = m\omega^2 R$, where R is the distance of its centre from the central axis of the tube and ω is the rotational speed. For the case of no compression ($\Delta = 0$) the spheres align in a linear chain along the central axis. At a finite compression ($\Delta > 0$) the chain starts to buckle and the

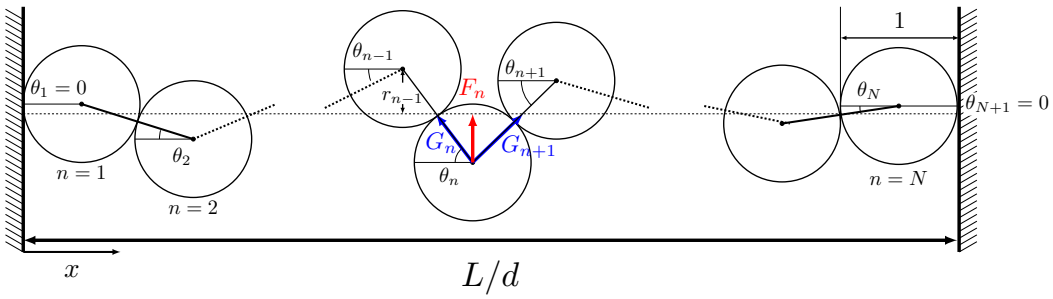

Fig 5.3: Sketch of the arrangement of spheres at the two walls and the interior of the *modulated zigzag* structure that is formed when N spheres are compressed between two hard walls. Shown is the notation used for the stepwise solution. Each sphere, displaced from the central axis (dashed line) by the dimensionless distance r_n, experiences a dimensionless centripetal force $F_n = r_n$ pulling it towards the axis and a compressive force G_n. θ_n is the angle between the line connecting the centres of spheres $n-1$ and n and the central axis. At the wall the line of contact is in the x direction, i.e. $\theta_1 = \theta_{N+1} = 0$.

structures of force equilibrium take the form of modulated zigzag structures as illustrated in Fig 5.3. We developed an elementary stepwise method to describe such structures for low energies.

In the following we will use the dimensionless distance from the central axis for each sphere $r = R/d$ and the dimensionless centripetal force

$$F = f_c/(m\omega^2 d) = r\,. \tag{5.2}$$

Our aim is to calculate the dimensionless forces $F_n = r_n$ and tilt angles θ_n, as defined in Fig 5.3, for $n = 1$ to N spheres. Considerations of force equilibrium and geometrical equations yield iterative relations for F_n (or r_n) and θ_n as follows.

The compressive forces G_n between contacting spheres are given by

$$G_n \cos\theta_n = G_0 \tag{5.3}$$

from the condition of force equilibrium in the x direction, which is that of the central axis. G_0 is the magnitude of the compressive force at each end of the system.

The equilibrium of centripetal forces F_n on the nth sphere gives

$$\begin{aligned} F_n &= G_n \sin\theta_n + G_{n+1} \sin\theta_{n+1} \\ &= G_0(\tan\theta_n + \tan\theta_{n+1}). \end{aligned} \tag{5.4}$$

The centres of contacting spheres are separated by their diameters. Hence the radial distances and forces are

$$\begin{aligned} r_n + r_{n+1} &= \sin\theta_{n+1}\,, \\ F_n + F_{n+1} &= \sin\theta_{n+1}\,. \end{aligned} \tag{5.5}$$

The above equations then relate θ_{n+1} and F_{n+1} to θ_n and F_n, i.e.

$$\begin{aligned} \theta_{n+1} &= \arctan\left(\frac{F_n}{G_0} - \tan\theta_n\right), \\ F_{n+1} &= \sin\left[\arctan\left(\frac{F_n}{G_0} - \tan\theta_n\right)\right] - F_n. \end{aligned} \tag{5.6}$$

These equations may be used in a "shooting method" to find solutions for a specified value of G_0. The hard-wall boundary condition for sphere $n = 1$ requires the first tilt-angle θ_1 to be zero, with an arbitrary F_1. Using eqs. (5.6) we proceed iteratively to (F_{N+1}, θ_{N+1}). The angle θ_{N+1} corresponds to the contact of the Nth sphere with the wall, as illustrated in Fig 5.3.

We search for values of F_1 (in general more than one) such that the angle θ_{N+1} is zero, satisfying the second hard-wall boundary conditions. This search is performed by coarse graining the initial force F_1 over a range of $0 < F_1 \leq 0.01$ in steps of 10^{-4}. These values are then used as brackets in a bisection method.

The non-dimensional total energy E of such a hard sphere structure consists only of the rotational energy,

$$E = \frac{E_{\mathrm{rot}}}{m\omega^2 d^2} = \frac{1}{2}\sum_{n=1}^{N} r_n^2\,, \tag{5.7}$$

where as in the previous chapter 4 we have omitted the (constant) energy contribution due to the moment of inertia of the spheres. The compression Δ

from eq. (5.1) is given by

$$\Delta = N - \sum_{n=1}^{N} \cos\theta_n \,. \tag{5.8}$$

By performing the root search at varying compressive forces G_0, we can accumulate a data set, for which we can calculate the energies and compressions in this way.

5.2.2 Simulations based on energy minimisation

To confirm and supplement the results of the stepwise method we also seek equilibrium configurations using energy minimisation starting from random configurations. These simulations are more general than the stepwise method since they are *not* restricted to be planar. They enable us to confirm that the structures found by the stepwise method are indeed the lowest energy configurations.

In practice we encounter difficulties with the stepwise method beyond a compression of $\Delta \geq 0.9$ (for $N = 20$). Our implementation based on the bisection search method has problems to find all solutions above this point. We expect to successfully extend the application of the stepwise method to this regime by means of other root finding methods. Results for larger compressions can be generated instead by energy minimisation. We have found it convenient to perform energy minimisation on a system of *soft* spheres, and extrapolate to the limit of hard spheres. The concept behind these energy minimisation simulation are the same as discussed in previous chapters 3 and 4.

The total non-dimensional energy E^{S} for N *soft* spheres (of diameter d)

longitudinally confined between length L is given by,

$$E^{\mathrm{S}} = \frac{1}{2}\sum_{n=1}^{n=N} r_n^2 + \frac{1}{2}\left(\frac{k}{m\omega^2}\right)\left(\sum_{\substack{n,m=1\\ m<n}}^{N}\left(\frac{\delta_{nm}}{d}\right)^2 + \left[\left(\frac{\delta_1}{d}\right)^2 + \left(\frac{\delta_N}{d}\right)^2\right]\right). \tag{5.9}$$

The first term is the rotational energy of each sphere. The second term accounts for the overlap between any two spheres, where the overlap between spheres n and m is defined as $\delta_{nm} = |\boldsymbol{R}_n - \boldsymbol{R}_m| - d$, where $\boldsymbol{R}_n$ and $\boldsymbol{R}_m$ are the centres of two contacting spheres in cylindrical polar coordinates. The final term accounts for the overlaps δ_1 and δ_N of the two end spheres with the two boundaries. As in previous chapters the soft sphere terms only contribute, if $\delta_{nm} < 0$ (and for the boundaries $\delta_1 < 0$ or $\delta_2 < 0$).

For any given values of compression Δ and $k/m\omega^2$ we find equilibrium solutions (stable or metastable) by varying the coordinates of the sphere centres and minimising the total energy. It is sufficient here to use a local minimisation routine such as gradient descent or BFGS (see chapter 2.5.1 or for details in Appendix A.2). Finally, by performing a series of simulations with increasing values of $k/m\omega^2$ we can extrapolate to the hard sphere case (i.e. $k/m\omega^2 \to \infty$) and compare directly with the stepwise method.

The solutions from the stepwise method are only in force equilibrium, i.e. they can be stable or unstable solutions. We have also used energy minimisation to check the stable/unstable character of solutions, identified by the stepwise method. This is done by *jiggling* the candidate structure: i.e. subjecting the structure to small random perturbations and then applying the steepest descent algorithm to see if it relaxes back to the initial configuration or evolves to a new arrangement.

5.3 Numerical results

We now present results for a variety of low energy and low compression structures. Many more structures of equilibrium can be found at higher energy and higher compression (which we hint at in Fig 5.5). Some of these have a more complicated shape, but may be of limited physical significance. We therefore do not discuss them throughout this chapter.

5.3.1 Typical profiles

For low compressions our search yields only one structure that we will refer to as the *symmetric* structure S, since the profile for F_n (or displacement r_n) is symmetric around the midpoint of the system. (Note that we have defined F_n and r_n to be positive.) Fig 5.4 presents the profile of such a structure for $N = 20$ for a low (green triangles) and high (blue stars) compression where we show the displacement r_n from the central axis vs the (dimensionless) position x_n, defined as

$$x_n \;=\; 1/2 \;+\; \sum_{i=2}^{n} \cos(\theta_i)\,. \tag{5.10}$$

These results show perfect agreement with the symmetric structure generated by energy minimisation and extrapolated to the hard sphere limit. The structures obtained by energy minimisation are confined to stable cases.

For high compressions additional asymmetric structures are obtained from the stepwise method. An example for the displacement profile of such a structure is given by the red crosses in Fig 5.4.

5.3.2 Bifurcation diagrams

We have used the iterative stepwise method to search for structures in the range of the compressive forces between $0.19 \leq G_0 \leq 0.25$ and initial forces between $0 < F_1 < 0.01$. These structures correspond to relative compression

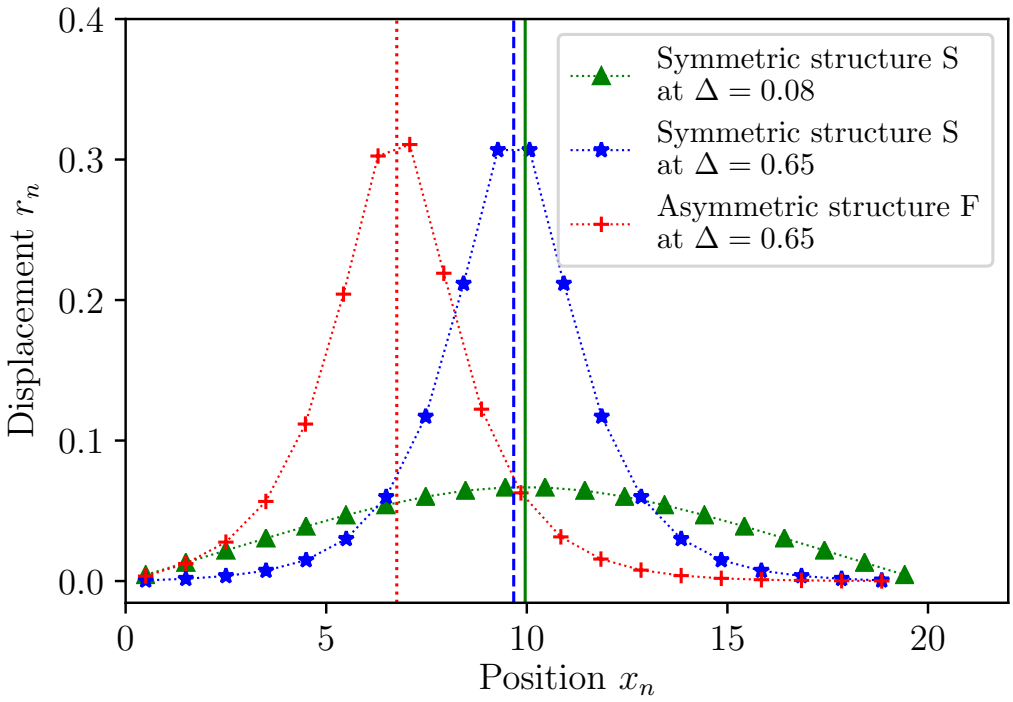

Fig 5.4: Sphere displacements r_n as function of position x_n for a symmetric (blue stars) and a stable asymmetric structure (red crosses) at a compression of $\Delta = 0.65$. Also shown is the displacement r_n for the symmetric structure at a lower compression of $\Delta = 0.08$ (green triangles). (All quantities are dimensionless, see definitions in main text.) The peak position of the asymmetric structure for $\Delta = 0.65$, estimated by a quadratic fit of the displacements around the maximum, is displayed by the vertical dotted red line. The vertical blue dashed and the green solid line display the midpoint of the system. The distance between x_0 and x_N is equal to $N - \Delta - 1$.

below $\Delta < 0.9$. They were computed for both an even ($N = 20$) and an odd ($N = 19$) number of spheres, for which the results differ qualitatively.

Bifurcation diagrams for both cases in terms of the two simulation parameters G_0 and F_1 are presented in Fig 5.5(a) [$N = 20$] and (b) [$N = 19$]. Each dotted line represents a structure computed by the stepwise method at a given G_0 and yielding a certain F_1. At a high G_0 only the symmetric structure S (red line) is observed, which cannot be resolved below $G_0 < 0.21$ anymore using our current implementation of the stepwise method (see discussion in section

5.2.2). Asymmetric structures start to appear above and below S induced by bifurcations with decreasing G_0. Structures below the red curve can be converted into those above the red curve by mirroring the structure at the midpoint of the system.

These two mesmerising bifurcation diagrams give an overview over the range of structures that can be computed with the stepwise method. However, they do not comprehensibly convey the information. Thus, we studied these structures in form of energy diagrams that focus on low energy structures.

In the given parameter ranges the total energy E_{Symm} of the symmetric structure S increases from 0 to roughly 0.15, whereas the difference between the energies of alternative structures is only of order 10^{-4}. We therefore computed the energy

$$\Delta E = E - E_{\mathrm{Symm}} \tag{5.11}$$

relative to that of the symmetric structure at the same compressive force G_0 and plotted them against their compression for even (Fig 5.6(a)) and odd case (Fig 5.6(b)). These two plots only depict the energies for low energy structures.

We present these relative energies in the vicinity of the compression range where the first asymmetric structures are created by bifurcation. While both cases of even and odd N feature an increasing number of bifurcations as compression is increased, they are qualitatively different and will thus be discussed separately.

For the even case $N = 20$ an increasing number of asymmetric structures (A-F) are introduced by bifurcation as compression increases. The unstable structures are marked with an asterisk. The first two additional branches A* and B emerge from an "out-of-the-blue" bifurcation at $\Delta = 0.558$ without any preceding structure. Of these two branches, structures on branch B are stable, whereas structures from A* are unstable, as verified by energy minimisation.

Two further structures C* and D, appear via a pitch-fork bifurcation out

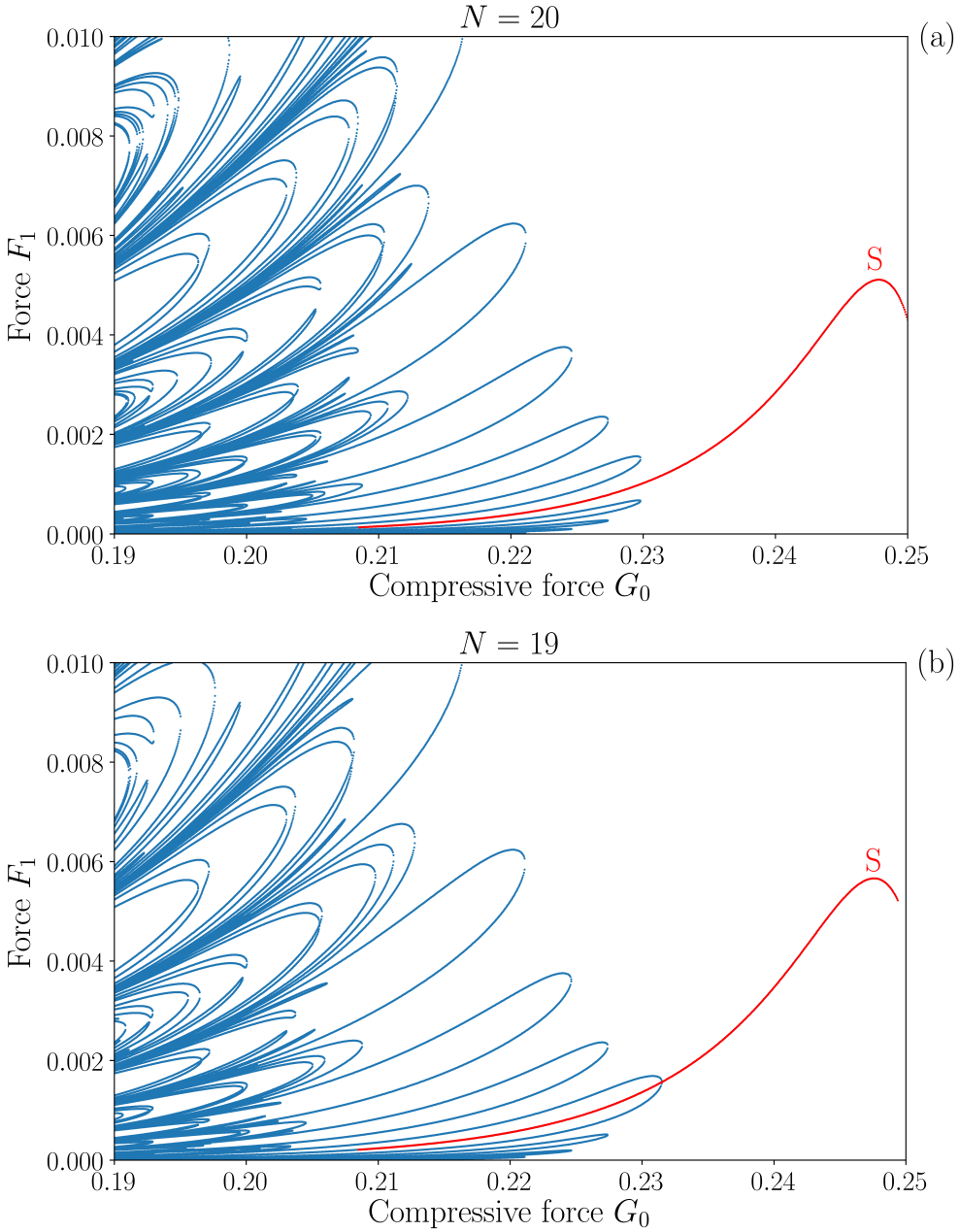

Fig 5.5: Bifurcation diagrams in their simulation parameters: The force F_1 of the first sphere from the stepwise method is plotted vs the compressive force G_0 for $N = 20$ (a) and $N = 19$ (b). Each dotted line corresponds to a particular structure, where the red line represents the symmetric structure S (not resolved below $G_0 < 0.21$; see text for explanation). Asymmetric structures (blue lines) below the red curve can be transformed into those above by mirroring the structure at the midpoint of the system.

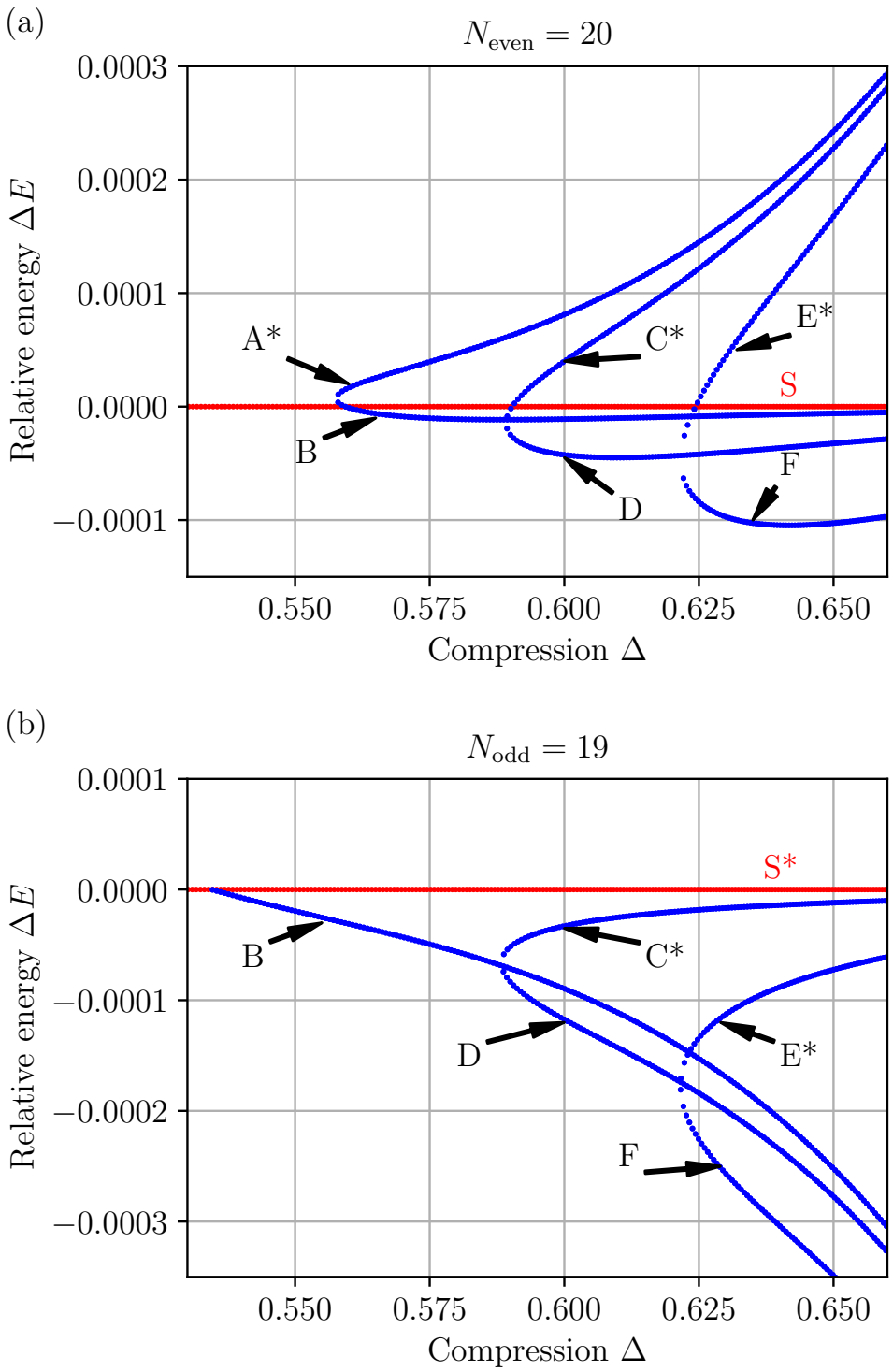

Fig 5.6: Energy bifurcation diagram: Relative energies $\Delta E = E - E_{\text{Symm}}$ (where E_{Symm} is the energy of the symmetric structure S), are plotted against compression Δ around the first bifurcation for the case of even number of spheres (a) and odd number of spheres (b). Unstable structures are marked with an asterisk. Examples of all structures in the even case are displayed in Fig 5.7.

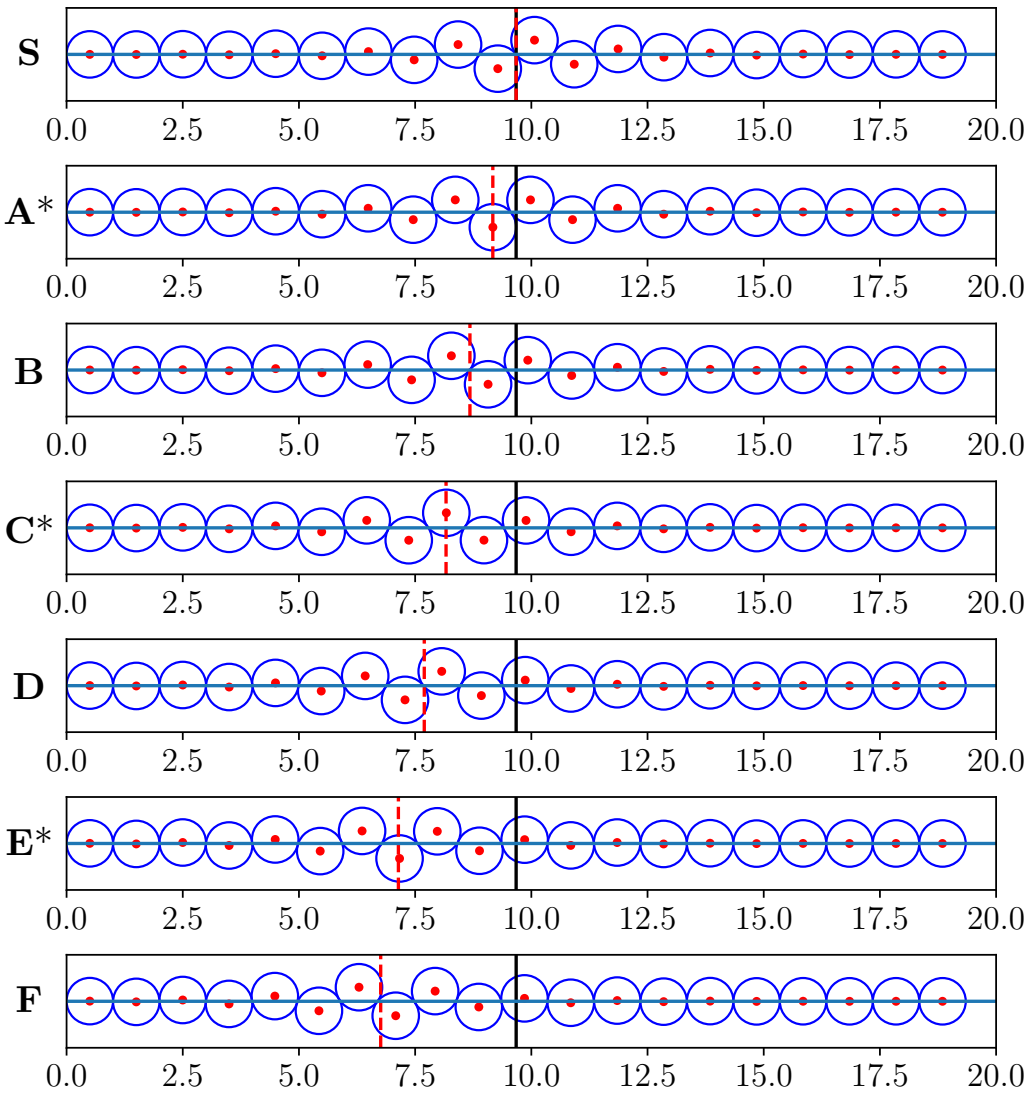

Fig 5.7: Examples of buckled chain structures from the S and A–F branches, as labelled in Fig 5.6. The structures were created by the stepwise method with $N = 20$ spheres at a compression of $\Delta = 0.65$. Structures marked by an asterisk are unstable. The solid black vertical line marks the centre of the system, while the dashed red vertical line marks the peak position of the position profile. Asymmetric structures (A-F) are doubly degenerate (i.e. can have a peak on the left or on the right of the centre).

of the previous stable structure B at $\Delta = 0.588$. B and the additional branch of lower energy D are stable, whereas the upper one C* is not. A similar pitch-fork bifurcation of the D branch occurs for the next two structures at

$\Delta = 0.622$, from which the lower branch F is again stable and E* unstable.

Examples of structures from all of the seven branches for the even case in Fig 5.6(a) are given in Fig 5.7. The vertical black solid line in these plots represents the centre of the structure; the vertical red dashed line indicates the peak position of the sphere profile, as estimated by a quadratic fit to the sphere positions around the maximum. For unstable structures the peak position coincides roughly with the centre position of a sphere. Note the degeneracy: asymmetric structures may have the peak left or right of the centre (see also bifurcation diagrams of Fig 5.5).

The energy diagram for the odd case of 19 spheres (in Fig 5.6(b)) differs with respect to the first bifurcation. Here only a single new stable structure (branch B) emerges. From then on bifurcations follow the pattern of the even case, in which previous structures remain stable and new structures of lower energy are stable (i.e. D and F are stable, while C* and E* are unstable).

While the structures that we have identified here appear to be the only equilibria within the specified range in energy and compression, structures with a more complicated profile occur at higher energy, which we have not addressed here. The displacement profiles of these structures can contain two or more off-centred peaks.

5.3.3 Maximum angles

We have also computed the maximum angle $\theta_{\max}$ of the symmetric structure with varying compression for the stepwise method and energy minimisation, see Fig 5.8. This is a quantity that can readily be extracted from experimental data, see section 5.5.

While our results for the stepwise method stop at a compression of 0.9, the maximum angle $\theta_{\max}$ from the energy minimisation was computed up to a compression of $\Delta \lesssim 1.3$. At this point the modulated zigzag structure acquires an additional contact with the next-nearest neighbour sphere.

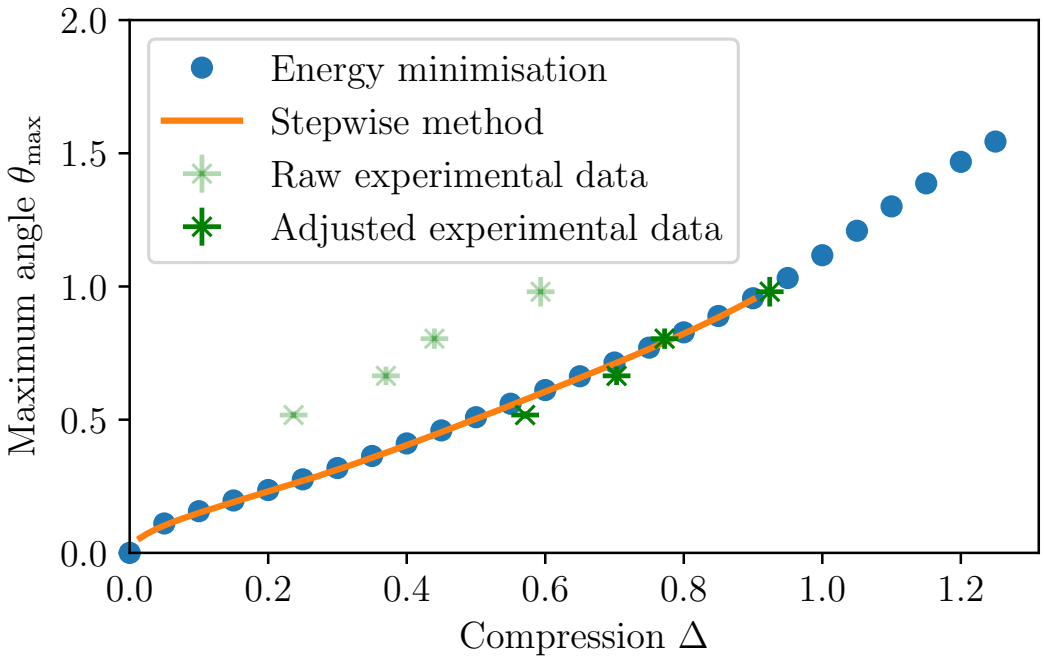

Fig 5.8: Maximum angle $\theta_{\max}$ of the symmetric structure as a function of compression Δ for an even number of spheres N. Blue circles and orange solid line are obtained from numerical calculations (stepwise method and energy minimisation). The green crosses with low opacity refer to the raw experimental data points. For the green crosses with high opacity, the increased effective sphere diameter attributed to vibrations in the system was taken into account in the compression calculation. The uncertainty in the $\theta_{\max}$ was obtained by averaging the angles over five images of the structure at same compression.

At low compressions ($\Delta \lessapprox 0.1$) the displacement profile is of the parabolic shape shown by the green triangles in Fig 5.4. For higher compressions the profile changes to a hyperbolic shape as described by the blue stars in Fig 5.4.

5.4 Linear approximation

In order to better understand the previous numerical results, we have developed an approximate, linear analytic description as follows. For small angles

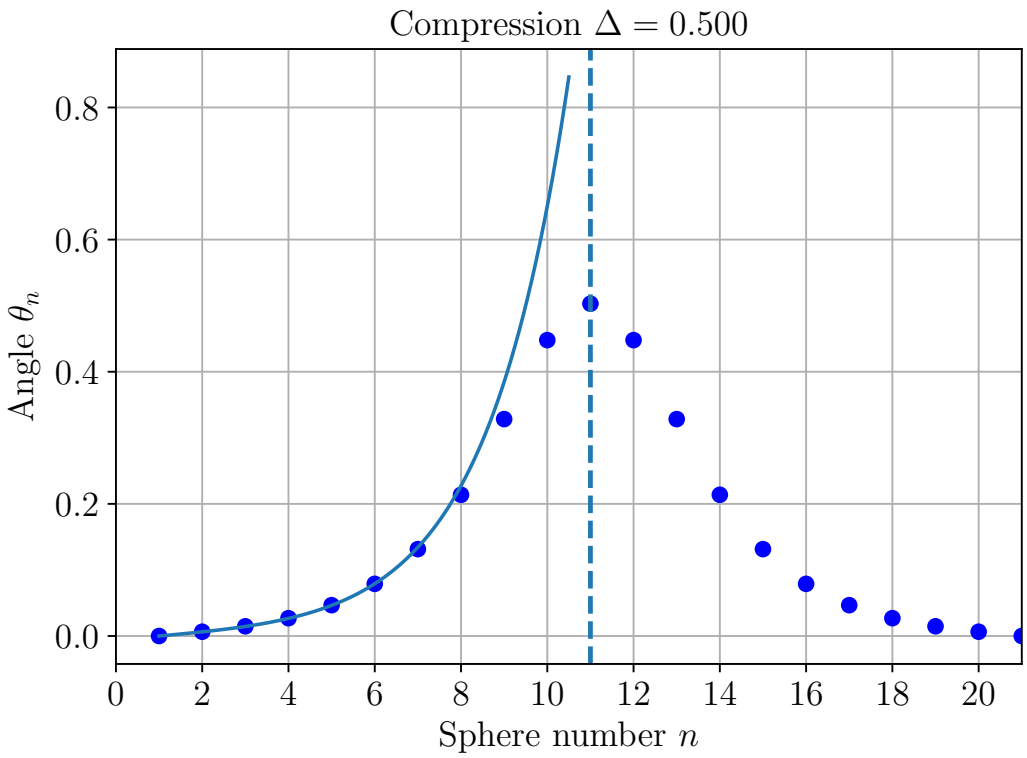

Fig 5.9: Variation of angle θ_n with sphere number n as obtained from the exact stepwise method of (blue dots) and from the linearised theory (5.25) (blue solid line) (for $N = 20$) at a compression of $\Delta = 0.500$. Note that there are 21 angles, since θ_{N+1} is associated with the wall contact of sphere N.

θ_n and forces F_n, linearisation of eq. (5.6) leads to

$$\begin{pmatrix} F_n \\ \theta_n \end{pmatrix} = \begin{pmatrix} \frac{1}{G_0} - 1 & -1 \\ \frac{1}{G_0} & -1 \end{pmatrix} \begin{pmatrix} F_{n-1} \\ \theta_{n-1} \end{pmatrix} . \tag{5.12}$$

Recursive substitution of F_n and θ_n and setting $\frac{1}{G_0} = 4 + \epsilon$ for small and positive ϵ, results in

$$\begin{pmatrix} F_n \\ \theta_n \end{pmatrix} = \underbrace{\begin{pmatrix} 3+\epsilon & -1 \\ 4+\epsilon & -1 \end{pmatrix}}_{\underline{\underline{M}}}^{n-1} \begin{pmatrix} F_1 \\ \theta_1 \end{pmatrix} . \tag{5.13}$$

The largest possible value for the compressive force is $G_0 = 1/4$. For the case of an infinitely long chain, it can be derived from the *uniform zigzag* structure

($r_n = -r_{n-1}$, $F_n = F_{n-1}$, and $\theta_n = \theta_{n-1}$). Equations (5.4) and (5.5) for this structure give

$$2F_n = \sin(\theta_n) \tag{5.14}$$

$$F_n = 2G_n \sin(\theta_n)\,. \tag{5.15}$$

By substituting the latter equation into the former, $G_n = 1/4$ can be calculated. Equation 5.3 dictates that this is the largest value G_0 can obtain.

A solution for $(F_n, \theta_n)^{\mathrm{T}}$ may be expressed in terms of eigenvalues $\lambda_{1,2}$ and eigenvectors $\boldsymbol{V}_{1,2}$ of the matrix $\underline{\underline{M}}$ as

$$(F_n, \theta_n)^{\mathrm{T}} = a\lambda_1^{n-1}\boldsymbol{V}_1 + b\lambda_2^{n-1}\boldsymbol{V}_2\,. \tag{5.16}$$

The eigenvalues are

$$\lambda_{1,2} = 1 + \frac{\epsilon}{2} + \sqrt{\epsilon^2 + 4\epsilon}\,, \tag{5.17}$$

which to lowest order in ϵ gives

$$\lambda_{1,2} \approx 1 \pm \sqrt{\epsilon}\,. \tag{5.18}$$

Its $(n-1)$th power can be approximated in the following way

$$\lambda_{1,2}^{n-1} = \mathrm{e}^{\ln(1\pm\sqrt{\epsilon})^{n-1}} \tag{5.19}$$

$$\approx \mathrm{e}^{\pm\sqrt{\epsilon}(n-1)}\,. \tag{5.20}$$

The corresponding eigenvectors are

$$\boldsymbol{V}_{1,2} = \left(\frac{1}{2}\left(1 \pm \frac{\sqrt{\epsilon}}{2}\right), 1\right)^{\mathrm{T}}\,. \tag{5.21}$$

The prefactors a and b are obtained from the initial conditions F_1 and θ_1. The solution in the linearised approximation for $\theta_1 = 0$ is then given by

$$F_n = \frac{2F_1}{\sqrt{\epsilon}}\sinh(\sqrt{\epsilon}(n-1)) + F_1\cosh(\sqrt{\epsilon}(n-1)) \tag{5.22}$$

$$\theta_n = \frac{4F_1}{\sqrt{\epsilon}}\sinh(\sqrt{\epsilon}(n-1))\,. \tag{5.23}$$

The forces F_n can be written in a more concise form as

$$F_n = \frac{F_1}{\sinh(\phi)} \sinh(\sqrt{\epsilon}(n-1) + \phi) \tag{5.24}$$

$$\theta_n = \frac{4F_1}{\sqrt{\epsilon}} \sinh(\sqrt{\epsilon}(n-1)) \,, \tag{5.25}$$

with the offset in the forces $\phi = \operatorname{arctanh}(\sqrt{\epsilon}/2)$. Note that θ_n does not have an offset, since $\theta_1 = 0$.

A comparison of angles θ_n using the approximated linearised equation (5.25) and the previously numerical exact stepwise method is shown in Fig 5.9 for a compressive force of $G_0 = 0.234$, resulting in a compression of $\Delta = 0.500$. The starting value F_1 in the linearised scheme was taken from the corresponding value in the stepwise method.

We find excellent agreement between the linearised theory and the stepwise method up to about $n = 8$. The linear theory produces a monotonically increasing function (Fig 5.9), whereas the accurate solution "rolls over" and decreases towards the second boundary. The cause for this can be found in the non-linearity of the equation for the stepwise-method.

5.5 Comparison with experiment

Our experimental procedure is similar to that of Lee *et al.* [8]. We placed an even number of $N = 34$ polypropylene beads of density $\rho = 0.900\,\mathrm{g/cm^3}$ and diameter $d = 3.000 \pm 0.001\,\mathrm{mm}$ [111] in a cylindrical tube (I.D. $15.91 \pm 0.01\,\mathrm{mm}$; O.D. $20.17 \pm 0.01\,\mathrm{mm}$; length $130.55 \pm 0.01\,\mathrm{mm}$) filled with water (density $\rho_\mathrm{w} = 1\,\mathrm{g/cm^3}$).

The tube is sealed on both ends with stoppers, making sure that no air bubbles remain within the system. The extent to which the stoppers intrude into the tube can be varied, allowing us to adjust the compression Δ.

The tube is then mounted onto a commercial lathe (Charnwood W824), for which we set the rotation frequency to $\omega = 1800 \pm 50\,\mathrm{rpm}$. In order to

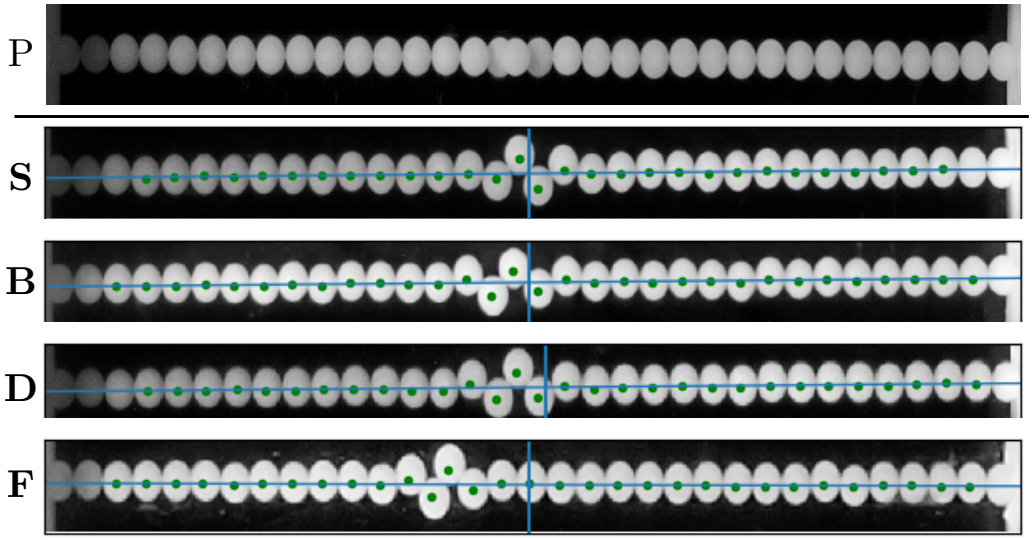

Fig 5.10: Photographs of a variety of buckled structures for $N = 34$, obtained by the rapid rotation of a water-filled tube containing polypropylene beads (density of $\rho = 0.900\,\mathrm{g/cm^3}$), using a lathe. The structure P above the solid line is an image of a modulated zigzag structure rotated by $\pi/2$ compared to the other structures. It indicates the planarity of the experimental structures. The structures S, B, D, and F are labelled as in Fig 5.6. The vertical line represents the centre of the system and the horizontal line the central axis of rotation.

record the structures we used a stroboscopic lamp, whose frequency is matched to that of the lathe. A slight off-set between both frequencies is used so that recorded structures appear to be slowly rotating (see example in supplemental video of Ref [6]).

The image labelled with P above the solid line in Fig 5.10 is an in-plane view of one of the modulated zigzag structures. The buckling is observable close to the centre of the structure where the spheres seem to overlap in horizontal direction. In vertical direction, all spheres are arranged in a line. It demonstrates the assumption of planarity, on which all the structures created by the stepwise method are based on.

Fig 5.10 below the solid line shows images of the structures that we identified with the branches S, B, D, and F by comparing them with to the numerical

results from 5.7. The experimental structures can be identified by the distance of the peak position to the structure centre. This is independent of N for large number of spheres because the wall effects can be neglected. The identified structures correspond to all the stable structures of Fig 5.6. Structure S, as well as structure B, are at a compression of $\Delta = 0.44 \pm 0.02$, while the compressions for structure D was $\Delta = 0.59 \pm 0.02$ and for F, $\Delta = 0.68 \pm 0.02$.

However, in order to reconcile these experimental results with the theoretical predictions of previous sections, it is necessary to introduce an *effective* diameter for the spheres, about 1 % greater than the true value. This increases the effective compressions by a constant shift of roughly 0.35. We attribute it to the effects of vibration of the lathe, and will explore strategies for its mitigation in future work. This shift also features in previous results from Lee *et al.* [8] and can be observed by comparing simulations and experiments in chapter 4.2 [4].

We extracted the maximum angle $\theta_{\max}$ for the symmetric structure with varying compression for the experiments (see Fig 5.8). It shows very clearly the necessity for the adjustment of sphere diameter. Due to the neglected wall effects, these results only depend on N being odd or even for a large enough number of spheres.

5.6 Conclusions

The compressed and confined sphere chain presents a variety of fascinating observations, previously described in terms of "kinks" or "solitons" [103]. We have succeeded in exploring many of its properties, using simple experimental apparatus and theoretical methods.

We hope that our results will find direct comparison with previous work, particularly with regards to ions confined in optical traps [98–105, 107]. This work should also be relevant to other systems in which buckling is a key fea-

ture: for example localised buckling has recently been observed in experiments involving an expanding (growing) elastic beam pinned to a substrate [112].

While we have investigated only simple structures with single peaks in the displacement profile so far, more complicated structures exist at higher energies. We hinted at their existence in the bifurcation diagram of Fig 5.5. Among these are structures that are created by concatenating one of the single-peak structures with its mirrored counterpart. Their compression and energy will roughly be doubled.

In our experiments we demonstrated the existence of all the stable structures with even number of spheres found in our numerical results. We only did a direct comparison between experiments and numerical results for the symmetric structure with even number of spheres where we compared the maximum angle $\theta_{\max}$. This comparison may be extended in the future to the whole spectrum of parameter values. The rotational energy of each experimental structure (S, B, D, and F) can be calculated from the extracted sphere positions for various compressions as well as different number of spheres.

Considerable current interest in the compressed sphere chain focusses on motion of the single peak and the corresponding Peierls–Nabarro potential. This is the potential needed to move the single peak position, i.e. transform one stable structure to another (e.g. from structure B to S in Fig 5.7). It may be estimated by making a smooth interpolation of the energy values for stable and unstable states as calculated here. Fig 5.11 shows an illustration of such a potential. Further experimental investigations towards this potential can possibly be undertaken in future work.

Recently we have found a yet simpler experimental method which should be useful, at least for purposes of demonstration. It consists of a horizontal tube into which ball bearings are introduced. Slight agitation enables them to settle in modulated zigzag structures similar to those depicted in this chapter.

A further variation, which appears to be promising, uses bubbles in a

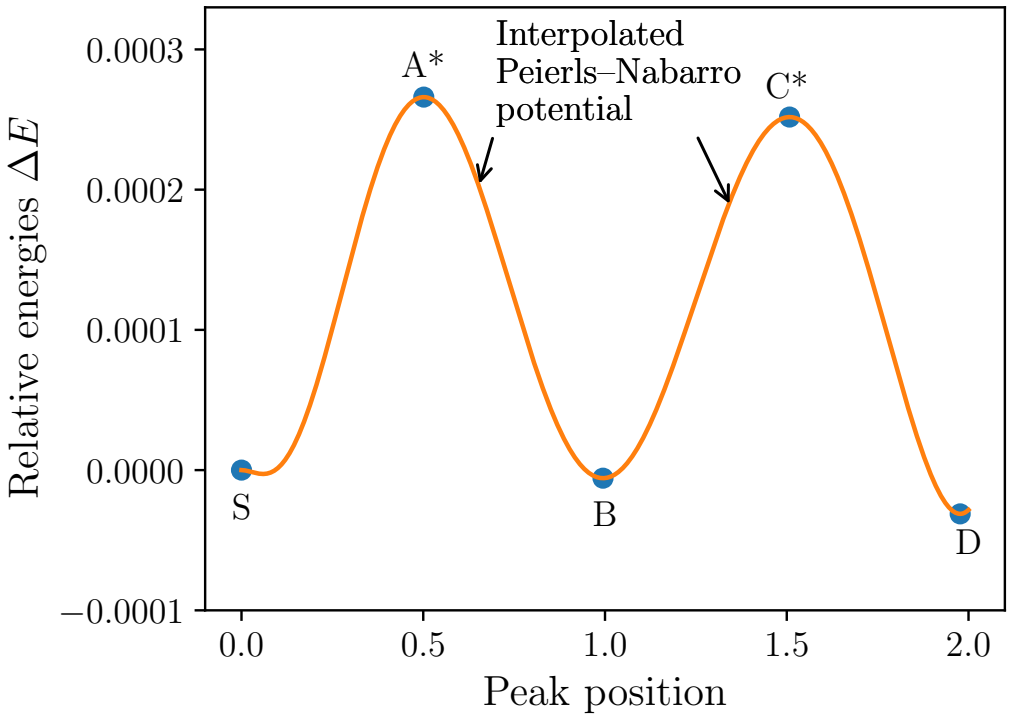

Fig 5.11: Illustration of the Peierls–Nabarro potential. The blue dots are the relative energies ΔE vs the peak position for structures S, A*, B, C*, and D from Fig 5.7. The solid line is a smooth interpolation through the dots for the stable and unstable structures. Note that the stable structures (S, B, D) are at the minima of the interpolation and unstable structures (A*, C*) are at the maxima.

horizontal liquid-filled tube. The bubbles are pushed towards the curved tube wall by buoyancy where they are confined by a potential that in first approximation is quadratic. The bubbles form a modulated zigzag structure when being compressed.

Other extensions of this experimental method include the case of soft (elastic) spheres, for which we have already observed similar effects, using hydrogel particles and bubbles. Also the observations can be extended to much higher compression, making contact with the work discussed in chapter 4, for the 3d structures generated. It may also be possible to take advantage of a technique that uses photoelastic material to indicate the magnitude of

the compressive forces [113, 114]. Some of these future experimental methods will be covered in more detail in the outlook of chapter 6.

Chapter 6

Summary and outlook

In this thesis, we have greatly extended the research field on columnar structures. In particularly we have advanced the research towards structures of soft and deformable objects. Some of our investigations have opened new possible experimental and theoretical investigations which will hopefully be examined in future work. These additional experimental and theoretical investigations will be the subject of this chapter.

We first summarise the key results of this thesis, as presented in the previous chapters 3–5. This is followed by an outline of possible future work for simulation and experiments related to each chapter. Such future work can further extend our results in the direction for possible applications in the area of botany, foams, or nanoscience, as explained in the Introduction (chapter 1.4).

This thesis has focussed on (columnar) structures of spheres in 3D, but packing problems of similar type can also be studied by packing disks inside a 2D channel. In the second part of the outlook we describe the 2D counterpart of columnar structures in detail, how they can be studied using soft disks, and how they results may apply to research in microfluidics or the packing of people.

While the soft sphere model, extensively used throughout this thesis, has

shown its great advantages, it also has limits in describing soft matter systems such as foams. These limits are highlighted in the third part of this chapter by comparing results of soft disk system to that of 2D foam simulations. In the last part, we describe a model, based on the theory of Morse and Witten, that may be used in the future for similar investigations as carried out in this thesis.

6.1 Soft sphere packings in cylinders

6.1.1 Summary

Chapter 3 focussed on columnar structures that are assembled by packing soft spheres inside a cylinder. The results of this chapter are built on the previous findings of hard sphere packings.

We reported on the simulation and experimental observation of a *line-slip* structure in such packings. The experimental observation was made on a column of bubbles under forced drainage, clearly exhibiting the expected line slip. Our simulations concerned columnar structures of minimal enthalpy using the soft sphere model. We presented a phase diagram of all stable (i.e. minimal enthalpy) structures up to the diameter ratio $D/d = 2.71486$, where the nature of the densest sphere packing changes.

However, macroscopic systems of this kind are not confined to the ideal equilibrium states of this diagram. Consequently, we explored the structural transitions to be expected as experimental conditions are varied by carrying out further simulations; these are in general hysteretic. We investigated an example of a reversible transition in closer detail and represented the results in a stability diagram. In a directed network we then displayed all permissible structural transitions of densest packings from the phase diagram.

6.1.2 Outlook: An exhaustive hysteresis investigation

In future work, our soft sphere simulations based on enthalpy minimisation can be used for an exhaustive hysteresis and metastability investigation for all possible structural transitions. So far, we have only presented a stability diagram that is representative for all reversible transitions. However, such a diagram will be significantly different for other types of transitions such as the irreversible transition or the re-entrance case (see chapter 3.3.3).

The stability diagrams for these two cases are of particular interest. The irreversible case covers all those transitions where the initial uniform structure U_1 is not recovered when reverting the control parameter (e.g. diameter ratio D/d or pressure p). For example, the $(4, 2, 2)$ uniform structure transforms into the $(5, 3, 2)$ uniform structure upon increasing D/d, but for the reverse trajectory, the $(5, 3, 2)$ follows a transition into the $(4, 3, 1)$ uniform structure (see also Fig 3.10 in chapter 3.3.3). Thus, a stability diagram for the irreversible case will involve three different uniform structures, of which two exist at the same value of the control parameter. In the case of the given example, the $(4, 2, 2)$ and $(4, 3, 1)$ uniform structures can exist at the same pressure or diameter ratio, of which at least one of them is metastable.

We also expect the irreversible case to be described with two stability diagrams that slightly differ from each other. They will depend on whether the prohibited transition occurs on increasing or decreasing the control parameter. In the previously mentioned example the prohibited transition is the $(5, 3, 2) \Rightarrow (4, 2, 2)$ transition, which requires a decrease in D/d or p. However, in another example the $(3, 2, 1) \Rightarrow (3, 3, 0)$ is also prohibited, but requires an increase in the control parameter. Thus the borders, demarcating the directions of the transitions, will differ in those stability diagrams.

The re-entrance case is worth studying in more detail because its line slip in-between has interesting properties in the hard sphere limit. As explained

in chapter 3.3.3, two different packings of the same line slip can exist at the same D/d, since its packing fraction as a function of D/d is curved backwards (cf. Fig A.1 in the Appendix A.1). Hence, studying the enthalpy curves for this particular line slip may introduce new interesting features.

Such metastability and hysteresis investigations for structural transitions may also be extended to structures with diameter ratios above $D/d > 2.71486$, as simulated by Fu *et al.* [65] (see also chapter 2.4). The nature of the structures in this regime differ significantly to those discussed in this thesis, since structures with internal spheres that are not in contact with the cylinder wall occur. Structural transitions for these packings may also be summarised in stability diagrams, which may significantly differ from all previous diagrams. It is also of interest how columnar structures with internal spheres are related to those without internal spheres. This can be investigated by extending the directed network of Fig 3.10 to higher values of D/d.

Additionally, Pittet *et al.*'s work on structural transitions in cylindrical dry foam [37] may be extended to wet foam structures in the future. Three different methods are possible in those experiments to change the control parameter of either D/d or pressure p. The general experimental set-up is described in the introduction of chapter 1.4.2.

In the first method the diameter ratio of the experiment is varied. The bubble size (and therefore D/d) can be controlled by the gas flow rate q_0 that is used to produce the bubbles (see Fig 1.7 in chapter 1.4.2). Thus, a wet foam structure in such experiments can be forced into a transition by changing the gas flow rate. However, the soap bubbles inside the foam column are not necessarily monodisperse in this method.

It may be more convenient to vary the pressure p. This was previously done by Boltenhagen *et al.* [38] using a piston for dry foam structures. The foam columns were observed to undergo different transitions, when compressed or dilated in this way. Similar experiments may be performed for wet foam

structures in forced drainage experiments.

One can also set up an experiment that uses the natural variation of pressure within the foam column due to gravity. Such an experiment can be performed by simply filling a long tube with soap bubbles. The liquid of the foam at the top will push down onto the bubbles below, causing a variation of pressure with height. Thus, structures along the column will also vary with height and structural transitions can easily be identified.

Results of such experiments may then be fruitfully compared to our simulations. Observed structural transitions may directly be compared to the directed network of Fig 3.10. But also schematic stability diagrams like that of Fig 3.9(b) can be used as a guide to experimentally assemble such foam structures.

Using a completely different experimental procedure, structural transitions may also be investigated by inducing a shear stress to the system. In these experiments the top and bottom bubbles of the foam structure are rotated/sheared against each other around the vertical axis. This may induce a structural transition, especially from a chiral to a achiral structure (or vice versa). Corresponding simulations may also be performed by using the soft sphere model.

6.2 Rotational columnar structures of soft spheres

6.2.1 Summary

In chapter 4 we analysed a novel method to assemble columnar structures involving rapid rotations around a central axis. Lee *et al.* [8] used this method to drive spheres of lower density than the surrounding fluid towards the central axis. This resulted in different columnar structures as the number of spheres

was varied.

We presented comprehensive *analytic* energy calculations for such structures, based on the soft sphere model, from which we obtained a phase diagram (cf Fig 4.6). It displayed interesting features, including *peritectoid* points, at which the achiral $(3, 3, 0)$ and $(4, 4, 0)$ uniform structures vanish.

These analytic calculations were complemented by computationally cheap numerical simulations for finite-sample sizes with soft spheres. These, in parts, corroborate the analytic calculation. However, they also revealed the appearance of a line-slip structure due to finite-size effects.

6.2.2 Outlook: Further investigations of finite-size effects

Our research on this assembly method opens up a variety of possible experiments and finite-size simulations. We only report on the appearance of one particular line-slip structure in our finite-size simulations. However, similar unexpected structures might play a role in other parts of the phase diagram of Fig 4.6. The rigorous exploration of such structures can be part of future investigations using the finite-size simulations, explained in chapter 4.3.1.

We also left out a rigorous analysis of the asymptotic trend as the number of spheres N in the simulation goes to infinity. Our preliminary results for the discovered line slip indicate that the binary mixture is recovered, when N is increased. The total energy in terms of N can be studied in more detail for the binary mixture and the line slip. The crossover point in the energy for those two structures will indicate how many spheres are needed to recover the limit of an infinite system size. Similar investigations can be performed for other unexpected (line-slip) structures in the future.

In order to get a closer comparison between simulations and the actual lathe experiments, the finite-size simulation can be modified by adding walls

at both ends of the unit cell. Wall effects are then introduced to the simulation and further unexpected structure, not predicted by the phase diagram, may appear. It can be examined if such wall and finite-size effects vanish with an increasing number of spheres. Investigations of such modified simulations can give a hint on what system sizes in experiments are needed to recover the limit of infinite system size.

Since these finite-size effects in the form of line slips are also expected for hard spheres, future experiments using polymeric beads (as performed by Lee *et al.*) can be performed to search for these unexpected structures experimentally. Results may be compared to finite-size simulations that are implemented with wall boundaries at each end of the unit cell. For closer comparison, hysteresis and metastability should be looked for in experiments and simulations.

In order to corroborate findings from soft sphere simulations, especially the occurrence of peritectoid points, Lee *et al.*'s type of experiments can also be performed using soap bubbles immersed in a rotating tube filled with surfactant solution. However, the bubbles in these experiments are prone to coarsening and (thus) changing bubble size during the course of the experiment.

An alternative experimental realisation of soft spheres are hydrogel spheres (Fig 6.1(a)). Hydrogel spheres consist of hydrophilic polymer networks that, when in contact with water, swell up to diameters of roughly $d \approx 1\,\mathrm{cm}$ (see scale in Fig 6.1(a)). They can simply be produced by placing colloidal particles made of such polymers in water. The hydrogel spheres, after absorbing the water, are then elastic and deformable (like soft spheres). Their density is slightly higher than that of water. Thus, either salt has to be added to the surrounding water or a different type of liquid has to be used.

We have already performed preliminary lathe experiments using such hydrogel spheres (see Fig 6.1(b)). In these experiments we placed the hydrogel

(a) (b)

Fig 6.1: Possible future experiments about rotational columnar structures of soft sphere may be performed with hydrogel spheres. (a) shows an image of such hydrogel spheres. (b) is an image of a $(4, 2, 2)$ structures assembled of hydrogel spheres involving rapid rotations with a lathe.

spheres in a glycerol solution, which has a significantly higher density than the hydrogel spheres. Rotating the system leads to various types of structures, such as the $(4, 2, 2)$ structures displayed in Fig 6.1(b).

However, two major technical difficulties arise in such lathe experiments that are yet to be overcome. As it can be seen from Fig 6.1(a), the hydrogel spheres are slightly polydisperse (not of equal size) because each sphere absorbs a different amount of water.

The second problem is related to a density change of the spheres over the course of the experiment. During the experiments, the spheres absorb the glycerol solution that they are placed in. Thus, the density of each sphere increases with time, depending on the amount of glycerol absorbed. Both issues make these such experiments using hydrogel spheres impractical for columnar structure investigations of soft spheres. By filtering the hydrogel spheres by size and sealing them against the surrounding liquid, these complications might be overcome in the future.

6.3 Hard sphere chains in a cylindrical harmonic potential

6.3.1 Summary

The simplest possible columnar structure consists of a chain of spheres that are assembled in a line. Such a structure, confined by a radial harmonic potential, with hard walls at its ends, exhibits a variety of buckled structures as it is compressed longitudinally. Such structures have previously been experimentally investigated using trapped ion systems.

In chapter 5 we showed that such hard sphere structures may be conveniently observed with Lee *et al.*'s experimental method of polymeric spheres inside a rotating liquid-filled tube [8]. We developed a corresponding theoretical model, based on a stepwise method, that is transparent and easily investigated numerically, as well as by analytic linear approximations.

Hence we explored a wide range of predicted structures occurring via bifurcation, of which stable ones were also observed in our experiments using rapid rotation and simulations based on energy minimisation. The structures predicted by our numerical model were presented in an energy bifurcation diagram, displaying the energies vs compressions for low energy structures.

6.3.2 Outlook: Extension of the stepwise method and experiments with confined soap bubble chains

The simulations, such as the stepwise method, as well as the lathe experiments that were described in chapter 5 can be extended in many possible directions. In its current state the stepwise method, used to find force-equilibrium structures, encounters difficulties above a certain compression. Since an increasing number of solutions is found for increasing compression, our implementation based on the bisection method has problems in finding all these solutions. By

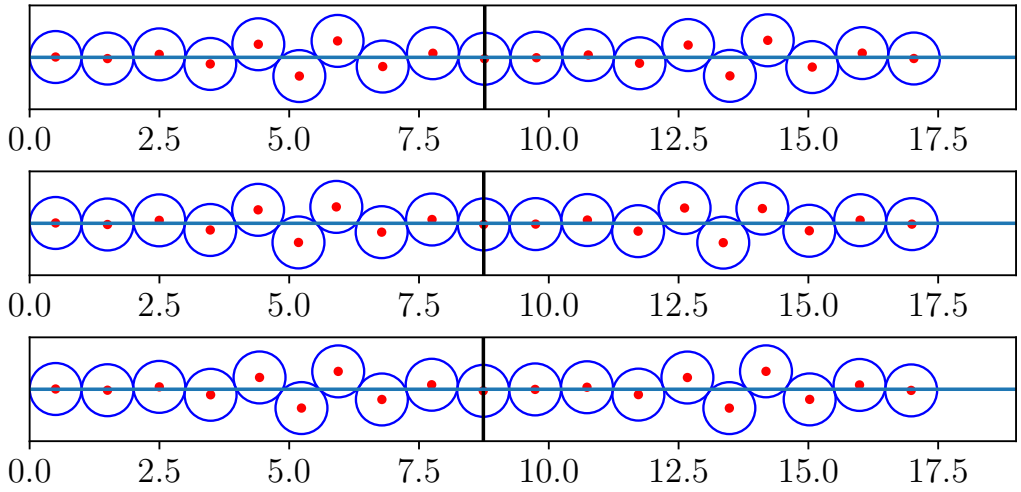

Fig 6.2: Three preliminary examples of high energy structure that have two peaks in their profile. The black vertical line represents the midpoint of the structure and the blue horizontal line is the rotational axis (as introduced in chapter 5). All structures were simulated with the stepwise method.

exchanging the root search method for a more sophisticated one (e.g. Newton–Raphson method), the stepwise method may also be able to cover the regime of higher compressions.

The present implementation, however, can already be used to find structures of higher energies that we did not discuss in chapter 5. We hinted at those structures in the extended bifurcation diagram of 5.5, but intentionally left them out of our analysis in this chapter. They can be found by increasing the search range for the simulation parameter F_1.

While all the profiles of all the energy structures, as described in chapter 5, consist of a single peak, some of these higher energy structures may have two (or even more) peaks in their profile. Some preliminary examples that were already generated with the stepwise method are shown in Fig 6.2. These structures have peaks on either side of the midpoint of the structure. Their second peak increases the rotational energy of the structure to (roughly) double the amount of their single peak counterpart.

Simulations and experiments of such structures can also be extended to

soft spheres. By allowing overlaps in the stepwise method, it may be modified to simulate structures of soft spheres. Results may then directly be compared to further soft sphere simulations based on energy minimisation from chapter 5.2.2.

Future lathe experiments for soft spheres can be carried out using bubbles or hydrogel spheres (see Fig 6.1) instead of polymeric beads. For these constituents the same issues apply concerning the polydispersity and density as described in section 6.2.2. Another fruitful extension of the experiments may be performed by using spheres made of photoelastic material [113, 114]. Such a material indicates the magnitude of each compressive force between the spheres, which might give a closer comparison with the stepwise method.

The most promising future work in this area is an experimental method using monodisperse bubbles confined in a horizontal liquid-filled tube (see Fig 6.3). Buoyancy pushes the bubbles that are aligned as a chain along the axis of the tube, towards the curved tube wall. There they are confined in transversal direction by the tube wall. By compressing the bubble chain in longitudinal direction, the chain starts to buckle and a modulated zigzag structure similar to those described in chapter 5.3 is formed.

A preliminary example of such a modulated zigzag structure, created from a chain of bubbles, is presented in the top image of Fig 6.3. Such a structure can directly be compared to further results from our soft sphere simulation, based on energy minimisation (explained in chapter 5.2.2). The corresponding structure simulated with this method is shown in the bottom image of Fig 6.3.

Such experiments are mainly for demonstrational purposes. However, the softness of the system may introduce some of new unexpected structures and features, not observed in hard sphere systems. A publication on this work is currently in preparation [115].

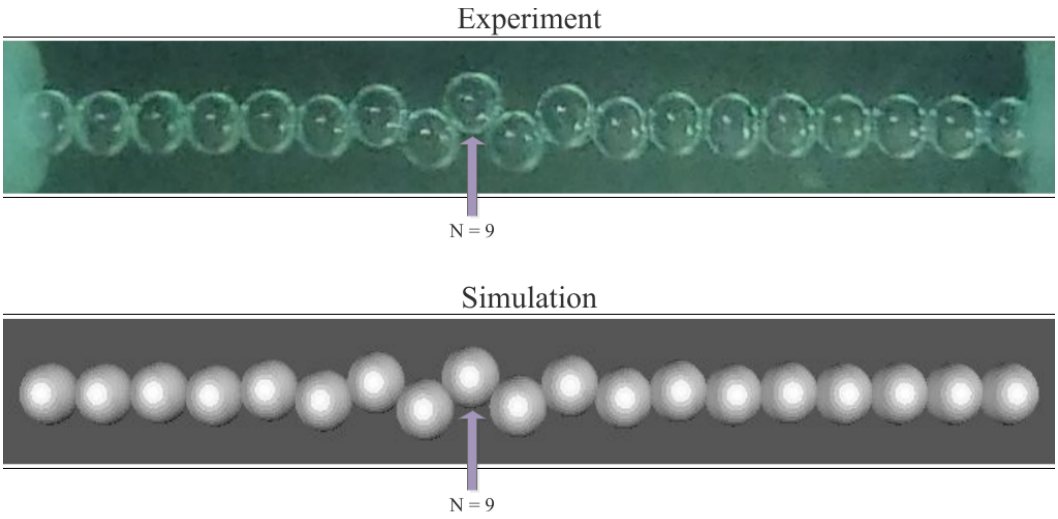

Fig 6.3: Top: A modulated zigzag structure of a chain of 19 soap bubbles inside a tube compressed between two stoppers similar to those in chapter 5. Buoyancy pushes the bubbles against the curved tube wall, which confines the bubbles in transversal direction. Bottom: The same modulated zigzag structure simulated by the soft sphere simulations based on energy minimisation from chapter 5.2.2. The soft spheres are compressed between two walls, distance L apart, and confined inside a cylindrical harmonic potential in radial direction. The images will be published in Ref [115].

6.4 Soft disk packings inside a 2D rectangular channel

Although the packing problem of spheres inside a cylinder can be reduced to packing disks on the cylinder surface, the resulting columnar structures on which we focussed in this thesis are three-dimensional (3D) structures. The 2D counterpart to packing spheres into cylinders, is the packing of disks inside a rectangular channel. This supposedly easier packing problem due to less dimension in the configuration space may bear further insight to sphere/disk packings with a range of interesting applications.

Such 2D packings and their packing fraction have been studied in details for hard spheres [116]. Through a final-year student project, we have started to preliminarily investigate such structures using soft disks. Their disk–disk

interaction is modelled the same as for soft spheres, but in 2D. We discovered that the densest packings of soft disks confined inside a rectangular channel are similar structures as the 3D columnar structures. They either form a hexagonal structure (such as the one in Fig 6.4(a)), which is the 2D counterpart of a uniform structure (explained in chapter 2.3.1), or a structure with loss of contacts between certain disks (see Fig 6.4(b)). This structure is the 2D counterpart of a line-slip arrangement (explained in chapter 2.3.2).

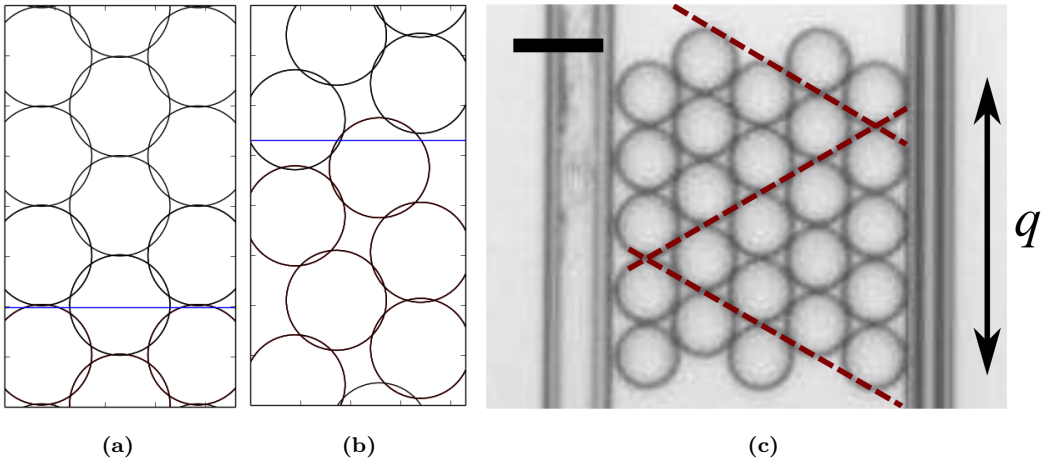

Fig 6.4: Soft disk packings [(a) and (b)] and a 2D bubble raft compressed between two vertical plates (c). (a) shows a hexagonal packing and (b) the 2D counterpart of a line slip. Both are simulated with soft disk simulations. (c) displays an optical microscopy image of a hexagonal crystal of buoyant droplets bounded by two glass plates [117].

There are many quasi-2D systems where the such packings are of great interest. The most obvious one is in microfluidics. This is an emerging multidisciplinary field that is concerned with the behaviour of fluids inside channels with a size on the microscale [36]. It is of incredible use in areas such as diagnostic medicine and microelectronics, where the precise manipulation of small amounts of fluid is important.

One goal of researchers in this field is to precisely control droplets or bubbles in these systems by varying parameters such as the size of their channel or the pressure of their system. Therefore studying the packing behaviour

of such deformable objects using the soft disk model as these parameters are varied is of great interest.

A 2D bubble raft bounded by two plates, such as the one of monodisperse bubbles displayed in Fig 6.4(c), is also used as a model system to study the crystal-to-glass transition [117]. In a study by Ono-dit-Biot *et al.*, 2D finite aggregates of oil droplets were compressed between two plates and their rearrangement under compression examined. By studying aggregates of mono- and polydisperse droplets, it gave insight into the energy landscape from crystals to glasses.

2D packings of soft, deformable objects also occur when people are packed together in a rectangular confinement. We performed very simple and preliminary experiments in this area for a poster project of second-year students (see illustration in Fig 6.5). In these experiments students were packed inside a rectangular confinement, created by tables. The image was then taken from the balcony of the SNIAM building at Trinity College Dublin. Research in this area may improve better designs for public transport and other public places where an agglomerate of people occurs.

Fig 6.5: An illustration of packing of people/students inside a rectangular confinement as an example of soft disk packings. The people displayed in the image "self-assembled" to an ordered zigzag structure. The picture was taken during a student project in front of the SNIAM building at Trinity College Dublin.

6.5 Limits of the soft sphere model

All outlook plans for future simulations up to this point continue our work using simulations that are based on the soft sphere models. However, another interesting direction for researching columnar structures can be followed by questioning the accuracy of the soft sphere model to systems of deformable objects such as foams or emulsions.

In this section we will elaborate on the limit of the soft sphere model. Since these limits are easier to investigate in two-dimensional (2D) systems, we will focus here on soft disks, rather than the soft spheres. Similar discrepancies are to be expected for 3D, as well.

Besides the simple discrepancy of lack of volume conservation, significant differences in the variation of the average contact number Z with packing fraction were discovered between the random soft disk model and 2D random foam simulations. We will briefly highlight these differences in the following.

A detailed discussion on the discrepancies can be found in Ref [1]. This is part of additional work during my PhD where I co-authored two further publications [1, 5]. However, I chose to put the focus of the thesis on columnar structure and left out the details of this work out of reasons of coherence.

6.5.1 Soft disk vs 2D foam simulation

In order to investigate the limit of the soft disk model, we compare results from this model with those from a well established 2D foam model, implemented in the `plat` software [78, 118, 119]. All results from such simulations in this section were carried out by with Friedrich Dunne, a former PhD Student in the Foams and Complex System Group at Trinity College Dublin.

`Plat` is a software for the simulation of random 2D foam [78, 118, 119] which is not based on an energy minimisation routine, but instead directly implements Plateau's laws for a 2D foam by modelling the films and liquid-

gas interfaces as circular arcs, constrained to meet smoothly at vertices. The radius of curvature r of each arc is determined by the Laplace law.

For a film this law is $p_i - p_j = 2\gamma/r$, where p_i and p_j are the pressures in the two adjacent bubbles and γ is the surface tension. For a liquid–gas interface $p_i - p_b = \gamma/r$, where p_b is the pressure in the Plateau border, set equal in all Plateau borders.

The 2D foam samples were generated as (nearly) dry foams (high packing fraction) by standard procedures [118–120]: A random Delauney tessellation is used to compute a Voronoi network. This is then converted to an (as yet unequilibrated) dry foam by decorating its vertices with small three-sided Plateau borders. The equilibration process of the decorated Voronoi network consists of adjusting cell pressure and the vertex positions (x_n, y_n) under the constraints of smoothly meeting arcs and area conservation for each bubble. Equilibrium is reached when the change in vertex positions is small.

A progressive decrease in steps of $\Delta\phi = 0.001$ in packing fraction was imposed to reach a given packing fraction ϕ and the system was equilibrated at each step. Decreases in packing fraction are performed by proportionally reducing bubble areas. The bubble radius distribution of the sample, which is calculated from bubble cell areas, follows a lognormal distribution.

The random soft disk packings are simulated with similar conditions (same polydispersity, same sample preparation protocol) as in `plat`. They are created using the BFGS minimisation routine to minimise the energy, as explained in chapter 2.5.1 [83].

Three samples of $N = 60$ bubbles at different packing fraction ϕ are presented in the top images of Fig 6.6. The bottom images show corresponding soft disk packing that were generated at the same value of ϕ. Differences between the two simulations are already visible from comparing these images: In the soft disk packings the disks overlap with increasing packing fraction, whereas the 2D foam simulations the bubbles/foam cells deform and take on

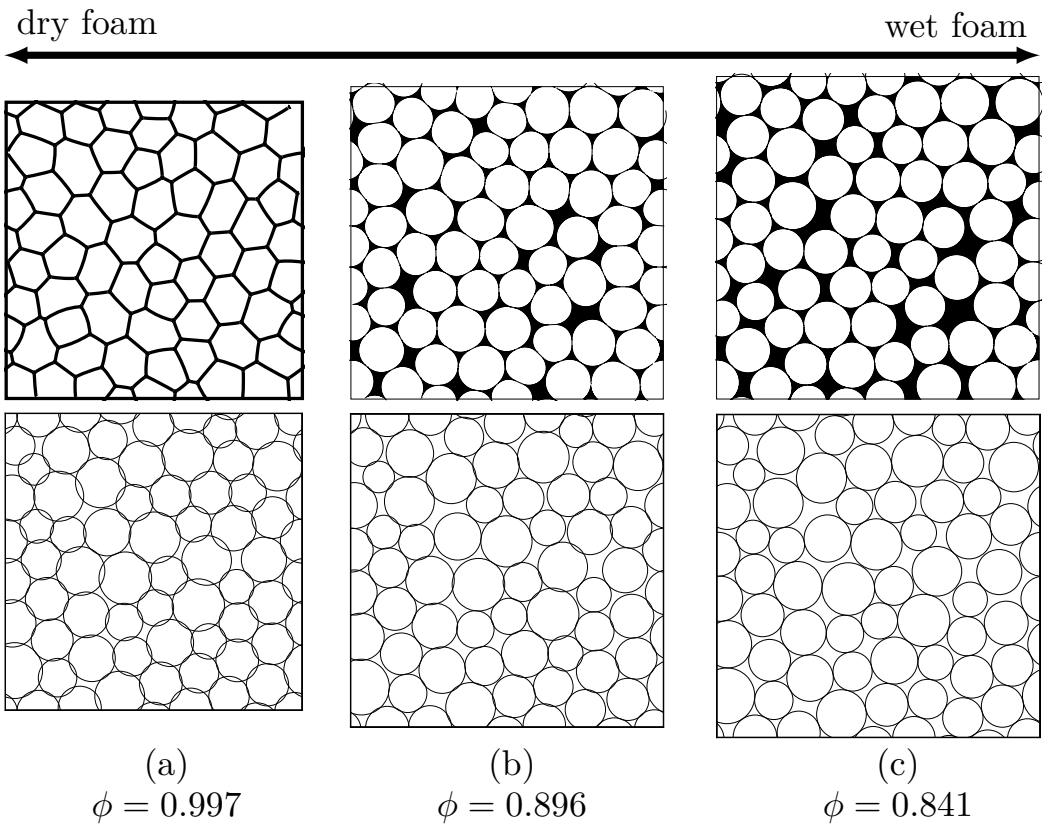

Fig 6.6: Comparison between a simulated 2D foam (three images at the top) and polydisperse soft disk packings (three images at the bottom) at different packing fraction ϕ. The top and bottom images in (a) correspond to a dry foam at a packing fraction of $\phi = 0.997$. The images in (b) are at a packing fraction of $\phi = 0.896$ and images in (c) are taken at the critical packing fraction of $\phi = 0.841$.

a polyhedral shape in the dry limit.

6.5.2 The average contact number $Z(\phi)$ for soft disk and 2D foam simulations

A quantitative discrepancy between these soft disk and 2D foam simulations was discovered in the variation of contact number $Z(\phi)$ with varying packing fraction ϕ. Previous simulations of the soft disk model [75, 121, 122] have shown that the average contact number $Z(\phi)$ varies in a square-root behaviour

above the critical point of jamming,

$$Z(\phi) - Z_c \propto (\phi - \phi_c)^{1/2}, \tag{6.1}$$

where ϕ_c is the packing fraction at the jamming point and Z_c the average contact number at ϕ_c. While local stability requires at least *three* neighbours for each disk at ϕ_c, overall stability requires $Z_c = 4$ as an average in an infinite 2D system [123].

In analysing our results we need to take into account a small finite-size correction. In the case of our finite system with periodic boundaries the critical value of the contact number is given by

$$Z_c = 4(1 - 1/N)\,, \tag{6.2}$$

where N is the number of bubbles; $N = 60$ in our case thus results in $Z_c = 3.933$. This relation is obtained from matching the number of degrees of freedom, $2N$ for a two-dimensional packing, with the number of constraints, due to the $ZN/2$ contacts. However, in a periodic system we can fix one bubble without loss of generality, leaving only $N - 1$ bubbles free to undergo translational motion.

As a standard procedure [122, 124], rattlers, which are bubbles with less than three contacts, were excluded in the analysis of both simulations. These do not contribute to the connected network and are mechanically unstable bubbles, which can be removed without changing the packing.

The main plot in Fig 6.7 displays the average contact number $Z(\phi)$ for the soft disks (blue data points) and the `plat` simulation (red data points). The soft disk data shows the expected square-root behaviour, as indicated by the fit with the solid blue line. But for the 2D foam simulations we find a linear variation in the $Z(\phi)$ above the critical packing fraction ϕ_c (solid red line in Fig 6.7). Appropriately, fitting

$$Z(\phi) = Z_c + k_{\mathrm{f}}(\phi - \phi_c), \tag{6.3}$$

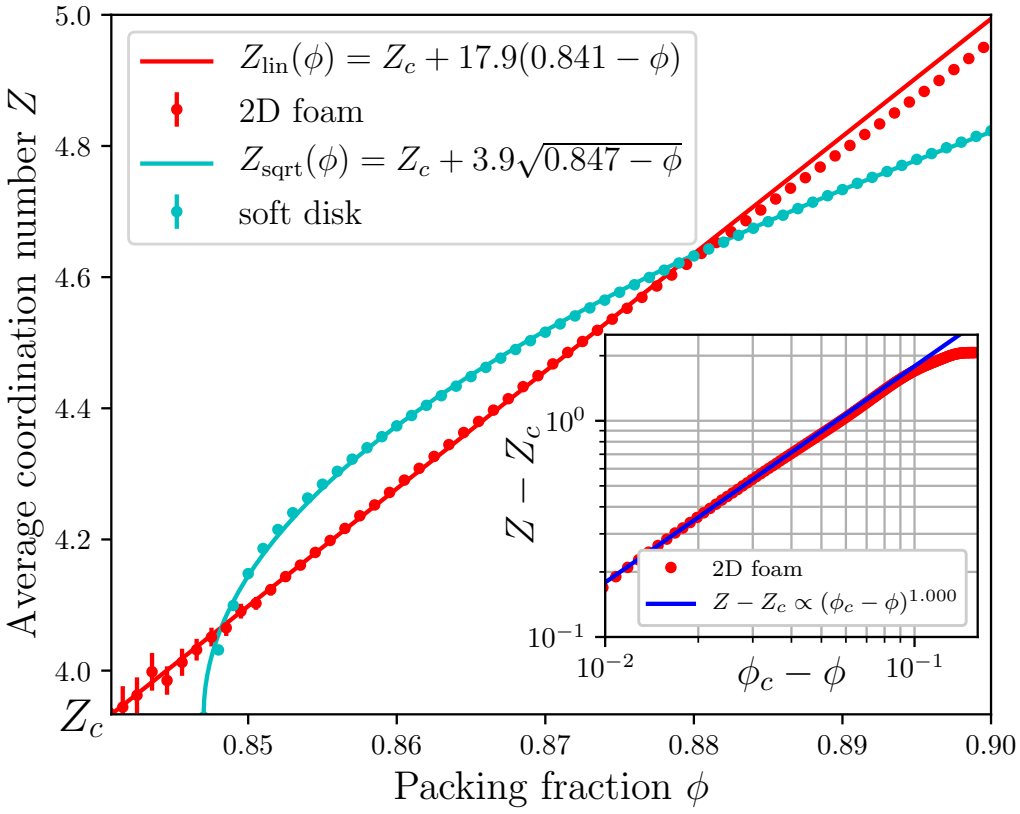

Fig 6.7: Comparison between the average contact number Z as a function of packing fraction ϕ for the soft disk simulation (blue data point) and the `plat` simulation for a 2D foam (red data points). For 2D foams close to the critical packing fraction ϕ_c, Z was found to vary linearly with $\phi - \phi_c$. $Z(\phi)$ for the soft disk system shows the well-known square-root scaling. For the soft disk systems we averaged over 20 000 realisations and for the `plat` results over 600 000 realisation, both with $N = 60$ bubbles/disks in each realisation. Inset: Double-logarithmic scale for $Z - Z_c$ vs. packing fractions $\phi - \phi_c$ up to $\phi = 1$. By fitting a linear function (solid line), the ϕ_c which gives the best linear relationship is obtained as $\phi_c = 0.841 \pm 0.001$.

to the `plat` data with $Z_c = 4 - 1/15$ gives $k_{\mathrm{f}} = 17.9 \pm 0.1$ and a critical gas fraction of $\phi_c = 0.841 \pm 0.001$. The value of ϕ_c is consistent with previous numerical results [120, 124, 125] The conclusion is therefore that Z approaches Z_c *linearly* for a 2D foam, whereas Z varies with a square root in ϕ in soft disk packings.

In the inset of Fig 6.7, we also plotted $\log(Z(\phi) - Z_c)$ vs. $\log(\phi - \phi_c)$, varying ϕ_c to obtain the value which gives the best *linear* relationship between these quantities. In this way, the critical packing fraction was found to be $\phi_c = 0.841 \pm 0.001$, and the slope is $\alpha = 1.000 \pm 0.004$ in the logarithmic plot. This corresponds to a power law relation

$$Z(\phi) - Z_c \propto (\phi - \phi_c)^{\alpha}\,, \tag{6.4}$$

which confirms the linear relationship for the 2D foam data.

If one describes foams in the wet limit as packings of disks (or spheres), then it is tempting to extend this analogy also to the functional relationship for $Z(\phi)$ and thus expect the same square-root relationship in lowest order. However, Surface Evolver simulations have shown that the energy is harmonic in 2D, but the bubble–bubble interactions are not pairwise-additive [77]. That is, the model of interaction that lies at the heart of the soft disk model does not represent realistic bubble–bubble interactions. One should therefore treat this prediction with some caution.

For 3D foams our results suggest also a deviation from the square-root scaling in $Z(\phi)$, since we conjecture the reason for the deviation in the 2D case to be the model of interaction. However, the scaling does not have to be linear. Apart from the non-pairwise interaction, the energy for the 3D bubble–bubble interaction is also not harmonic. It scales with the form $f^2 \ln(1/f)$, first predicted by Morse and Witten, where f is the force exerted between droplets [76, 77].

The variation of the average contact number $Z(\phi)$ with packing fraction ϕ is only one example where the soft sphere/disk model differs from the exact foam simulations. Further related discrepancies were studied in detail in Ref [1]. Although the consequences of such findings for columnar structures is unclear, these limits demonstrate the need for new simple models to investigate equilibrium soft matter structures, such as foams or emulsions. Further

investigations related to our columnar structures can then be carried out with these models, as we will discuss in the next section.

6.6 The Morse–Witten model for deformable spheres

One of those models that can be implemented in our simulations for future plans is the Morse–Witten model [5, 76, 126, 127]. It simulates deformable spheres such as bubbles or droplets based on the Morse–Witten theory [76]. This theory describes the shape of a bubble subject to a point force and an equal compensating body force, such as buoyancy or gravity. Fig 6.8 displays the shape of such a deformed bubble in 3D (a) and 2D (b) using the Morse–Witten theory.

Höhler and Weaire reviewed simulations based on this theory in Ref [126]. For instance, this theory can be used to describe the equilibrium shape of a single bubble pressed against a horizontal plate by an external body force (see Fig 6.8(a)). The contact force of the plate with the bubble is assumed to be a point force f. The Morse–Witten theory then approximates the bubble shape by linearising the curvature $\mathcal{C}$ of the interface in the Laplace–Young equation

$$\gamma\mathcal{C} = \Delta p\,. \tag{6.5}$$

The surface tension of the bubble interface is given by γ and Δp is the pressure difference across the interface. In 3D this assumption and approximation leads to a divergence of the shape at the contact point (see yellow part below the red disk in Fig 6.8(a)). However, since the correcting volume is of second order in the force f, this can be neglected.

The shape of a 2D bubble can be estimated in a similar fashion (Fig 6.8(b)) with the difference that no divergence occurs at $\theta = 0$. The comparison

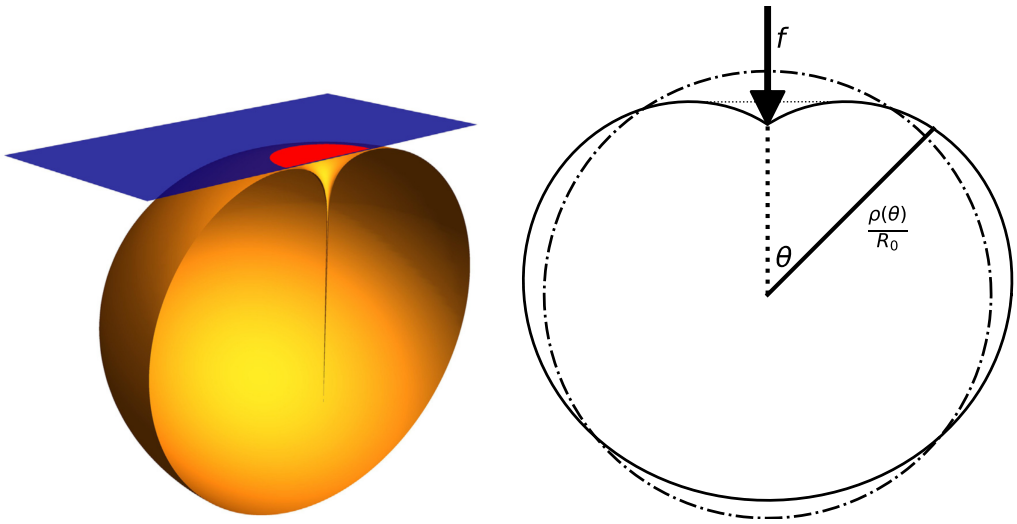

(a) (b)

Fig 6.8: The Morse–Witten theory is used to estimate the shape of a deformed bubble in 2D and 3D. In (a) the shape of a 3D bubble pushed against a horizontal plate (blue) by buoyancy is displayed. The red disk at the top of the bubble indicates the contact area of the bubble with the plate. The yellow part below the red disk is disregarded because its volume is negligible compared to the rest of the bubble [126]. (b) shows the shape $\rho(\theta)$ of a 2D bubble deformed by a point force f and an equal compensating body force, as described in the Morse–Witten theory. The undeformed bubble, which takes the shape of a disk with radius R_0, is shown by the dashed circle. The part of the profile below the faint horizontal dashed line is disregarded [5].

between the dashed circle and the shape of the bubble in Fig 6.8(b) shows clearly the effect of deformation for soft objects such as bubbles.

While the soft sphere model does not consider such deformation and assumes interactions to be pairwise, the Morse–Witten theory provides a formulation for a non-pairwise bubble–bubble interaction that takes deformation into account. A first simulation for a polydisperse wet foam was implemented by Dunne *et al.* [5] for 2D bubbles. This 2D simulation was found to be accurate in the limit of high liquid fraction where the bubbles are spherical. It superposes all contact forces of a bubble with its neighbouring bubbles to calculate the shape of a deformed bubble. By equilibrating the net forces of

all bubbles, one ends up with a stable bubble configuration.

However, such an implementation of the Morse–Witten model currently only exists for 2D foams. For most purposes related to this thesis a 3D implementation of monodisperse bubbles needs to be developed first.

The 2D implementation may already be used to extend the work from chapter 5 on sphere chains in a cylindrical harmonic potential to that of deformable and monodisperse bubbles. The 2D model can be applied here because the equilibrium structures are restricted to planar ones. The boundaries in form of the centripetal force and walls at both ends need to be added to the simulation. Both amendments are fairly simple: The centripetal force can be implemented as another force that contributes to the net force of each bubble and the walls may be modelled by two further horizontal point forces.

The 2D Morse–Witten simulation can also be applied to further 2D packing problem such as those introduced in section 6.4 of the outlook. Instead of investigating soft disks packed inside a rectangular channel, the Morse–Witten theory may be used to simulate 2D bubbles compressed by two vertical plates. Implementing the bubble-to-wall interaction may be of some difficulty.

A 3D implementation of the Morse–Witten model can be used to extend the investigations from chapter 3 and 4. Huge difficulties will have to be accomplished for simulating a columnar foam confined inside a cylinder (similar to the work in chapter 3) using this model. One major implementation issue will be related to simulating the correct interface and contact between a bubble and the curved cylinder wall. Such a situation probably needs to be studied separately in detail first.

The simulation of columnar structures of bubbles inside a rotating liquid-filled tube (see chapter 4), however, can be accomplished with less effort in 3D. Similar to the 2D case, the confinement in radial direction can simply be implemented by amending a centripetal force to the overall net force of the bubbles.

Appendix A

A.1 Tabulated hard sphere results

In the first part of the appendix we recapitulate some of the hard sphere results from Mughal *et al.* [14]. We present these previous results here in case the reader needs to look up some of the work that this thesis is based on. We mostly refer to this work in chapter 3.

Table A.1 displays the densest packings of hard spheres of diameter d inside a cylinder of diameter D. The table stops at the D/d value at which the nature of the structure changes significantly and structures with internal spheres occur. This table includes all structures that are also observed in the phase diagram of Fig 3.2 of chapter 3.

Fig A.1 presents the surface density vs the periodicity vector $\boldsymbol{V}$ (see chapter 1.3 for explanation) of disk packings on the surface of the cylinder. The corresponding 3D plot is shown in Fig A.2 (together with the 2D data). Both plots are heavily used in chapter 3 to investigate structural transition. Their information is needed to fill in the missing structural transition in the directed network of Fig 3.10.

The black line connecting the $(4, 2, 2)$ and $(4, 3, 1)$ structures in Fig A.1 indicates the special behaviour of the re-entrance case (see chapter 3.3.3). This line is slightly curved backwards, leading to two different surface densities at a given $|V|$ (or two different packing fractions at a given D/d in 3D).

Table A.1: Densest hard sphere packings.

structure	range	spheres in unit cell	notation
1 (C_1)	$D/d = 1$	1	straight chain
2	$1 \leq D/d \leq 1.866$	1	zigzag
3	$1.866 \leq D/d \leq 1.995$	1	twisted zigzag
4	$1.995 \leq D/d < 2.0$	2	(**2**,1,1)
5 (C_2)	$D/d = 2.0$	2	(2,2,0)
6	$2.0 < D/d \leq 2.039$	2	(2,**2**,0)
7	$D/d = 2.039$	1	(3,2,1)
8	$2.039 \leq D/d \leq 2.1413$	2	(3,**2**,1)
9	$2.1413 \leq D/d < 2.1545$	3	(**3**,2,1)
10 (C_3)	$D/d = 2.1547$	3	(3,3,0)
11	$2.1547 < D/d \leq 2.1949$	3	(3,**3**,0)
12	$2.1949 \leq D/d \leq 2.2247$	2	(3,**2**,1)
13	$D/d = 2.2247$	2	(4,2,2)
14	$2.2247 \leq D/d \leq 2.2655$	2	(4,2,**2**)\(4,**2**,2)
15	$2.2655 \leq D/d \leq 2.2905$	3	(3,**3**,0)
16	$D/d = 2.2905$	1	(4,3,1)
17	$2.2905 \leq D/d \leq 2.3804$	3	(4,**3**,1)
18	$2.3804 \leq D/d < 2.413$	4	(**4**,3,1)
19 (C_4)	$D/d = 2.4142$	4	(4,4,0)
20	$2.4142 < D/d \leq 2.4626$	4	(4,**4**,0)
21	$2.4626 \leq D/d \leq 2.4863$	3	(4,**3**,1)
22	$D = 2.4863$	1	(5,3,2)
23	$2.4863 \leq D/d \leq 2.5443$	3	(5,**3**,2)
24	$2.5443 \leq D/d \leq 2.5712$	4	(4,**4**,0)
25	$D = 2.5712$	1	(5,4,1)
26	$2.5712 \leq D/d \leq 2.655$	4	(5,**4**,1)
27	$2.655 \leq D/d < 2.7013$	5	(**5**,4,1)
28 (C_5)	$D/d = 2.7013$	5	(5,5,0)
29	$2.7013 < D/d \leq 2.71486$	5	(5,**5**,0)

Table listing the densest hard sphere packings inside a cylinder for a range of diameter ratios D/d where D is the cylinder and d the sphere diameter. The table stops at $D/d < 2.71486$, where the nature of the structure changes significantly and structures with internal spheres occur. Bold numerals designate the line-slip type. The table is taken from Ref [14].

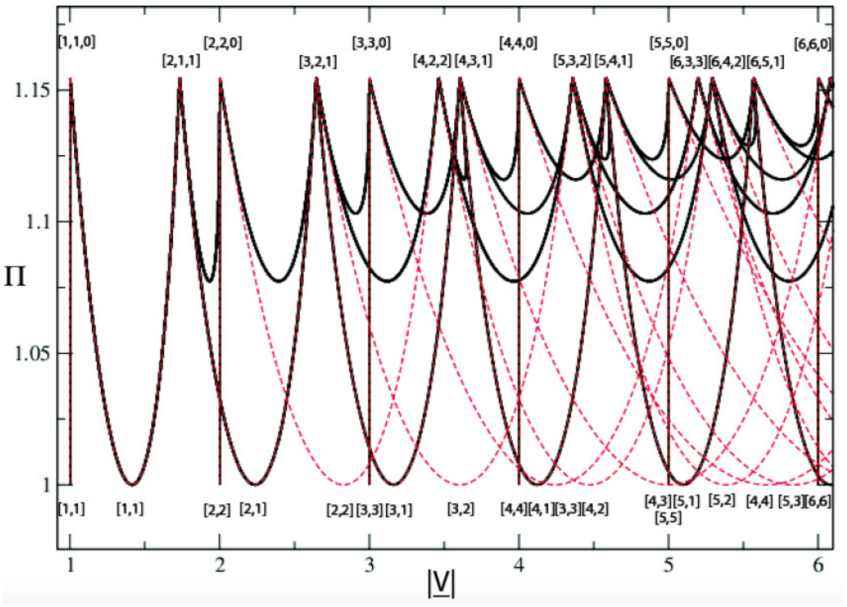

Fig A.1: Surface density vs the periodicity vector $\boldsymbol{V}$ of disk packings on the surface of a cylinder. Each black line connecting two peaks corresponds to a line-slip structure that relates two uniform structures (at the peaks), labelled with (n, m, l). They give rise to possible structural transition. The red dashed lines correspond to affine transitions that are not important for this thesis. The plot is taken from Ref [14].

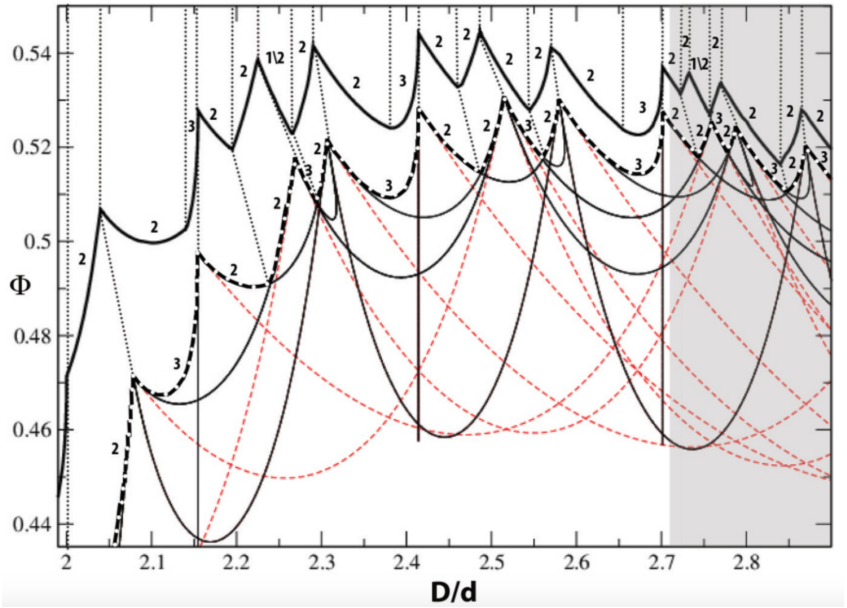

Fig A.2: Comparison of 3D and 2D packing fractions ϕ vs diameter ratio D/d for the densest hard sphere packings – upper and lower curves, respectively. Dotted lines are a guide for the eye to the detailed correspondence. For the 2D results, the line-slip structures are identified by black continuous lines. The plot is taken from Ref [14].

A.2 Employed minimisation routines

In this thesis, two different minimisation routines were used: The BFGS method to search for local energy (or enthalpy) minima and the Basin-hopping method to search for the global minimum. In this part of the Appendix we will provide closer detail about these two algorithms. Both algorithms are part of the scipy library [86], from where we imported these functions in our simulations.

For the reason of simplicity and illustrative purposes, we will refer to the function that is to be minimised as the energy function $\mathtt{E}(\boldsymbol{X})$ in the following two subsections. The vector $\boldsymbol{X}$ contains all the N parameter, on which the energy function depends. In our case these are mainly the positions of the spheres packed inside the cylinder.

This function to be minimised can nonetheless be generalised to any type of function, depending on the context of the minimisation. In physics, stable structures are obtained by seeking for the minimum of a thermodynamic potential. The energy and the enthalpy of a system are two example of such a potential that are used in this thesis.

The BFGS method – A quasi-Newton method

The simplest algorithm in finding the (local) minimum of a function is the gradient descent (or steepest descent) algorithm. This algorithm finds the local minimum by iteratively taking steps in the directions of the force vector $\boldsymbol{F}$ of the system. The force vector is defined as

$$\boldsymbol{F} = -\boldsymbol{\nabla}\mathtt{E}(\boldsymbol{X}) = -\begin{pmatrix} \frac{\partial \mathtt{E}}{\partial X_1} \\ \frac{\partial \mathtt{E}}{\partial X_2} \\ \vdots \\ \frac{\partial \mathtt{E}}{\partial X_N} \end{pmatrix}, \tag{A.1}$$

where N is the length of the parameter vector $\boldsymbol{X}$.

We used a more sophisticated algorithm to seek for the local minimum: The BFGS method [83, 86, 128]. It is named for its discoverers Broyden, Fletcher, Goldfarb, Shanno and belongs to the class of quasi-Newton algorithms [128]. Algorithms of this type are further advancements of the conjugate gradient algorithm and thus sometimes referred to as conjugate gradients as well (even though they are technically a different type of algorithm) [128].

All Newton methods are based on the second-order Taylor expansion around the minimum $\boldsymbol{X}_0$ of an energy function

$$\mathtt{E}(\boldsymbol{X}) = \mathtt{E}(\boldsymbol{X}_0) - \boldsymbol{F}^{\mathrm{T}} \cdot (\boldsymbol{X} - \boldsymbol{X}_0) + \frac{1}{2}(\boldsymbol{X} - \boldsymbol{X}_0)^{\mathrm{T}} \cdot \boldsymbol{H} \cdot (\boldsymbol{X} - \boldsymbol{X}_0) \tag{A.2}$$

with the force vector $\boldsymbol{F}$ and the Hessian $\boldsymbol{H}$ of the energy $\mathtt{E}(\boldsymbol{X})$. The Hessian is an $N \times N$ matrix that contains all second derivatives of the energy

$$\boldsymbol{H} = \begin{pmatrix} \frac{\partial^2 \mathtt{E}}{\partial X_1 \partial X_1} & \frac{\partial^2 \mathtt{E}}{\partial X_1 \partial X_2} & \cdots & \frac{\partial^2 \mathtt{E}}{\partial X_1 \partial X_N} \\ \frac{\partial^2 \mathtt{E}}{\partial X_2 \partial X_1} & \frac{\partial^2 \mathtt{E}}{\partial X_2 \partial X_2} & \cdots & \vdots \\ \vdots & \vdots & \ddots & \vdots \\ \frac{\partial^2 \mathtt{E}}{\partial X_N \partial X_1} & \cdots & \cdots & \frac{\partial^2 \mathtt{E}}{\partial X_N \partial X_N} \end{pmatrix}. \tag{A.3}$$

To avoid complicated analytic calculations, this matrix is often numerically approximated. Any Newton method that numerically approximates the Hessian is called a quasi-Newton algorithm.

Fig A.3 displays the pseudo-code of any Newton-type algorithm. The main step (line 4 of FigA.3) of the iterative scheme can be derived from eq. (A.2). By setting $E(\boldsymbol{X}_0) = 0$ (WLOG), one can see that the equation

$$\boldsymbol{H} \cdot \underbrace{(\boldsymbol{X} - \boldsymbol{X}_0)}_{\boldsymbol{p}_0} = \boldsymbol{F} \tag{A.4}$$

is satisfied in the (local) minimum for the Taylor expansion. Thus, solving this equation iteratively for the direction $\boldsymbol{p}_0$, yields a downhill direction to a possible minimum. This step is followed by a line search in the direction $\boldsymbol{p}_0$, which is usually done with the Wolfe algorithm [128]. The line search returns

Algorithm 1: The quasi-Newton method

input : Energy function $\mathtt{E}(\boldsymbol{X})$ and initial condition $\boldsymbol{X}_0$ of length N

output: Local minimum $\boldsymbol{X}_{\min}$

$\boldsymbol{F}_0 = -\boldsymbol{\nabla}\mathtt{E}(\boldsymbol{X}_0)$; // Calculate forces

$\boldsymbol{H}_0 = \boldsymbol{H}(\boldsymbol{X}_0)$; // Calculate Hessian

while $|\boldsymbol{F}_0| > \epsilon$ **do**

  Solve matrix equation $\boldsymbol{H}_0\boldsymbol{p}_0 = \boldsymbol{F}_0$ for $\boldsymbol{p}_0$;

  Line search along $\boldsymbol{X}_0 + \alpha\boldsymbol{p}_0$ for α ;

  $\boldsymbol{X}_{\min} = \boldsymbol{X}_0 = \boldsymbol{X}_0 + \alpha\boldsymbol{p}_0$;

  $\boldsymbol{F}_0 = -\boldsymbol{\nabla}\mathtt{E}(\boldsymbol{X}_0)$; // Update forces

  $\boldsymbol{H}_0 = \boldsymbol{H}(\boldsymbol{X}_0)$; // Update Hessian

end

Fig A.3: Pseudo-code for a quasi-Newton method to seek the nearest local minimum of an energy function $\mathtt{E}(\boldsymbol{X})$. It is based on iteratively solving the matrix equation (A.4) to find the direction $\boldsymbol{p}_0$, followed by a line search to find the step α to the nearest minimum in this direction. The parameter vector $\boldsymbol{X}_{\min}$, initial condition $\boldsymbol{X}_0$ as well as forces (or gradient) and Hessian are updated accordingly. For quasi-Newton methods, the Hessian is approximated numerically. The iterative scheme terminates when the absolute value of the forces drops below a certain threshold ϵ.

the step size α that one has to perform to find the nearest minimum along the direction $\boldsymbol{p}_0$. The parameter vectors $\boldsymbol{X}_{\min}$ and $\boldsymbol{X}_0$ are then updated to this minimum and the forces and Hessian calculated for this new minimum. The algorithm terminates when the absolute value of the forces $|\boldsymbol{F}_0|$ are below a certain threshold value ϵ, which is close to zero.

A common issue of this iterative scheme is a singular Hessian, which can occur. If the Hessian is singular, the matrix equation (A.4) has no solution. The BFGS method circumvents this issue by directly approximating the inverse of the Hessian.

Any Newton method or conjugate-gradient-type algorithm is a deterministic algorithm, i.e. the algorithm will always find the same minimum for a given initial condition $\boldsymbol{X}_0$ and there is no stochastic component in it. This makes it capable of only finding the nearest local minimum to a starting value $\boldsymbol{X}_0$. We make use of this property for investigating structural transitions in chapter 3 . On the downside, these algorithms are not suitable for searching for the global energy minimum because they easily get stuck in a local minimum.

The Basin-hopping algorithm

In order to find the global minimum of an energy function $\mathtt{E}(\boldsymbol{X})$, a stochastic component is needed. The landscape of a one dimensional energy function with many local minima is illustrated in Fig A.4. Searching for the minimum with a deterministic algorithm, such as the previously described BFGS method, results in the position of the blue dot as the minimum. However, the global minimum of this energy function is in the red dot. A stochastic component allows the initial guess to jump out of the initial basin (marked by the dashed lines). Based on this stochastic principle many global minimisation routines were developed.

The Basin-hopping algorithm is such a stochastic global minimisation technique [85]. Its iterative scheme resembles that of simulated annealing and made simulated annealing depreciated [86]. Just as simulated annealing, it is best suited to rugged variable landscapes consisting of many local minima (just like the one in Fig A.4), and combines heuristic procedures with local searches to effectively explore the entire space.

The pseudo-code algorithm in Fig A.5 illustrates this iterative search scheme. The minimum search is performed by perturbing the system, followed by a local optimisation in a given number of steps `niter`. The local minima with the initial guesses $\boldsymbol{X}_0'$ are calculated using conjugate-gradient- or quasi-Netwon-type algorithms (such as the BFGS method).

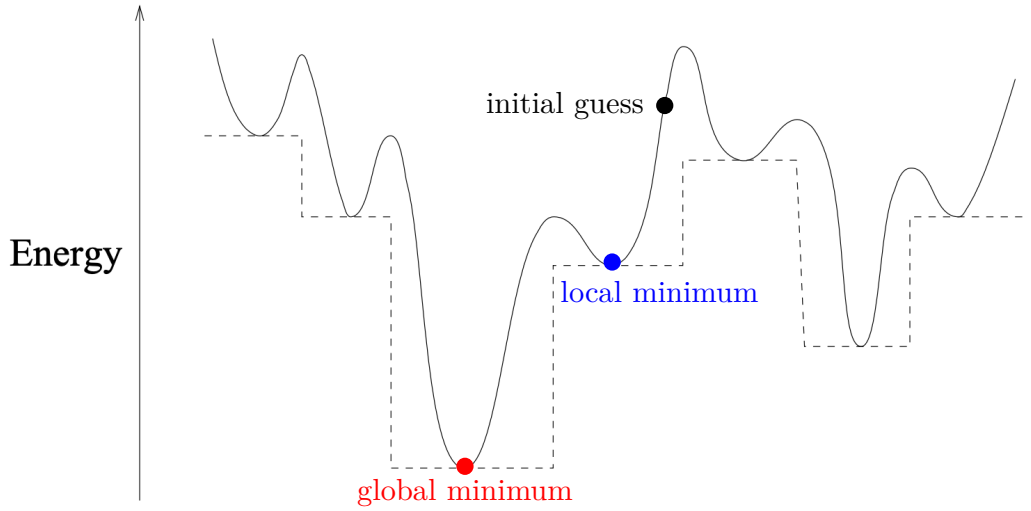

Fig A.4: Schematic plot of an energy landscape with many local minima [85]. The dashed lines map out the basins around each minimum of this landscape. The red dot represents the global minimum, while the blue dot is the nearest local minimum to the initial condition marked by the black dot.

If the energy of the new local minimum is below the previous minimum, the new step is always accepted. Otherwise the step is accepted with the Metropolis acceptance criterion that is also used in simulated annealing: The step is accepted with the probability

$$p_A = \exp\left(-\frac{\mathtt{E}(\boldsymbol{X}_{\text{new}}) - \mathtt{E}(\boldsymbol{X}_{\text{old}})}{\mathsf{T}}\right) , \tag{A.5}$$

where $\mathtt{E}(\boldsymbol{X}_{\text{old}})$ and $\mathtt{E}(\boldsymbol{X}_{\text{new}})$ are here the energies before and after the new step. With the temperature T, the likelihood of jumping to another basin can be tuned. During the iteration the global minimum is updated accordingly.

The perturbations in each step of the algorithm ensure that more than just one local minimum is explored and, with sufficient number of iterations, the probability of finding the global minimum tends to 1. The acceptance rate of the random perturbation is dependent on a given temperature T, which is where the comparisons to simulated annealing can be drawn.

Algorithm 2: Basin-hopping algorithm

input : Energy function $\mathtt{E}(\boldsymbol{X})$ with N-dimensional parameter $\boldsymbol{X}$

output: Global minimum $\boldsymbol{X}_{\min}$

$\boldsymbol{X}_0$ = random point in the parameter space ;
$\boldsymbol{X}_{\min} = \boldsymbol{X}_{\text{old}}$ = local minimum of $\mathtt{E}(\boldsymbol{X})$ around $\boldsymbol{X}_0$;
for $i = 0$ **to** niter **do**
    $\boldsymbol{X}_0'$ = randomly perturb parameter $\boldsymbol{X}_0$;
    $\boldsymbol{X}_{\text{new}}$ = local minimum of $\mathtt{E}(\boldsymbol{X})$ around $\boldsymbol{X}_0'$;
    q = random number $\in (0, 1]$;
    if $\mathtt{E}(\boldsymbol{X}_{\text{new}}) < \mathtt{E}(\boldsymbol{X}_{\text{old}})$ **or** $\exp(-(\mathtt{E}(\boldsymbol{X}_{\text{new}}) - \mathtt{E}(\boldsymbol{X}_{\text{old}}))/\mathsf{T}) < q$ **then**
        $\boldsymbol{X}_0, \boldsymbol{X}_{\text{old}} = \boldsymbol{X}_0', \boldsymbol{X}_{\text{new}}$; // accept new step
    end
    if $\mathtt{E}(\boldsymbol{X}_{\text{new}}) \leq \mathtt{E}(\boldsymbol{X}_{\min})$ **then**
        $\boldsymbol{X}_{\min} = \boldsymbol{X}_{\text{new}}$; // update new global minimum
    end
end

Fig A.5: Pseudo-code for the basin-hopping algorithm used to minimise an energy function $\mathtt{E}(\boldsymbol{X})$ in N dimensions. It finds the global minimum iteratively by performing three steps in each of the `niter` iterations: First, the parameter $\boldsymbol{X}_0$ is randomly perturbed and stored in $\boldsymbol{X}_0'$. Second, the nearest local minimum from $\boldsymbol{X}_0'$ is obtained with a conjugate-gradient-type algorithm. This step of perturbation is accepted via the Metropolis acceptance criterion with temperature T. The minimum $\boldsymbol{X}_{\min}$ is updated accordingly.

A.3 Analytic energy calculations for achiral $(l, l, 0)$ structures

Here, we show the detailed analytic energy calculation for all achiral and homogeneous columnar structures of the form $(l, l, 0)$ [e.g. $(2, 2, 0)$, $(3, 3, 0)$ and (4, 4, 0)]. This serves as an example for the analytic calculations performed

in chapter 4.

The calculation starts with eq. (4.8) of the total energy per sphere E^S_{rot} from chapter 4

$$\frac{E^{\mathrm{S}}_{\mathrm{rot}}}{M\omega^2 d^2} = \frac{1}{2}\frac{R^2}{d^2} + \frac{1}{2}\frac{k}{M\omega^2}\left\langle\left(\frac{\delta_{ij}}{d}\right)^2\right\rangle . \tag{A.6}$$

The first term corresponds to the rotational energy, while the second term is the sphere–sphere interaction, which is structure dependent.

The $(l, l, 0)$ structures consists of packings with l spheres in one layer that are stacked on top of each other (compare also Fig 1.1 for the $(3, 3, 0)$ structure). Thus, the second term of the average squared overlaps $\left\langle \delta^2_{ij}/d^2\right\rangle$ can be split into two terms

$$\left\langle\left(\frac{\delta_{ij}}{d}\right)^2\right\rangle = \Delta_{\mathrm{Layer}} + 2\Delta_{\mathrm{Top}} . \tag{A.7}$$

These two terms describe the average squared overlap of one sphere in the structure with neighbouring spheres. The first one Δ_{Layer} is due to the overlap with one contacting sphere in the same layer. The second term Δ_{Top} is the overlap with two spheres from the layer above (or below). The two terms can formally be written as

$$\Delta_{\mathrm{Layer}} = \frac{(d - r_0(R))^2}{d^2} \tag{A.8}$$

$$\Delta_{\mathrm{Top}} = \frac{(d - h(L, R))^2}{d^2} , \tag{A.9}$$

where r_0 and h are centre–centre distances between these spheres within the same layer and spheres above (or below), respectively. They only depend on the geometry of the structure and are functions of the radial distance R and the length L between the layer.

For r_0 we find

$$r_0(R) = 2R\sin\left(\frac{\pi}{l}\right) . \tag{A.10}$$

For the distance h we focus on two centre positions of the spheres, one de-

scribed by the coordinates (x_0, y_0, z_0) and the other by (x_1, y_1, z_1):

$$\begin{aligned} x_0 &= 0 & x_1 &= R\cos\left(\frac{\pi}{l}\right) \\ y_0 &= R\sin\left(\frac{\pi}{2}\right) & y_1 &= R\cos\left(\frac{\pi}{2}+\frac{\pi}{l}\right) \\ z_0 &= 0 & z_1 &= L\,. \end{aligned} \tag{A.11}$$

The distance between those two spheres is then

$$h(R,L) = \sqrt{R^2\cos^2\left(\frac{\pi}{l}\right) + R^2\left(\sin\left(\frac{\pi}{2}+\frac{\pi}{l}\right)-1\right)^2 + L^2} \tag{A.12}$$

Substituting the expressions for r_0 and h back into the total energy yields the following expression for the energy:

$$\begin{aligned} \frac{E^{\mathrm{S}}_{(l,l,0)}(R,L)}{M\omega^2 d^2} &= \frac{1}{2}\frac{R^2}{d^2} + \frac{1}{2}\frac{k}{M\omega^2 d^2}\left(\left(d - 2R\sin\left(\frac{\pi}{l}\right)\right)^2\right. \\ &\left. + \left(d - \sqrt{R^2\cos^2\left(\frac{\pi}{l}\right) + R^2\left(\sin\left(\frac{\pi}{2}+\frac{\pi}{l}\right)-1\right)^2 + L^2}\right)^2\right)\,. \end{aligned} \tag{A.13}$$

The total energy E^S_{rot} is now only a function of two variables, the radial distance R and length L. The total energy can then be minimised with analytic or numerical methods with respect to only the radial distance R, while the length L is kept fixed. This length L can be related to the linear number density ρ as described in chapter 4.

Bibliography

[1] J. Winkelmann, F. Dunne, V. Langlois, M. Möbius, D. Weaire, and S. Hutzler, *2d foams above the jamming transition: deformation matters*, Colloids Surf. A **534**, 52–57 (2017).

[2] J. Winkelmann, B. Haffner, D. Weaire, A. Mughal, and S. Hutzler, *Corrected Article: Simulation and observation of line-slip structures in columnar structures of soft spheres [Phys. Rev. E 96, 012610 (2017)]*, Phys. Rev. E **97**, 059902 (2017).

[3] A. Mughal, J. Winkelmann, D. Weaire, and S. Hutzler, *Columnar structures of soft spheres: metastability and hysteresis*, Phys. Rev. E **98**, 043303 (2018).

[4] J. Winkelmann, A. Mughal, D. Williams, D. Weaire, and S. Hutzler, *Theory of rotational columnar structures of soft spheres*, Phys. Rev. E **99**, 020602(R) (2019).

[5] F. F. Dunne, J. Winkelmann, D. Weaire, and S. Hutzler, *Implementation of morse–witten theory for a polydisperse wet 2d foam simulation*, Phil. Mag. **99**, 2303–2320 (2019).

[6] J. Winkelmann, A. Mughal, D. Weaire, and S. Hutzler, *Equilibrium configurations of hard spheres in a cylindrical harmonic potential*, EPL, accepted for publication. (2019).

[7] J. Winkelmann, *Ordered columnar structures: Golf balls packed inside tube*, (2019) `https://www.reddit.com/r/ScienceGIFs/comments/b2c604/ordered_columnar_structures_golf_balls_packed/` (visited on 07/23/2019).

[8] T. Lee, K. Gizynski, and B. Grzybowski, *Non-equilibrium self-assembly of monocomponent and multicomponent tubular structures in rotating fluids*, Adv. Mater. **29**, 1704274 (2017).

[9] I. Douglass, H. Mayger, T. Hudson, and P. Harrowell, *The stabilization of tubular crystals in mixtures of spherical particles*, Soft Matter **13**, 1344–1351 (2017).

[10] A. Rogava, *Tennis-ball towers*, Physics World **32**, 25–25 (2019).

[11] M. Livio, *The Golden Ratio: The Story of PHI, the World's Most Astonishing Number* (Crown/Archetype, 2008).

[12] D. W. Thompson, *On growth and form*, 1nd ed. (Cambridge University Press Cambridge, Eng, 1917), 2 v. :

[13] J.-F. Sadoc, N. Rivier, and J. Charvolin, *Phyllotaxis: a non-conventional crystalline solution to packing efficiency in situations with radial symmetry*, Acta Crystallographica Section A **68**, 470–483 (2012).

[14] A. Mughal, H. Chan, D. Weaire, and S. Hutzler, *Dense packings of spheres in cylinders: simulations*, Phys. Rev. E **85**, 051305 (2012).

[15] K. Troche, V. Coluci, S. Braga, D. Chinellato, F. Sato, S. Legoas, R. Rurali, and D. Galãvo, *Prediction of ordered phases of encapsulated c60, c70, and c78 inside carbon nanotubes*, Nano Letters **5**, 349–355 (2005).

[16] G. Wu, H. Cho, D. A. Wood, A. D. Dinsmore, and S. Yang, *Confined assemblies of colloidal particles with soft repulsive interactions*, J. Am. Chem. Soc. **139**, 5095–5101 (2017).

[17] *London, England: Kew Gardens: Titan Arum seeds ripening*, (2005) `http://www.cambridge2000.com/gallery/html/PA309665e.html` (visited on 08/12/2019).

[18] Z. Liang, Y. Liu, F. Zhang, Y. Ai, and Q. Liang, *Dehydration-triggered shape morphing based on asymmetric bubble hydrogel microfibers*, Soft Matter **14**, 6623–6626 (2018).

[19] N. Tanjeem, D. B. H. Wilkin, C. Rycroft, and V. Manoharan, "Line-slip defects in colloidal crystals on a cylinder", in Bulletin of the American Physical Society (2018).

[20] R. O. Erickson, *Tubular packing of spheres in biological fine structure*, Science **181**, 705–716 (1973).

[21] A. Amir and D. R. Nelson, *Dislocation-mediated growth of bacterial cell walls*, PNAS **109**, 9833–9838 (2012).

[22] R. Hull, *The structure of tubular viruses*, Adv. Virus Res. **20**, 1–32 (1976).

[23] J. Bryan, *Microtubules*, BioScience **24**, 701–711 (1974).

[24] W. Brinkley, *Microtubules: A brief historical perspective*, J. Struct. Biol. **118**, 84–86 (1997).

[25] J. Norman, E. Sorrell, Y. Hu, V. Siripurapu, J. Garcia, J. Bagwell, P. Charbonneau, S. Lubkin, and M. Bagnat, *Tissue self-organization underlies morphogenesis of the notochord*, Philos. Trans. Royal Soc. B **373** (2018).

[26] R. Erickson, edited by J. Dale and M. FL (University Press, Cambridge, 1983) Chap. The geometry of phyllotaxis, pp. 53–88.

[27] P. Prusinkiewicz and L. A (Springer Verlag, 1990) Chap. Phyllotaxis, pp. 99–118.

[28] R. N. Pittet N and W. D, *Cylindral packing of foam cells*, Forma **10**, 65–73 (1995).

[29] M. Saadatfar, J. Barry, D. Weaire, and S. Hutzler, *Ordered cylindrical foam structures with internal bubbles*, Philos. Mag. **88**, 661–668 (2008).

[30] S. Tobin, J. Barry, A. Meagher, B. Bulfin, C. O'Rathaille, and S. Hutzler, *Ordered polyhedral foams in tubes with circular, triangular and square cross-section*, Colloids Surf. A **382**, 24–31 (2011).

[31] A. Meagher, F. García-Moreno, J. Banhart, A. Mughal, and S. Hutzler, *An experimental study of columnar crystals using monodisperse microbubbles*, Colloids Surf. A **473**, 55–59 (2015).

[32] S. Hutzler, D. Weaire, and R. Crawford, *Moving boundaries in ordered cylindrical foam structures*, Phil. Mag. Part B **75**, 845–857 (1997).

[33] D. Weaire, S. Hutzler, G. Verbist, and E. Peters, *A review of foam drainage*, Adv. Chem. Phys. **102**, 315–374 (1997).

[34] S. Hutzler, D. Weaire, and R. Crawford, *Convective instability in foam drainage*, EPL **41**, 461 (1998).

[35] K. A. Brakke, *The surface evolver*, Exp. Math. **1**, 141–165 (1992).

[36] W. Drenckhan, S. Cox, G. Delaney, H. Holste, D. Weaire, and N. Kern, *Rheology of ordered foams—on the way to Discrete Microfluidics*, Colloids Surf. A **263**, 52–64 (2005).

[37] N. Pittet, P. Boltenhagen, N. Rivier, and D. Weaire, *Structural transitions in ordered, cylindrical foams*, EPL **35**, 547 (1996).

[38] P. Boltenhagen, N. Pittet, and N. Rivier, *Giant deformations and topological hysteresis of an ordered foam*, EPL **43**, 690 (1998).

[39] P. Boltenhagen and N. Pittet, *Structural transitions in crystalline foams*, EPL **41**, 571 (1998).

[40] K. Cox, J. Winkelmann, and S. Hutzler, *Chainlike arrangement of equal-volume soap bubbles*, In preparation. (2019).

[41] A. Brisson and P. Unwin, *Tubular crystals of acetylcholine receptor.* J. Cell Biol. **99**, 1202–1211 (1984).

[42] R. E. Smalley, M. S. Dresselhaus, G. Dresselhaus, and P. Avouris, *Carbon nanotubes: synthesis, structure, properties, and applications*, Vol. 80 (Springer Science & Business Media, Germany, 2003).

[43] N. Chopra, R. Luyken, K. Cherrey, V. Crespi, M. Cohen, S. Louie, and A. Zettl, *Boron nitride nanotubes*, Science **269**, 966 (1995).

[44] M. A. Lohr, A. M. Alsayed, B. G. Chen, Z. Zhang, R. D. Kamien, and A. G. Yodh, *Helical packings and phase transformations of soft spheres in cylinders*, Phys. Rev. E **81**, 040401 (2010).

[45] D. Wood, C. Santangelo, and A. Dinsmore, *Self-assembly on a cylinder: A model system for understanding the constraint of commensurability*, Soft Matter **9**, 10016–10024 (2013).

[46] Q. Zhang, J. Gu, L. Zhang, and J. Lin, *Diverse chiral assemblies of nanoparticles directed by achiral block copolymers via nanochannel confinement*, Nanoscale **11**, 474–484 (2019).

[47] D. Wood, *Assembly of particles onto rigid cylinders and flexible membranes: probing effects of surface curvature and deformation*, (2017).

[48] T. Yamazaki, K. Kuramochi, D. Takagi, Y. Homma, F. Nishimura, N. Hori, K. Watanabe, S. Suzuki, and Y. Kobayashi, *Ordered fullerene nanocylinders in large-diameter carbon nanotubes*, Nanotechnology **19**, 045702 (2008).

[49] J. Warner and M. Wilson, *Elastic Distortions of Carbon Nanotubes Induced by Chiral Fullerene Chains.* ACS Nano.

[50] K. Wang, S.-M. Jin, J. Xu, R. Liang, K. Shezad, Z. Xue, X. Xie, E. Lee, and J. Zhu, *Electric-field-assisted assembly of polymer-tethered gold nanorods in cylindrical nanopores*, ACS Nano **10**, 4954–4960 (2016).

[51] S. Sanwaria, A. Horechyy, D. Wolf, C.-Y. Chu, H.-L. Chen, P. Formanek, M. Stamm, R. Srivastava, and B. Nandan, *Helical packing of nanoparticles confined in cylindrical domains of a self-assembled block copolymer structure*, Angew. Chem. **53**, 9090–9093 (2014).

[52] G. R. Lázaro, B. Dragnea, and M. F. Hagan, *Self-assembly of convex particles on spherocylindrical surfaces*, Soft Matter **14**, 5728–5740 (2018).

[53] J. P. Hill, W. Jin, A. Kosaka, T. Fukushima, H. Ichihara, T. Shimomura, K. Ito, T. Hashizume, N. Ishii, and T. Aida, *Self-Assembled Hexa-peri-hexabenzocoronene Graphitic Nanotube*, Science **304**, 1481–1483 (2004).

[54] N. B. Schade, M. C. Holmes-Cerfon, E. R. Chen, D. Aronzon, J. W. Collins, J. A. Fan, F. Capasso, and V. N. Manoharan, *Tetrahedral colloidal clusters from random parking of bidisperse spheres*, Phys. Rev. Lett. **110**, 148303 (2013).

[55] V. Manoharan, *Manoharan lab - optical metamaterials*, (2019) `https://manoharan.seas.harvard.edu/self-assembled-metamaterials` (visited on 07/23/2019).

[56] E. Ozbay, *The magical world of photonic metamaterials*, Opt. Photon. News **19**, 22–27 (2008).

[57] V. M. Shalaev, *Optical negative-index metamaterials*, Nat. photonics **1**, 41 (2007).

[58] W. Cai, U. K. Chettiar, A. V. Kildishev, and V. M. Shalaev, *Optical cloaking with metamaterials*, Nat. photonics **1**, 224 (2007).

[59] V. T. Cong, E.-O. Ganbold, J. K. Saha, J. Jang, J. Min, J. Choo, S. Kim, N. W. Song, S. J. Son, S. B. Lee, and S.-W. Joo, *Gold nanoparticle silica nanopeapods*, J. Am. Chem. Soc. **136**, 3833–3841 (2014).

[60] Z. Fan and A. O. Govorov, *Helical metal nanoparticle assemblies with defects: plasmonic chirality and circular dichroism*, J. Phys. Chem. C **115**, 13254–13261 (2011).

[61] M. D. Turner, M. Saba, Q. Zhang, B. P. Cumming, G. E. Schröder-Turk, and M. Gu, "A chiral beamsplitter inspired by butterfly nanostructures", in Frontiers in optics 2013 postdeadline (2013), FW6A.3.

[62] M. D. Turner, M. Saba, Q. Zhang, B. P. Cumming, G. E. Schröder-Turk, and M. Gu, *Miniature chiral beamsplitter based on gyroid photonic crystals*, Nat. Photonics **7**, 801 (2013).

[63] M. Saba, M. D. Turner, K. Mecke, M. Gu, and G. E. Schröder-Turk, *Group theory of circular-polarization effects in chiral photonic crystals with four-fold rotation axes applied to the eight-fold intergrowth of gyroid nets*, Phys. Rev. B **88**, 245116 (2013).

[64] L. Fu, C. Bian, C. W. Shields IV, D. F. Cruz, G. P. López, and P. Charbonneau, *Assembly of hard spheres in a cylinder: A computational and experimental study*, Soft Matter **13**, 3296–3306 (2017).

[65] L. Fu, W. Steinhardt, H. Zhao, J. E. Socolar, and P. Charbonneau, *Hard sphere packings within cylinders*, Soft Matter **12**, 2505–2514 (2016).

[66] T. C. Hales, *A proof of the kepler conjecture*, Ann. Math., 1065–1185 (2005).

[67] M. O'Keeffe, *Sphere Packings and Space Filling by Congruent Simple Polyhedra*, Acta Crystallographica Section A **54**, 320–329 (1998).

[68] E. Koch and W. Fischer, "Sphere packings and packings of ellipsoids", in *International tables for crystallography volume c: mathematical, physical and chemical tables*, edited by E. Prince (Springer Netherlands, Dordrecht, 2004), pp. 746–751.

[69] Y. G. Stoyan and G. N. Yaskov, *Packing identical spheres into a cylinder*, Int. T. Oper. Res. **17**, 51–70 (2010).

[70] H.-K. Chan, *Densest columnar structures of hard spheres from sequential deposition*, Phys. Rev. E **84**, 050302 (2011).

[71] A. Mughal, H. K. Chan, and D. Weaire, *Phyllotactic description of hard sphere packing in cylindrical channels*, Phys. Rev. Lett. **106**, 115704 (2011).

[72] A. Mughal, *Screw symmetry in columnar crystals*, Phil. Mag. **93**, 4070–4077 (2013).

[73] J.-P. Hansen and I. R. McDonald, *Theory of simple liquids* (Elsevier, 1990).

[74] G. Schroeder-Turk, J. Knauf, R. Roth, and K. Mecke, *Can a hard-sphere fluid feel the topology of a confining pore?*, Bulletin of the American Physical Society **60** (2015).

[75] D. Durian, *Foam mechanics at the bubble scale*, Phys. Rev. Lett. **75**, 4780 (1995).

[76] D. Morse and T. Witten, *Droplet elasticity in weakly compressed emulsions*, EPL **22**, 549–555 (1993).

[77] M. D. Lacasse, G. S. Grest, and D. Levine, *Deformation of small compressed droplets*, Phys. Rev. E **54**, 5436–5446 (1996).

[78] F. Bolton, *Software plat: a computer code for simulating two-dimensional liquid foams*, `https://github.com/fbolton/plat`, 1996.

[79] A. Boromand, A. Signoriello, F. Ye, C. S. O'Hern, and M. D. Shattuck, *Jamming of deformable polygons*, Phys. Rev. Lett. **121**, 248003 (2018).

[80] A. Boromand, A. Signoriello, J. Lowensohn, C. S. Orellana, E. R. Weeks, F. Ye, M. D. Shattuck, and C. S. O'Hern, *The role of deformability in determining the structural and mechanical properties of bubbles and emulsions*, Soft Matter **15**, 5854–5865 (2019).

[81] M. Z. Yamchi and R. K. Bowles, *Helical defect packings in a quasi-one-dimensional system of cylindrically confined hard spheres*, Phys. Rev. Lett. **115**, 025702 (2015).

[82] G. T. Pickett, M. Gross, and H. Okuyama, *Spontaneous chirality in simple systems*, Phys. Rev. Lett. **85**, 3652–3655 (2000).

[83] R. H. Byrd, P. Lu, J. Nocedal, and C. Zhu, *A Limited Memory Algorithm for Bound Constrained Optimization*, SIAM J. Sci. Comput. **16**, 1190–1208 (1995).

[84] N. Metropolis, A. W. Rosenbluth, M. N. Rosenbluth, A. H. Teller, and E. Teller, *Equation of State Calculations by Fast Computing Machines*, J. Chem. Phys. **21**, 1087–1092 (1953).

[85] D. J. Wales and J. P. K. Doye, *Global optimization by basin-hopping and the lowest energy structures of lennard-jones clusters containing up to 110 atoms*, J. Phys. Chem. A **101**, 5111–5116 (1997).

[86] E. Jones, T. Oliphant, P. Peterson, et al., *SciPy: Open source scientific tools for Python*, 2001.

[87] A. Mughal and D. Weaire, *Theory of cylindrical dense packings of disks*, Phys. Rev. E **89**, 042307 (2014).

[88] D. Weaire, N. Pittet, S. Hutzler, and D. Pardal, *Steady-state drainage of an aqueous foam*, Phys. Rev. Lett. **71**, 2670 (1993).

[89] S. A. Koehler, S. Hilgenfeldt, and H. A. Stone, *A generalized view of foam drainage: experiment and theory*, Langmuir **16**, 6327–6341 (2000).

[90] V. Tsytovich, G. Morfill, V. Fortov, N. Gusein-Zade, B. Klumov, and S. Vladimirov, *From plasma crystals and helical structures towards inorganic living matter*, New J. Phys. **9**, 263 (2007).

[91] D. Zerrouki, J. Baudry, D. Pine, P. Chaikin, and J. Bibette, *Chiral colloidal clusters*, Nature **455**, 380–382 (2008).

[92] Y. Yin and Y. Xia, *Self-assembly of spherical colloids into helical chains with well-controlled handedness*, J. Am. Chem. Soc. **125**, 2048–2049 (2003).

[93] E. C. Oğuz, R. Messina, and H. Löwen, *Crystalline multilayers of the confined yukawa system*, EPL **86**, 28002 (2009).

[94] S. Hutzler, R. P. Murtagh, D. Whyte, S. T. Tobin, and D. Weaire, *Z-cone model for the energy of an ordered foam*, Soft Matter **10**, 7103–7108 (2014).

[95] *DesignerData*, (2019) `http://www.designerdata.nl/plastics/thermo+plastics/PP` (visited on 08/13/2019).

[96] N. D. Mermin and H. Wagner, *Absence of ferromagnetism or antiferromagnetism in one- or two-dimensional isotropic heisenberg models*, Phys. Rev. Lett. **17**, 1133–1136 (1966).

[97] R. Abbaschian and R. Reed-Hill, *Physical Metallurgy Principles* (Cengage Learning, 2008).

[98] T. Dessup, T. Maimbourg, C. Coste, and M. Saint Jean, *Linear instability of a zigzag pattern*, Phys. Rev. E **91**, 022908 (2015).

[99] H. Landa, B. Reznik, J. Brox, M. Mielenz, and T. Schätz, *Structure, dynamics and bifurcations of discrete solitons in trapped ion crystals*, New J. Phys. **15**, 093003 (2013).

[100] M. Mielenz, J. Brox, S. Kahra, G. Leschhorn, M. Albert, T. Schätz, H. Landa, and B. Reznik, *Trapping of topological-structural defects in Coulomb crystals*, Phys. Rev. Lett. **110**, 133004 (2013).

[101] K. Pyka, J. Keller, H. Partner, R. Nigmatullin, T. Burgermeister, D. Meier, K. Kuhlmann, A. Retzker, M. B. Plenio, W. Zurek, et al., *Topological defect formation and spontaneous symmetry breaking in ion Coulomb crystals*, Nat. Commun. **4**, 2291 (2013).

[102] R. C. Thompson, *Ion coulomb crystals*, Contemp. Phys. **56**, 63–79 (2015).

[103] H. L. Partner, R. Nigmatullin, T. Burgermeister, J. Keller, K. Pyka, M. B. Plenio, A. Retzker, W. H. Zurek, A. del Campo, and T. E. Mehlstäubler, *Structural phase transitions and topological defects in ion coulomb crystals*, Physica B: Condensed Matter **460**, 114–118 (2015).

[104] R. Nigmatullin, A. del Campo, G. De Chiara, G. Morigi, M. B. Plenio, and A. Retzker, *Formation of helical ion chains*, Phys. Rev. B **93**, 014106 (2016).

[105] L. Yan, W. Wan, L. Chen, F. Zhou, S. Gong, X. Tong, and M. Feng, *Exploring structural phase transitions of ion crystals*, Sci. Rep. **6**, 21547 (2016).

[106] G. W. Hunt, A. Tordesillas, S. C. Green, and J. Shi, *Force-chain buckling in granular media: a structural mechanics perspective*, Philos. Trans. Royal Soc. A **368**, 249–262 (2010).

[107] A. V. Straube, R. P. A. Dullens, L. Schimansky-Geier, and A. A. Louis, *Zigzag transitions and nonequilibrium pattern formation in colloidal chains*, J. Chem. Phys. **139**, 134908 (2013).

[108] A. Melzer, *Zigzag transition of finite dust clusters*, Phys. Rev. E **73**, 056404 (2006).

[109] A. V. Straube, A. A. Louis, J. Baumgartl, C. Bechinger, and R. P. A. Dullens, *Pattern formation in colloidal explosions*, EPL **94**, 48008 (2011).

[110] T. Beatus, T. Tlusty, and R. Bar-Ziv, *Phonons in a one-dimensional microfluidic crystal*, Nat. Phys. **2**, 743–748 (2006).

[111] R. P. S. Balls, (2019) `https://www.redhill-balls.eu` (visited on 07/23/2019).

[112] T. C. Michaels, R. Kusters, A. J. Dear, C. Storm, J. C. Weaver, and L. Mahadevan, *Geometric localization in supported elastic struts*, arXiv preprint arXiv:1906.04638 (2019).

[113] T. S. Majmudar and R. P. Behringer, *Contact force measurements and stress-induced anisotropy in granular materials*, Nature **435**, 1079–1082 (2005).

[114] K. E. Daniels, J. E. Kollmer, and J. G. Puckett, *Photoelastic force measurements in granular materials*, Rev. Sci. Instrum. **88**, 051808 (2017).

[115] A. Irannezhad, A. Mughal, D. Weaire, and S. Hutzler, *A simple system to illustrate the nonlinear properties of a linear chain*, To be published.

[116] B. D. Lubachevsky and R. Graham, "Dense Packings of Congruent Circles in Rectangles with a Variable Aspect Ratio", in *Discrete and Computational Geometry: The Goodman-Pollack Festschrift*, edited by B. Aronov, S. Basu, J. Pach, and M. Sharir (Springer Berlin Heidelberg, Berlin, Heidelberg, 2003), pp. 633–650.

[117] J.-C. Ono-dit-Biot, P. Soulard, S. Barkley, E. R. Weeks, T. Salez, E. Raphael, and K. Dalnoki-Veress, *Rearrangement of 2d aggregates of droplets under compression: signatures of the energy landscape from crystal to glass*, arXiv preprint arXiv:1907.08557 (2019).

[118] F. Bolton and D. Weaire, *The effects of Plateau borders in the two-dimensional soap froth. I. Decoration lemma and diffusion theorem.* Phil. Mag. B **63**, 795–809 (1991).

[119] F. Bolton and D. Weaire, *The effects of Plateau borders in the two-dimensional soap froth. II. General simulation and analysis of rigidity loss transition.* Phil. Mag. B **65**, 473–487 (1992).

[120] F. Dunne, D. Weaire, F. Bolton, and S. Hutzler, *Topological changes in wet 2d foams*, Phil. Mag. (2016).

[121] C. S. O'Hern, S. A. Langer, A. J. Liu, and S. R. Nagel, *Random packings of frictionless particles*, Phys. Rev. Lett. **88**, 075507 (2002).

[122] C. O'Hern, L. Silbert, A. Liu, and S. Nagel, *Jamming at zero temperature and zero applied stress: the epitome of disorder*, Phys. Rev. E **68**, 011306 (2003).

[123] M. van Hecke, *Jamming of soft particles: geometry, mechanics, scaling and isostaticity*, J. Phys.: Condens. Matter **22**, 033101 (2010).

[124] G. Katgert and M. van Hecke, *Jamming and geometry of two-dimensional foams*, EPL **92**, 34002 (2010).

[125] D. Bideau and J. Troadec, *Compacity and mean coordination number of dense packings of hard discs*, J. Phys. Condens. Matter **17**, L731 (1984).

[126] R. Höhler and S. Cohen-Addad, *Many-body interactions in soft jammed materials*, Soft Matter **13**, 1371–1383 (2017).

[127] D. Weaire, R. Höhler, and S. Hutzler, *Bubble-bubble interactions in a 2d foam, close to the wet limit*, Adv. Colloid Interface Sci. **247**, 491–495 (2017).

[128] J. Nocedal and S. Wright, *Numerical optimization*, 2nd ed. (Springer-Verlag New York, 2006).